8-2014

Exploring martian magmas: From the mantle to the regolith

Arya Sigrid Waltraud Udry
University of Tennessee - Knoxville, audry@utk.edu

To the Graduate Council:

I am submitting herewith a dissertation written by Arya Sigrid Waltraud Udry entitled "Exploring martian magmas: From the mantle to the regolith." I have examined the final electronic copy of this dissertation for form and content and recommend that it be accepted in partial fulfillment of the requirements for the degree of Doctor of Philosophy, with a major in Geology.

Harry Y. McSween, Major Professor

We have read this dissertation and recommend its acceptance:

Larry A. Taylor, Theodore C. Labotka, Robert N. Compton

Accepted for the Council:

Carolyn R. Hodges

Vice Provost and Dean of the Graduate School

(Original signatures are on file with official student records.)

Exploring martian magmas: From the mantle to the regolith

A Dissertation Presented for the
Doctor of Philosophy
Degree
The University of Tennessee, Knoxville

Arya Sigrid Waltraud Udry
August 2014

DEDICATION

To Sylvia

ACKNOWLEDGEMENTS

First of all, I would like to thank my advisor Dr. Hap McSween, who gave me the great opportunity to work on extremely interesting rocks. His investment and enthusiasm help improve my scientific and teaching skills. I also wish to thank my committee member Larry Taylor, Ted Labotka, and Robert Compton for their guidance in petrology and geochemistry and assistance during this PhD.

I am grateful to the rest of the faculty and staff of the Earth and Planetary Science Department for all their support and help

I would like to thank my collaborators Brian Balta, and Robert Bodnar, Pilar Leccumberi-Sanchez, and Luca Fedele for their help with the LA-ICP-MS at Virginia Tech, as well as Rick Hervig, Lynda Williams, and Mini Wadhwa for their help with the SIMS at ASU.

I would like to thank my amazing officemate Nicole and all my friends for their moral support (and, for some, their scientific input). I especially would like to thank my dear friend Peter, whose continuous support and encouragement, both real and moral, were extremely valuable during this whole PhD.

Last but not least, I am very grateful for my amazing family, my parents Sylvia and Eric, my brothers Galaad and Livio, and my grand mother Huguette who never stopped supporting me even from the other side of the planet.

ABSTRACT

The planet Mars is geologically more similar to Earth than to other planets of the solar system. For the past 50 years, new rovers, orbital spacecraft, and new martian meteorites have helped us to understand the geological processes that occurred on Mars. In this dissertation, I investigate a wide range of martian igneous compositions, such as shergottite and nakhlite meteorites, Gusev and Gale surface basalts, and the Northwest Africa (NWA) 7034 breccia. I attempt to better understand magmatic processes that occurred in the martian mantle and crust as well as surficial processes using various petrologic and geochemical tools.

As shown by thermodynamical modeling, fractional crystallization of primary martian magmas can form a wide variety of magma compositions, including: tholeiitic and alkaline, under polybaric conditions.

Parental magmas of the most common martian meteorites, shergottites, appear to have undergone water-degassing, as judged from analyses of light-lithophile elements (Li, B, Be) with varying solubilities in exsolved aqueous fluids and Li isotopes, which can be fractionated by degassing. This magmatic water might have been a major source for martian surficial water during the Amazonian period.

In addition to shergottites, I examine the petrology of four Miller Range nakhlites, which, according to various petrological evidences, come from the same parent meteorite. However, modal abundances show that their parent meteorite was heterogeneous. Therefore, discovery of new nakhlites will be critical to fully understand stratigraphic differences in the nakhlite cumulate pile.

Finally, I show that one unusual vitrophyric clast in the NWA 7034 polymict martian breccia is likely an impact melt whose parent rock has the same composition as the Humphrey Gusev basalt, and represents the first martian sample with a similar composition to surface rocks measured by rovers.

I demonstrate in this dissertation that there is a wide variety of martian igneous compositions and that the study of these compositions and recovery of new martian meteorites and analyses of martian surface basalts by rovers is critical to understanding crustal and mantle petrologic processes on Mars.

TABLE OF CONTENTS

LIST OF TABLES

LIST OF FIGURES

INTRODUCTION

Meteorites are the only samples that we possess from the planet Mars. The evidence that these meteorites are from Mars was first shown by Bogard and Johnson (1983), who argued that the gas compositions in the martian basalt EETA 79001 melt inclusions and shock veins were similar to the martian atmosphere measured by the Viking landers in 1976. Subsequently, several additional criteria for discriminating martian meteorites were outlined and are now used to verify the origin of martian meteorites, such as: 1) their specific oxygen isotopic compositions, 2) Fe-Mn ratio of pyroxene and olivines, and 3) the presence of Fe-oxides and absence of Fe-metals, which are present in other achondrite meteorites (e.g., McSween and Treiman, 1998). Because martian meteorites are the only samples that we have from Mars, their study is critical to understand the martian crust and mantle processes.

Approximately 70 unpaired martian meteorites have been described to date. They are divided in three main groups (shergottites, nakhlites, and chassignites) and two single rocks (Allan Hills – ALH – 84001 and Northwest Africa – NWA – 7034). Apart from the NWA 7034 breccia, all the martian meteorites are igneous; hence, their study allows us to understand the mineralogy, composition, and geochronology of the martian crust as well as the different mantle sources of their parental magmas. Most of these samples are volcanic rocks, however some plutonic rocks exist in the martian meteorite collection. Shergottites are the most common type of martian meteorites with approximately 55 recorded samples, which are subdivided in three groups: basaltic, olivine-phyric, and lherzolitic shergottites. Their crystallization ages (165 - 575 Ma: Stöffler et al., 1986; Taylor et al., 2002) are young compared with most of the martian surface. Basaltic and olivine-phyric shergottites represent lavas and mostly consist of pigeonite, augite, maskelynite, and olivine. Lherzolitic shergottites are plutonic rocks with cumulus olivine and oikocrysts of low-Ca pyroxene. Shergottites as a group display variable enrichment in light rare earth elements (LREE), which represent two distinct sources: 1) a reduced, depleted source and 2) an oxidized, enriched source (e.g., Herd et al., 2002). The enriched source might have originated from assimilation of crust or a metasomatized mantle with different compositions relative to the source of the depleted shergottites (e.g., McCubbin et al., 2012; Usui et al., 2012). The nakhlites are cumulate augite-rich rocks, which are older than shergottites (1.3 Ga), all of which are thought to originate from a common cumulate pile (Day et al., 2006). Chassignites are dunites that have the same crystallization age as nakhlites and are thought to originate from the same parental mantle source (McCubbin et al., 2013). ALH 84001 is the oldest martian meteorite with an age of 4.0 Ga and is a orthopyroxenite (Lapen et al., 2010). NWA 7034 and its paired meteorites are the first sedimentary samples that we possess from Mars. They are polymict regolith breccias, with U-Pb zircon ages of 4.4 Ga and 1.7 Ga (Agee et al., 2013; Humayun et al., 2013). They consist of various igneous lithologies that were never observed before in martian meteorites.

The martian meteorites are younger and have a different compositions when compared to the martian surface basalts that were analyzed by both rovers and orbital spacecraft. This indicates that the martian meteorites are biased samples of the crust

(Balta and McSween, 2013). The Spirit rover landed in the Gusev crater in January 2004, and analyzed the Gusev plain basalts, also called the Adirondack-class basalts, which consist of the representative picritic basalts: Humphrey, Adirondack, and Mazatzal (McSween et al., 2008). The Curiosity rover landed in Gale crater in August 2012, and analyzed the alkaline rock Jake_M, which is a mugearite and contains nepheline, a phase that was not observed before in martian basalt (Stolper et al., 2013). Thus, in addition to meteorites, the martian surface basalts are key to understand the martian interior.

Using data obtained from meteorites, remote sensing tools, rovers, and landers, we can now better understand the martian crust, mantle compositions, and magmatic processes. In this dissertation, we attempt to answer several petrological questions using these various martian basaltic compositions:

1) How did primary and parental martian magmas evolve, and is polybaric fractional crystallization important on Mars? On Earth, magma fractionation generally occurs during ascent, representing polybaric conditions. However, all the prior martian magma fractionation experiments and modeling were conducted at one static pressures. Thus, we conduct the first martian fractionation study under polybaric conditions. We use thermodynamical modeling to understand fractionation of various primary and parental martian basalt compositions.

2) Did magma degassing occur on Mars, and is it reflected in common igneous minerals? It was concluded that water carved the ancient martian surface. This water likely originated from magma. However, it was previously shown that martian meteorites are dry and therefore was concluded the martian mantle is dry (Dreibus and Wänke, 1985). This hypothesis was countered by new studies of hydrated phases in martian meteorites (e.g., Treiman, 1985; McCubbin et al., 2013). We investigate magmatic water by analyzing light-lithophile elements (Li, B, and Be) with different solubilities and lithium isotopes in pyroxene, olivine, and maskelynite of four compositionally different shergottites.

3) Are the Miller Range nakhlites (MIL 090030, 090032, 090136, and 03346) paired and what is the significance for their potential parent meteorite? Nakhlites are thought to originate from a common cumulate pile, and MIL 03346 was located at the top of the pile according to compositional and mineralogical evidences (Day et al., 2006). Using various petrological tools, we investigate the pairing of these Miller Range nakhlites in order to better understand their potential parent meteorite and the nakhlite cumulate pile stratigraphy.

4) How diverse are the martian basalt compositions? Only 70 samples and several martian surface basalt compositions are available. Consequently, the more samples we possess and understand, the more we can determine petrological processes on Mars. We investigate a unique vitrophyre melt clast in the NWA 7034 breccia whose composition has not been observed in martian meteorites before.

Glossary

- Alkaline magma: Magma rich in sodium and potassium relative to silica.
- Amazonian: Martian time period from 3.0 Ga to present.

- Assimilation (magmatic): Process during which magma melts the country rock, resulting in a change in the magma composition.

- Breccia: Rock composed of angular fragments (also called clasts) of pre-existing rocks or minerals cemented together by a fine-grained matrix.

- Cumulus phase: Mineral resulting from fractional crystallization.

- Fractional crystallization: Separation by gravitational settling of crystallizing minerals from magma during cooling, which results in change in magma composition.

- Hesperian: Martian time period from approximately 3.7 Ga to 3.0 Ga.

- Liquid line of descent: Series of liquid derived from single parent magma.

- Metasomatized magma: Magma that changes composition from introduction of hot aqueous solutions originating from external sources.

- Multiple saturation point: Point of unique pressure and temperature where mantle phases are present.

- Nakhlite: Type of martian meteorite. They are clinopyroxene-rich rocks originating from a unique cumulate pile on Mars.

- Noachian: Martian time period from 4.5 to 3.7 Ga.

- Oxygen fugacity (magma): Equivalent to partial pressure of oxygen in a magma expressed relative to a mineral redox buffer.

- Parental melt: Magma from which an igneous rock is crystallized and can be related through chemical properties.

- Petrology: Study of origin, chemical composition, mineralogy, distribution, alteration, and structure of igneous, metamorphic, and sedimentary rocks.

- Picritic (basalt): high magnesium basalt rich in the mineral olivine.

- Polymict (breccia): Breccia whose clasts include different lithologies or originate from different sources.

- Primary magma: Magma formed form melting of mantle and that did not undergo fractionation and/or assimilation en route to the surface.

- Primitive magma: magma that underwent minimal fractionation.

- Regolith (martian): Top layer of the martian surface that consists of unconsolidated rocks and dust, which were broken down by impacts. It is also called martian soil.

- Residual melt: Remaining magma after fractional crystallization.

- Shergottite: Most common type of martian meteorite with basaltic composition. They are composed of pyroxene, shocked plagioclase, and olivine. They are subdivided in three different groups: basaltic, olivine-phyric, and lherzolitic. The two formers are volcanic rocks whereas the latter has a plutonic origin.

- Vitrophyric: Rock consisting of phenocrysts and a glassy matrix.

- Tholeiitic magma: Magma relatively rich in iron and magnesium and poor in alkali elements relative to silica composition.

References

Agee C. B., Wilson N. V., McCubbin F. M., Ziegler K., Polyak V. J., Sharp Z. D., Asmerom Y., Nunn M. H., Shaheen R., Thiemens M. H., Steele A., Fogel M. L., Bowden R., Glamoclija M., Zhang Z., and Elardo S. M. 2013. Unique meteorite from Early Amazonian Mars: Water-rich basaltic breccia Northwest Africa 7034. *Science* 339:780-785.

Balta J. B. and McSween H. Y. 2013. Water and the composition of martian magmas. *Geology* doi:10.1130/GS34714.1Bogard and Johnson (1983)

Day J. M. D., Taylor L. A., Floss C., and McSween H. Y. 2006. Petrology and chemistry of MIL 03346 and its significance in understanding the petrogenesis of nakhlites on Mars. *Meteoritics and Planetary Science* 41:581–606.

Dreibus G., and Wänke H. 1985. Mars, a Volatile-Rich Planet. *Meteoritics* 20:367-381.

Herd C. D. K., Schwandt C. S., Jones J. H., and Papike J. J. 2002. An experimental and petrographic investigation of Elephant Moraine 79001 lithology A: Implications for its petrogenesis and the partitioning of chromium and vanadium in a martian basalt. *Meteoritics and Planetary Sciences* 37,:987–1000.

Humayun M., Nemchin A., Zanda B., Hewins R. H., Grange M., Kennedy A., Lorand J.-P., Gopel C., Fieni C., Pont S., and Deldicque D. 2013a. Origin and age of the earliest martian crust from meteorite NWA 7533. *Nature* 503:513-516.

Lapen T. J., Righter M., Brandon A. D., Debaille V., Beard B. L., Shafer J. T., and Peslier A. H. 2010. A younger age for ALH84001 and its geochemical link to shergottite sources in Mars.

McCubbin F. M., Hauri E. H., Elardo S. M., Vander Kaaden K. E., Wang J., and Shearer C. K. 2012. Hydrous melting of the martian mantle produced both depleted and enriched shergottites. *Geology* 40:683-686.

McCubbin F. M., Elardo S. M., Shearer C. K., Smirnov A., Hauri E. H., and Draper D. S. 2013. A petrogenetic model for the comagmatic origin of chassignites and nakhlites: interences from chlorine-rich minerals, petrology, and geochemistry. *Meteoritics and Planetary Science* 48:819-853.

McSween H. Y. and Treiman A. H. 1998. Martian meteorites, in *Planetary Materials*, Rev. Mineral. Geochem., vol. 36, edited by Papike J. J., pp. 6-1-6-53, Mineralogical Society of America, Washington, D.C.

McSween H. Y., Ruff S. W., Morris R. V., Gellert R., Klingelhöfer G., Christensen P. R., McCoy T. J., Ghosh A., Moersch J. M., Cohen B. A., Rogers A. D., Schröder C., Squyres S. W., Crisp J., and Yen A. 2008. Mineralogy of volcanic rocks in Gusev Crater, Mars: Reconciling Mössbauer, Alpha Particle X-Ray Spectrometer, and Miniature Thermal Emission Spectrometer spectra. *Journal of Geophysical Research* 113:E06S04.

Stöffler D., Ostertag R., Jammes C., Pfannschmidt G., Sen Gupta P. R., Simon S. B., Papike J. J., and Beauchamp R. H. 1986. Shock metamorphism and petrology of the Shergotty achondrite. *Geochimica et Cosmochimica Acta* 50:889–903.

Stolper E. M., Baker M. B., Newcombe M. E., Schmidt M. E., Treiman A. H., Cousin A., Dyar M. D., Fisk M. R., Gellert R., King P. L., Leshin L., Maurice S.,

McLennan S. M., Minitti M., Perrett G., Rowland S., Sautter V., Wiens R. C., and the MSL Science Team. 2013. The petrochemistry of Jake_M: a martian mugearite. *Science* 341:2513.

Taylor L. A., Nazarov M. A., Shearer C. K., McSween H. Y., Cahill J., Neal C. R., Ivanova M. A., Barsukova L. D., Lentz R. C., Clayton R. N. and Mayeda T. K. 2002. Martian meteorite Dhofar 019: A new shergottite. *Meteoritics and Planetary Sciences* 37:1107-1128.

Treiman A. H. 1985. Amphibole and hercynite spinel in Shergotty and Zagami: Magmatic water, depth of crystallization, and metasomatism, *Meteoritics* 20:229-243.

Usui, T., O'D Alexander C. M., Wang J., Simon J. I., and Jones J. H. 2012. Origin of water and mantle-crust interactions on Mars inferred from hydrogen isotopes and volatile element abundances of olivine-hosted melt inclusions of primitive shergottite. *Earth and Planetary Science Letters* 357–358:119–129.

CHAPTER I
EXPLORING FRACTIONATION MODELS FOR MARTIAN MAGMAS

This chapter is a reformatted version of a paper of the same name published in Journal of Geophysical research – Planets. Arya Udry, Brian Balta and Hap McSween wrote this manuscript. Arya Udry and Brian Balta conducted thermodynamical computer modeling.

Udry A., J. Brian Balta, and McSween H. Y. 2014. Exploring fractionation models for Martian magmas. Journal of Geophysical Research – Planets. 199: 1-1-8. doi:10.1002/2013JE004445

Abstract

Martian primary compositions, i.e., magmas that did not experience fractionation and/or contamination after extraction from the mantle, occur as a subset of martian meteorites and a few lavas analyzed on the planet's surface by rovers. Eruptions of primary magmas are rare on Earth and presumably on Mars. Previous studies of fractional crystallization of martian primary magmas have been conducted under isobaric conditions, simulating idealized crystallization in magma chambers. Polybaric fractionation, which occurs during magma ascent, has not been investigated in detail for martian magmas. Using the MELTS algorithm and the pMELTS revision, we present comprehensive isobaric and polybaric thermodynamic calculations of the fractional crystallization of four primary or parental martian magmas (Humphrey, Fastball, Y-980459 shergottite, and nakhlite parental melts) using various pressure-temperature paths, oxygen fugacities, and water contents to constrain how these magmas might evolve. We then examine whether known martian alkaline rock compositions could have formed through fractional crystallization of these magmas under the simulated conditions. We find that isobaric and polybaric crystallization paths produce similar residual melt compositions, but given sufficient details, we may be able to distinguish between them. We calculate that Backstay (Gusev Crater) likely formed by fractionation of a primary magma under polybaric conditions, while Jake_M (Gale Crater) may have formed through melting of a metasomatized mantle, crustal assimilation, or fractional crystallization of an unknown primary magma. The best fits for the Backstay composition indicate that consideration of polybaric crystallization paths can help improve the quality of fit when simulating liquid lines of descent.

Introduction

The martian crust is mainly composed of igneous rocks of mafic and ultramafic composition (McSween et al., 2009) and sediments derived from these rocks (e.g., Squyres et al., 2004). Chemical compositions of surface terrains measured by the Gamma-Ray Spectrometer (GRS) on Mars Odyssey (e.g., Gasnault et al., 2010), volcanic rocks analyzed by alpha particle x-ray spectrometers (APXS) on rovers, and martian meteorites analyzed in the laboratory are nearly all basalts or cumulates from basaltic magmas. Two schools of thought exist concerning the origin and evolution of these rocks: (1) they are mostly primary compositions, formed by partial melting of the mantle

and largely unaffected by fractional crystallization, or (2) they are mostly evolved compositions derived by fractionation of primary melts. Schmidt and McCoy (2010) modeled the compositions of volcanic rocks in Gusev Crater analyzed by the Spirit rover as primary magmas, although their partial melting models did not exclude later fractional crystallization. Baratoux et al. (2011, 2013) likewise interpreted varying compositions in martian basaltic units analyzed by GRS as indicating variations in the mantle temperatures and pressures of primary melt formation. Conversely, McSween et al. (2006a) and Tuff et al. (2013) modeled Gusev rocks as arising from fractionation of a primary magma composition, and Stolper et al. (2013) modeled the Jake_M alkaline rock from Gale Crater as forming from the fractionation of basaltic magma. Numerous petrologic studies have demonstrated that fractionation has been key in creating the compositions of many martian meteorites, including the cumulate nakhlites, chassignites, and ALH 84001 (e.g., McSween and Treiman, 1994; Mittlefehldt, 1994; Mikouchi et al., 2003; Treiman, 2005; Nekvasil et al., 2007a) and some of the shergottites, such as the olivine-rich lherzolitic shergottites (Goodrich, 2002). On Earth, primary magmas do not erupt on a global scale and are in fact uncommon, as most magmas undergo fractionation and/or assimilation en route to the surface (e.g., O'Hara, 1965; Stolper and Walker, 1980; BSVP, 1981). Most volcanic rocks on the Moon and on asteroid 4Vesta are also thought to represent fractionated magmas (e.g., BVSP, 1981; Shearer et al., 2006; McSween et al., 2011), despite differences in gravity, volatile contents, the compositions of mantle sources, and the crusts through which they ascended. It seems likely, then, that most martian magmas would be fractionated, a hypothesis that can be tested by comparing fractional crystallization paths with the compositions of observed martian igneous rocks.

Prior studies have investigated fractionation of martian primary magmas under static pressure conditions using experimental techniques and petrologic modeling tools (e.g., McSween et al., 2006a; Monders et al., 2007; McCubbin et al., 2008; Filiberto et al., 2008; Symes et al., 2008; Liu et al., 2013). While fractional crystallization of magmas under near-isobaric conditions occurs in magma chambers, complete or almost complete crystallization at a single pressure is not geologically common and probably unlikely for lavas that reach the surface. To date, researchers have not explicitly tested the influence of polybaric crystallization paths on martian magmas. Here we investigate martian magmatic evolution using thermodynamic modeling of three primary and one parental magma compositions (Humphrey, Fastball, Yamato-980459, and nakhlite parental melts), which span much of the known range of martian basalt compositions. We model isobaric as well as polybaric fractional crystallization to compare the resulting liquid lines of descent. We also evaluate whether fractionation of these tholeiitic primary magmas can give rise to some observed martian alkaline rock compositions (Backstay, Jake_M, and nakhlite intercumulus glass). The various fractional crystallization models presented here provide a basis for further experiments to better constrain martian magmatism.

Background and compositions used in calculations

Previous numerical models and experiments of martian magma fractionation

McSween et al. (2006a) performed a series of liquid line of descent calculations using the MELTS algorithm (Ghiorso and Sack, 1995), attempting to fit the measured compositions of Gusev alkaline rocks (Backstay, Irvine, and Wishstone) as products of isobaric crystallization of the Adirondack-class Humphrey composition at different depths. They inferred that the alkaline rocks could have formed by crystallization of a Humphrey-like magma at distinct pressures (0.1, 0.3, and 1.0 GPa respectively), high oxygen fugacities (between FMQ – fayalite-magnetite-quartz - and FMQ-1), and modest water contents (0.5 wt% H_2O). McCubbin et al. (2008) performed isobaric fractional crystallization experiments using wet (1.67 wt% H_2O) and nearly dry (0.07 wt% H_2O) Humphrey-like compositions at a static pressure of 0.93 GPa, equivalent to the base of a thick martian crust. Although they did not produce compositions similar to the measured Gusev alkaline basalts, they confirmed that the compositional evolution of a Humphrey-like parental magma depends strongly on whether the magma was wet or dry. Therefore, as is the case with magmas on Earth, fractionation of a limited set of primary magmas is able to generate substantial compositional diversity.

Fractional crystallization has also been modeled using shergottite compositions. Symes et al. (2008) performed MELTS fractional crystallization calculations using the Y-980459 composition and concluded that shergottite compositional diversity is produced by a combination of both fractional crystallization and compositionally distinct sources. Liu et al. (2013) reported pMELTS calculations on the EETA 79001A shergottite composition and suggested that its parental magma underwent polybaric fractionation, with crystallization occurring first beneath the martian crust and continuing during ascent. In addition, based on petrogenetic studies and MELTS calculations, numerous authors have concluded that nakhlites formed from closed-system fractional crystallization of a single lava flow or shallow magma body (Mikouchi et al., 2003; Treiman, 2005; Stockstill et al., 2005; Day et al., 2006; Imae and Ikeda, 2008; Sautter et al., 2012; Udry et al., 2012; McCubbin et al., 2013). Other fractional crystallization calculations using MELTS have been performed using the compositions of Shergotty (Dann et al., 2001), LAR 06319 (Peslier et al., 2010; Basu Sarbadhikari et al., 2011; Balta et al., 2013), and Dhofar 019 (Taylor et al., 2002).

Alkaline magma formation

On Earth, alkaline magmatism can be generated in oceanic hotspots, continental rift settings, flood basalt provinces, and during the late stages of island arc magmatism (e.g., BVSP, 1981). Terrestrial alkaline rocks can be produced in a variety of ways, including: high pressure melting (>1 GPa or 30 km depth: e.g., East African Rift) (Hirose and Kushiro, 1993), low degrees of partial melting (e.g., Maymecha river basin, Siberia) (Arndt et al., 1998), partial melting of metasomatic veins (e.g., French Massif Central) (Pilet et al., 2008) or metasomatic lithosphere (e.g., Nunivak Island, Alaska) (Menzies and Murthy, 1980), and fractional crystallization of wet, hotspot-derived magma at crustal pressures (e.g., Nandewar volcano, Australia) (Nekvasil et al., 2000, 2004). This

final process, fractionation of mantle-derived magma in the crust, is common on Earth and should be expected on Mars due to its thick, stagnant crust. The combination of crustal pressures and hydrous magmas produces alkaline magmas during crystallization by delaying plagioclase crystallization in favor of pyroxene and olivine. In addition, Nekvasil et al. (2000, 2004, 2007b) and Whitaker et al. (2005, 2007) showed that polybaric crystallization paths, which form pyroxene at high pressure and plagioclase at low pressure, can also contribute to alkaline magma formation. It was also shown that the role of CO_2 is critical for the formation of alkaline basalts (e.g., Hirose, 2007; Dasgupta et al., 2007).

Dreibus and Wänke (1985; 1987) were the first to propose alkali-rich basalts on Mars. Martian alkaline rocks have been analyzed *in situ* by rovers (McSween et al., 2006a; McSween et al., 2009; Stolper et al., 2013), but have not been distinguished from orbit (Dunn et al., 2007). GRS (with a footprint of 300 km) measured Si and K but not Na (e.g., Boynton et al., 2007), and likewise cannot clearly distinguish alkaline compositions. Consequently, alkaline rocks may be widespread on the martian surface and simply not be recognizable by the available measurements. None of the primary magmas studied here are alkaline, raising the question of whether the processes that form alkaline rocks on Earth are analogous on Mars.

Martian primary and parental magmas

On planetary bodies, a primary bulk composition should display high Mg# (molar Mg/(Mg+Fe) >70) and MgO content (>11 wt%), have no trace element or isotopic indicators of fractionation or assimilation, and be multiply saturated with the residual phases of the mantle (e.g., olivine, pyroxenes) at a particular combination of pressure and temperature (BVSP, 1981; Asimow and Longhi, 2004). The multiple saturation point, taken to approximate the pressure and temperature at which the primary magma formed, can be found by experiments or calculated using an appropriately calibrated model (Balta and McSween, 2013a). Investigations of martian meteorites and rocks analyzed by rovers indicate that a few martian basalts are candidates for primary magmas. For our calculations, we chose three possible martian primary magmas and one parental magma that cover the presently recognized compositional range (Table A1).

Humphrey

Humphrey is an Adirondack-class basalt from Gusev Crater analyzed by the Spirit rover (McSween et al., 2004, 2006a, 2006b). The rock is picritic (McSween et al., 2008) as revealed by the RAT-abraded rock analyzed by APXS and Mössbauer. Based on phase equilibrium experiments, Monders et al. (2007) inferred that Humphrey is a primary magma that formed by ~15-20% melting of an undepleted martian mantle source. These authors measured a multiple saturation point with olivine + orthopyroxene + spinel at 1.0 GPa and 1320 °C, corresponding to a depth of ~85 km, which they inferred to be the depth of the mantle source region. Alternatively, Filiberto et al. (2008) conducted dry experiments and suggested that Humphrey does not display a primary composition based on the fact that its composition is multiply saturated with the wrong pyroxene (pigeonite, rather than orthopyroxene as found in the Monders et al. (2007) experiments).

Fastball

Fastball was analyzed by the Spirit rover at the Home Plate outcrop in the Columbia Hills of Gusev Crater and was interpreted as pyroclastic based on its texture. Its composition is depleted in Al_2O_3, FeO, and CaO compared to Humphrey (Table A1). Fastball was an unbrushed rock and its measured composition might have greater uncertainties than others compositions discussed in this paper; however, we adopt the composition as Filiberto et al. (2010) argued that Fastball represents a primary magma based on its multiple saturation point with olivine + orthopyroxene occurring at ~1.2 GPa and ~1430 °C. Fastball and Humphrey are the only rover-analyzed compositions for which multiple saturation experiments suggest that they could represent primary compositions.

Yamato-980459

The most primitive and magnesian (Mg# = 0.67) of the shergottites is the olivine-phyric shergottite Yamato-980459 (henceforth Y-98). It consists of olivine megacrysts set in a groundmass of Fe-rich olivine and pyroxene, basaltic glass, and skeletal Fe-Ti-Cr oxides (Greshake et al., 2004; Ikeda et al., 2004; McKay et al., 2004; Musselwhite et al., 2006; Usui et al., 2008). Musselwhite et al. (2006) argued that Y-98 represents a primary composition with an experimentally produced multiple saturation point (olivine + low-Ca pyroxene) at 1.2 ± 0.5 GPa and 1540 ± 10 °C. Although a few other shergottites have been proposed as primary magmas (NWA 5789 and NWA 6234 (Gross et al., 2011; Filiberto and Dasgupta, 2011; Gross et al., 2013)), experiments have only been conducted on Y-98. Usui et al. (2012) measured low water contents in olivine-hosted melt inclusions in Y-98 and suggested they required a dry parental magma. However, Balta et al. (2013) argued that those inclusions could be susceptible to water loss after trapping while the crystals resided in the magmatic system, so in our calculations we also consider the possibility that Y-98 (or a similar magma) was more hydrous than argued by Usui et al. (2012). In addition, Draper (2007) and Balta and McSween (2013a) hypothesized its composition could be consistent with the presence of some magmatic water.

Nakhlite parental melts

The nakhlites are olivine-bearing clinopyroxenites thought to have crystallized in a cumulate pile from a single magma (Harvey and McSween, 1992a; Mikouchi et al., 2003). They are mainly composed of augite, olivine, and glassy intercumulus phase (e.g., Treiman, 2005; Day et al., 2006; Udry et al., 2012). Although the nakhlite parental melt is not necessarily a primary magma (e.g., Sautter et al., 2012; McCubbin et al., 2013), it was included in this study in order to expand the range of available martian compositions. Augite-liquid partition coefficients and augite- and olivine-hosted melt inclusions have been used to constrain the nakhlite parental melt composition (e.g., Harvey and McSween, 1992a; Treiman and Goodrich, 2001; Varela et al., 2001; Stockstill et al., 2005; Sautter et al., 2012). Stockstill et al. (2005) argued that the nakhlite parental melt had a low water content, although recent measurements have identified some hydrous apatites and amphiboles that may contradict this conclusion (McCubbin et al., 2009;

Hallis et al., 2012). For the nakhlite parental melt compositions, we used the estimates of Stockstill et al. (2005) and Sautter et al. (2012), which analyzed melt inclusions in Nakhla augites after fast-heating rehomogenization. These compositions are broadly similar to other proposed nakhlite parental melts (e.g., Harvey and McSween, 1992a; Treiman, 1993; Treiman and Goodrich, 2001), but differ slightly from each other: the composition of Sautter (NPM05) is moderately depleted in CaO, MgO, P_2O_5, and alkalis and enriched in FeO relative to that of Stockstill (NA03) (Table A1). The NK01 parental melt composition calculated by Treiman and Goodrich (2001) was not used in this study because Stockstill et al. (2005) showed that their NA03 models better matched the major element compositions measured in nakhlites, despite the fact that NK01 and NA03 major element compositions are very similar.

Alkaline martian magmas

Our fractional crystallization modeling produced a wide variety of plausible martian igneous compositions. We selected several martian alkaline rock compositions measured by rovers and in meteorites (Table A1) and attempted to use our database to better understand magma formation conditions.

Backstay

Backstay was one of the first alkaline basaltic rocks encountered by Spirit in the Columbia Hills in Gusev Crater (McSween et al., 2006a). Backstay is a trachybasalt (also called hawaiite) (McSween et al., 2006a) and is the least altered rock found on the Columbia Hills (Ming et al., 2006). It is silica-saturated and hypersthene-normative, as are various terrestrial continental and oceanic island alkaline basalts (e.g., Nandewar volcano, Ascension Island) (Nekvasil et al., 2000, 2004; Harris, 1993). McSween et al. (2006a) argued that, in these alkaline rocks, the plagioclase is richer in sodium, the olivine is richer in iron, and the pyroxene:olivine ratio is higher than in Adirondack-class rocks (e.g., Humphrey).

Jake_M

Near the beginning of its traverse in Gale Crater, the Curiosity rover analyzed a volcanic rock named Jake_M (Grotzinger et al., 2013). Based on the norm calculated from APXS analyses, it contains >15% nepheline, as well as albite and orthoclase, and has a composition similar to a terrestrial mugearite (also called trachy-andesite) (Stolper et al., 2013). Using isobaric MELTS calculations and a terrestrial starting composition, Stolper et al. (2013) argued that Jake_M formed by suppression of plagioclase during fractionation of a parental magma, which they estimated could occur at ~0.4 GPa in the presence of water (~1 wt%).

Nakhlite intercumulus glass

Based on rare earth element abundance patterns, nakhlites are interpreted to have fractionally crystallized in a closed system (e.g., Wadhwa and Crozaz, 1995; Day et al., 2006; Udry et al., 2012) in which augite crystallized prior to olivine. The intercumulus glass in Miller Range nakhlites displays alkaline compositions, plotting in or around the

trachy-andesite and trachyte fields in the TAS diagram (Day et al., 2006; Udry et al., 2012).

Modeling techniques

In total, we conducted more than six hundred polybaric and isobaric fractional crystallization calculations using different P-T paths, variable oxygen fugacities (between FMQ-3.5 and FMQ), and water contents that ranged from dry to ~1.67 wt% H_2O using the AlphaMELTS front end of the MELTS algorithm (Smith and Asimow, 2005). The calculations are summarized in Table A2. AlphaMELTS runs the routines of MELTS, pMELTS, and pHMELTS (Ghiorso and Sack, 1995; Ghiorso et al., 2001; Asimow et al., 2004). MELTS is a thermodynamic-based algorithm calibrated using petrologic experiments on both terrestrial and planetary compositions (Balta and McSween, 2013b), and is commonly used in calculating mineral assemblages along crystallization paths. pMELTS is an updated calibration to the initial version which allows for application of the algorithm at elevated pressures up to 3 GPa. Balta and McSween (2013b) argued that calculations using the MELTS algorithm can be expected to reproduce martian compositions close to the liquidus to within uncertainties better than 1 wt% for most major oxides if the conditions of crystallization are fully explored. In this study, we used both MELTS and pMELTS, depending on the conditions. pMELTS has been found to be more accurate in determining pyroxene and olivine stabilities (Balta and McSween, 2013b); consequently, the pMELTS calibration was principally used for determining the pressure and temperature of multiple saturation points involving these minerals. However, the pMELTS calibration poorly simulates the composition of phases that crystallize outside its calibrated range and thus calculations using the MELTS calibration were required at low pressures. It was shown that the effect of water modeled by pMELTS yields similar results to experiments, whereas MELTS does not reproduce the effect of water on olivine liquidus temperatures (Medard and Grove, 2008). Spinel stability is also overestimated in both calibrations (Balta and McSween, 2013b), so we avoid drawing conclusions based on its crystallization. Apart from water, other volatiles such as F, Cl, and SO_3 have been hypothesized as contributors to martian magmas, particularly Cl in nakhlites (Filiberto and Treiman, 2009; McCubbin et al., 2013), and CO_2 in alkaline magmas (e.g., Hirose, 1997; Dasgupta et al., 2007), but the software is not well-constrained for these components and thus we are unable to consider them explicitly. Instead, we focus on whether crystallization involving the available components can reproduce the trends discussed.

We calculated the results of magmatic crystallization along a large series of P-T paths (Fig. A1). These P-T paths can be generally described by 4 endmembers: 1) high-pressure fractionation followed by sub-adiabatic ascent (requiring minor heat loss) and decompression (Path α), 2) medium-pressure fractionation followed by sub-adiabatic ascent (Path β), 3) sub-adiabatic ascent followed by low-pressure fractionation (Path γ), and 4) isobaric fractionation (Path σ), calculated for comparison with polybaric paths. Path σ in Figure A1 shows simple fractionation at static pressure within a magma chamber. The three polybaric P-T paths α, β, and γ do not involve true adiabatic ascent

because that would cause re-melting of previously formed phases, effectively resetting the calculation until it again becomes sub-adiabatic (Liu et al., 2013). We began calculations ~10 °C above the liquidus temperatures, which depend on the starting compositions and water contents. For isobaric calculations, fractional crystallization was modeled in 5 °C steps, whereas for polybaric calculations, the temperature steps varied from ~1 °C to 10 °C and pressure steps varied from 5 to 200 bars. The calculations were halted when they became unstable, stopping the calculated crystallization sequence, or at ~900 °C, as lower temperatures are outside of the MELTS-calibrated range.

We also investigated the effect of water on fractional crystallization. Previously, it has been demonstrated that some martian magmas were wet based on several lines of evidence, including 1) hydrated minerals in trapped melt inclusions (0.2 wt% H_2O in the original magma) (Treiman, 1985), 2) soluble light-lithophile element zoning patterns in pyroxenes (1.8 wt% H_2O in parent magma) (Lentz et al., 2001; McSween et al., 2001), 3) pyroxene crystallization systematics (1.8 wt% H_2O in the parent magma) (Dann et al., 2001), 4) H and O isotopic compositions (75-116 ppm H_2O in the parent magma) (Usui et al., 2012), and 5) water analyses in apatite (at least 0.07-0.29 wt% H_2O in the parent magma) (McCubbin et al., 2012) and in amphiboles (0.15-0.25 wt% H_2O in the parental magma) (Watson et al, 1994; McCubbin et al., 2010). We selected 0.5 wt% H_2O as a reasonable approximation for wet primary magmas (e.g., Watson et al, 1994; McSween et al., 2001; Usui et al., 2012; McCubbin et al., 2012) and also calculated crystallization of the Humphrey composition with 1.67 wt% H_2O in order to compare with the experiments of McCubbin et al. (2008).

To examine the influence of oxygen fugacity on the fractionation of martian primary magmas, we varied oxygen fugacities for each composition within the ranges estimated for those samples (Table A2). The oxygen fugacity of Humphrey was estimated between FMQ-3.1 and FMQ-1.7 (Schmidt et al, 2011), whereas no clear oxygen fugacity has been determined for Fastball. Martian meteorites show oxygen fugacities between FMQ-3.5 (equal to the iron-wüstite buffer) and FMQ-0.5 (Righter et al., 2008). The depleted martian mantle is thought to be reduced (~FMQ-3.5) (Herd et al., 2002), and the source of oxidation in some meteorites is debated. The oxidized character may be due to metasomatism, ferric iron-rich material, or the presence of water, and its source may be located within the crust or within a heterogeneous mantle (Herd et al, 2002; Herd, 2003; Wadhwa, 2008). Thus, we used FMQ-2.5 and FMQ-1 in Humphrey and Fastball calculations, which reasonably encompass the range of martian meteorite oxygen fugacities and those calculated by Schmidt et al. (2011), as well as FMQ-2, in order to compare our results to the McCubbin et al. (2008) experiments. Oxygen fugacities applied to Y-98 and nakhlite parental melt calculations are the same as those assessed for their magma sources: FMQ-3.5 and FMQ-2.5 for Y-98 (Shearer et al., 2006), and FMQ and FMQ-1 for nakhlites (Wadhwa et al., 2004; Righter et al., 2008; McCubbin et al., 2013).

To explore how known martian alkaline compositions (Backstay, Jake_M, and nakhlite intercumulus glass) may have formed on Mars, we used major-element compositions to constrain the plausible conditions of formation (e.g., isobaric and polybaric P-T paths, water contents, and oxygen fugacities) from the investigated starting

compositions. To obtain major element composition best fits, we applied a least-squares fit calculated from deviations between the calculated and measured compositions. We crosschecked the least-squares method manually with the individual important oxide values to estimate the accuracy of the fits.

Isobaric and polybaric fractional crystallization of martian magmas

Humphrey

Isobaric fractional crystallization calculations (starting at 1.25 GPa and 1400 °C) for a dry magma showed that, unsurprisingly, the liquid lines of descent vary due to changes in mineral stability associated with the pressures and the volatile contents. Under dry conditions, at relatively low pressures (<0.6 GPa), the liquid evolves towards the sub-alkaline field in the total alkalis versus silica (TAS) diagram (Fig. A2) due to plagioclase fractionation with a decrease in FeO* due to olivine crystallization, whereas at higher pressure (>0.7 GPa), the liquid decreases in SiO_2 (extending to the tephrite field), increases in FeO*, and moves towards the alkaline field due to increasing pyroxene stability at higher pressures. Under wet conditions, the residual liquid shows increasing SiO_2 and decreasing FeO* at every pressure and forms alkaline magma at pressures >0.8 GPa under isobaric conditions. The evolution of these liquid lines of descent is similar to those of terrestrial silica-saturated alkaline rocks (Nekvasil et al., 2004).

Polybaric P-T paths for Humphrey began at 1.25 GPa and 1350-1390 °C (Fig. A3b). Our calculations show that the liquid evolution paths are not significantly impacted by oxygen fugacity. However, the addition of water stabilizes olivine relative to pyroxene and plagioclase, such that residual melts increase in SiO_2 and decrease in FeO* under wet conditions (0.5% H_2O). Humphrey-like magma that ponds at shallow depth (path γ) remains sub-alkaline, whereas alkaline magma forms during fractionation at depth (>0.8 GPa: path α). Alkaline magma formation is favored when crystallization takes place at elevated pressures with water present as those conditions reduce the crystallization of plagioclase, causing retention of alkali elements (such as Na) in the magma. Under anhydrous conditions, liquids decrease in SiO_2 but can still form alkaline compositions if the parental magma is fractionated at high or medium pressure (>0.8 GPa, corresponding to paths α and β). Silica enrichment and sub-alkaline compositions are found for magma that undergoes lower pressure, sub-adiabatic ascent (path γ).

We also calculated conditions to match the experiments of McCubbin et al. (2008) (0.07 and 1.67 wt% H_2O and fO_2 = FMQ-2), to compare isobaric and polybaric fractionation and the effects of water. Polybaric calculations and isobaric experiments (McCubbin et al., 2008) reveal that residual melts from fractionation of a wet Humphrey magma (1.67 wt% H_2O: Figs. A3 and A4) increase in SiO_2 and decrease in FeO* (α, β, and γ), whereas relatively dry residual magma (0.07 wt% H_2O, Fig. A5 and A6) broadly decreases in SiO_2 and increases in FeO*. One exception occurs when dry magma undergoes sub-adiabatic ascent (path γ), which first increases in SiO_2 and decreases in FeO* but then increases in FeO* during late-stage crystallization. Both dry and wet magmas show decreases in Al_2O_3 due to plagioclase crystallization after 40% solidification (Figs. A3c and A5c) and decreases in CaO after augite and plagioclase

crystallization begins (20% fractionation, Figs. A3e and A5e; orders of mineral appearance for Humphrey and other compositions are shown in the auxiliary material).

Fastball

pMELTS crystallization models started at 1.25 GPa and 1350-1390 °C. As with Humphrey, the oxygen fugacities did not significantly influence the liquid paths. Isobaric calculations performed using a Fastball composition result in liquid lines of descent similar to Humphrey. Figure A7 shows liquid lines of descent for FMQ-1 with 0.5 wt% H_2O for isobaric fractionation: as with Humphrey, at high pressure (>0.9 GPa: path α), the melt evolves towards an alkaline composition with decreasing SiO_2 and increasing FeO*, whereas low-pressure isobaric crystallization results in sub-alkaline magmas, increasing SiO_2, and decreasing FeO*.

Polybaric calculations for 0.5 wt% H_2O reveal that, if the magma is held at depth followed by sub-adiabatic ascent (≥0.8 GPa: paths α and β), the residual melt has an alkaline composition regardless of oxygen fugacity. Conversely, the residual melt compositions from magma that underwent lower-pressure, sub-adiabatic ascent remain sub-alkaline (Fig. A8, path γ). If the primary magma is dry, the liquid paths are similar to those of Humphrey and decrease in SiO_2 and increase in FeO* when the magma is held at high or medium pressures (≥0.8 GPa: paths α and β), and increase in SiO_2 and decrease in FeO* when it is held at low pressures (path γ). Decreasing Al_2O_3 is again observed when plagioclase crystallizes (after 40% fractionation) and decreasing CaO when augite and plagioclase crystallize. Calculations of Fastball crystallization show that the residual melts are similar to those produced from Humphrey magma under similar conditions, which is predictable, as their bulk compositions are very similar and they may be derived from the same mantle source, consistent with the occurrence of both rocks in Gusev Crater.

Y-98 Shergottite

Calculations for the Y-98 composition start at 1.25 GPa and 1480 °C. As with the previous calculations, varying oxygen fugacities did not significantly change the liquid evolution paths. Isobaric crystallization calculations performed under both dry and wet (0.5 wt% H_2O) conditions show that the liquid lines of descent remain mostly within the sub-alkaline field and show increases in FeO*. Only under very high-pressure conditions (1.3 and 1.4 GPa) do liquids reach into the alkaline field (not shown). The liquid shows decreasing SiO_2 at high pressures (>0.7 GPa) due to increasing pyroxene stability with higher pressure, and increasing SiO_2 at lower pressures (<0.7 GPa).

For the polybaric paths (α, β, and γ) in dry or wet systems at FMQ-3.5 and FMQ-2.5, the liquid lines of descent also remain sub-alkaline (Fig. A9). The fact that mostly sub-alkaline magma is produced is due to the fact that Y-98 bulk composition is depleted in alkali elements relative to the other compositions studied. However, overall decreases in SiO_2 are observed for P-T paths α and β, whereas those representing path γ increase in SiO_2. Again, both Al_2O_3 and CaO decrease when plagioclase and augite begin to crystallize.

Nakhlite Parental Melt

Both Stockstill et al. (2005) and Sautter and al. (2012) used MELTS (at FMQ and FMQ-1) to assess crystallization of the nakhlite parental magmas believed to have occurred at a shallow level (low pressure) (Day et al., 2006). As the MELTS routine is calibrated for low-pressure processes and to compare results from both routines, we used MELTS in addition to pMELTS for nakhlite parental melt calculations. Starting conditions were 1.25 GPa and 1330-1380 °C. We performed calculations for both nakhlite parental melt compositions, Stockstill (NA03) and Sautter (NPM05), under dry conditions. The liquid lines of descent evolve differently for the two parental melts. Residual melts from NPM05 remain within the sub-alkaline field at all pressures (not shown), whereas residual melt from NA03 extends into the trachy-andesite field on the TAS diagram (Fig. A10). This difference is likely due to the fact that NA03 is enriched in alkalis compared to NPM05. However, both compositions show initial increases in SiO_2 and FeO*, followed by decreases in FeO*, due to olivine fractionation, at high and low pressures.

For both NA03 and NPM05 compositions, pMELTS polybaric calculations at FMQ and FMQ-1 for the dry and wet (0.5 wt% H_2O) systems remain in the sub-alkaline field for all P-T paths (α, β, and γ), although wet melts more closely approach the alkalic field than dry melts. MELTS calibration calculations for NPM05 under dry and wet conditions also remain sub-alkaline (Fig. A10). Finally, MELTS calculations using NA03 (for a dry magma with FMQ-1) evolve into the alkaline field and towards trachyte compositions for all P-T paths, similar to isobaric calculations. FeO* variation in the magma is due to crystallization of augite and olivine. Feldspar crystallization is responsible for decreasing Al_2O_3 (which begins after 30% fractionation). The only pyroxene to crystallize is augite, so the residual liquid shows continuously decreasing CaO.

Alkaline magma generation

Backstay

Based on our calculations, we conclude that despite some differences, Backstay could have formed from a primary magma similar to Humphrey or Fastball if the fractionation of the primary magma occurred under appropriate conditions.

Figure A11 shows liquid lines of descent for paths β, γ, and σ, all of which lead to major elemental compositions close to Backstay. The P-T path which gives the best fit for Backstay from an Adirondack basalt parent involves medium-pressure fractionation followed by sub-adiabatic ascent (path β). Based on our least-squared comparison, using a polybaric path improves the quality of the fit compare to an isobaric path. Calculations show that water (~0.5 wt% H_2O) must have been present in the initial magma to produce this composition, and it requires 10-30% fractionation of olivine and pyroxene. Although fO_2 only slightly impacts the final composition, the fit is slightly better at FMQ-1.

Jake_M

We performed best-fit calculations on Jake_M; however, we considered a wider range of conditions than Stolper et al. (2013) (isobaric and polybaric conditions, fO_2

values, water contents, and martian starting primary compositions) for our calculations and used pMELTS. It has been shown that MELTS underestimates the pressure of multiple saturation for martian liquids while pMELTS more accurately reproduces them (Balta and McSween, 2013b). Using their correction, isobaric MELTS calculations between 1 bar and 0.6 GPa conducted by Stolper et al. (2013) would correspond roughly from 1 bar to 2.4 GPa (Balta and McSween, 2013b). Our pMELTS calculations show that the Jake_M composition can be obtained from crystallization of a Humphrey starting composition with 0.5 wt% H_2O and an oxygen fugacity of FMQ-1 if the fractionation occurs at high pressures (1.0-1.25 GPa) followed by sub-adiabatic ascent (Fig. A12b, path α). The calculated residual liquid composition has a very low MgO content compared to the actual Jake_M composition (0.3 versus 3.6 wt%: Fig. A12). This low MgO content is a consequence of the best-fit composition occurring after 90% fractionation of olivine, garnet, feldspar, and pyroxene, whereas Stolper et al. (2013) argued that the rock formed by 57% fractionation of olivine and pyroxene. The percentage of fractionation calculated in our polybaric model seems too high to be realistic. Thus, we cannot conclude that Jake_M formed from a primary Humphrey-like magma, but instead requires an unknown primary magma produced by melting of an alkali rich, possibly metasomatized mantle source or by crustal assimilation.

Nakhlite intercumulus glass

We obtained residual liquids similar in composition to the Miller Range intercumulus glass using MELTS fractional crystallization calculations from the NA03 parental melt composition (Stockstill et al., 2005). According to our models, the best-fit crystallization path occurs when the initial NA03 magma follows polybaric path β while dry and close to FMQ-1 (Fig. A13), consistent with previous nakhlite studies (Wadhwa et al., 2004; Righter et al., 2008). The requirement that the magma is dry is consistent with the melt inclusion measurements of Stockstill et al. (2005) (but contrary to hydrous apatite measurements of Hallis et al. (2012)). Fractionation of approximately 70% augite and 10% olivine is required to fit the groundmass composition, similar to the abundances observed in the Miller Range nakhlites (Udry et al., 2012) (Fig. A13). However, despite these calculations nakhlite formation by polybaric fractionation appears impossible according to the petrological observations of Day et al. (2006), who argued that nakhlites formed in two steps: 1) isobaric crystallization of olivine and pyroxene in a magma chamber, and 2) eruption at the martian surface with subsequent crystallization of the intercumulus phase. Notably, no continuous fractionation occurred during magma ascent and we present several possible explanations to explain this behavior. First, the MELTS and pMELTS calibrations may simply not be precise enough to produce an accurate pressure estimate in these high-augite content magmas (Balta and McSween, 2013b). Alternatively, as we show below, continuous crystallization on a polybaric path can approximate isobaric crystallization or crystallization at several pressures; thus, our polybaric path could be describing the case where the melt formed most of its crystals at some pressure in a magma chamber and then upwelled to the surface where final crystallization took place, similar to the sequence hypothesized by Day et al. (2006). Finally, McCubbin et al. (2013) hypothesized assimilation of a Cl-rich brine during

crystallization of the nakhlites. The algorithms do not include Cl as a component and, although there has been initial characterization of its impact on phase equilibria (e.g., Filiberto and Treiman, 2009), estimating its effect on compositions would require experiments detailing its impact on the full liquid line of descent (including compositions far from the liquidus). The assimilation of Cl could possibly produce a liquid line of descent for the Miller range groundmass that mimics those simulated in our Cl-free polybaric crystallization paths.

Discussion

Primary and parental martian magma evolution

Both Fastball and Humphrey compositions show similar magmatic evolution paths under both isobaric and polybaric conditions. High- and medium-pressure fractionation followed by sub-adiabatic ascent (paths α and β) causes evolution of both magmas to alkaline compositions, although the exact P-T paths which produce alkaline compositions depend on water content. The residual magmas that underwent low-pressure crystallization following sub-adiabatic ascent (path γ) remain sub-alkaline. Thus, Humphrey and Fastball melts can produce alkaline magmas under appropriate conditions. We note again that other mechanisms for generating alkaline compositions, such as direct melting of metasomatized mantle or low-degree melting, cannot be ruled out on Mars; however, they are not required by the Backstay composition.

The evolution of nakhlite parental melts is distinct from that of the Humphrey and Fastball compositions. The NPM05 composition only yields sub-alkaline compositions even if the primary magma is held at high pressures; however, the dry NA03 magma produces alkaline compositions under both isobaric and polybaric conditions. These results show that water is not always necessary to form alkaline magmas by fractional crystallization of primary and parental magmas on Mars, analogous to Earth (e.g., Whitaker et al., 2007).

The evolution of the Y-98 shergottite magma differs from that of other martian primary magmas in that only very high pressure conditions yield alkaline magma. Shergottites may not be abundant at the martian surface (Balta and McSween, 2013a), even if we assume that shergottites are derived from primary magmas with similar composition to Y-98.

The main conclusion we can draw from these thermodynamic models is that isobaric and polybaric fractional crystallization of the known primary and parental martian magmas can lead to a large range of residual liquid compositions. Our calculations suggest that martian igneous rocks could easily be more diverse than suggested by the limited martian meteorites and mission datasets. Specifically, we hypothesize that alkaline rocks may be more common at that surface than has been recognized to date. This claim may be supported by the observation of clasts with alkaline composition in the martian meteorite breccia NWA 7034 (Santos et al., 2013), which is thought to be a sample of the martian regolith.

In addition, liquid lines of descent for each primary magma do not show significant differences between most isobaric and polybaric paths. The liquid lines of descent for

each primary magma, determined using major-element trends under high-pressure isobaric conditions, are similar to the polybaric fractionation paths α and β. Likewise, trends under low-pressure, isobaric conditions are similar to path γ under polybaric conditions. These results imply that isobaric experiments conducted at different static pressures can likely reproduce realistic magmatic processes regardless of modest changes in pressure as the magmas migrate through the crust. In general, oxygen fugacity does not significantly alter martian liquid evolution paths if the changes remain within the measured martian magma range. However, water contents significantly influence the compositions of residual magmas, as shown in experiments (e.g., McCubbin et al., 2008; Nekvasil et al., 2009).

Implications for Mars magmatic evolution over time

Our calculations imply that alkaline magma formation on Mars is analogous to Earth in that sub-alkaline magmas like Humphrey and Fastball are predicted to stagnate at elevated pressures. Furthermore, high-pressure fractionation might be more common for younger rocks as martian crustal thickness has increased over time (Baratoux et al., 2011). Consequently, formation of alkaline magmas on Mars should be more common in recent martian history. McCubbin et al. (2008) hypothesized that crustal thickening with time could lead to magmas underplating the crust and forming cumulates; generation of residual alkaline magmas would be a byproduct of that process. Alkaline magmas in Gusev Crater have been dated as early Hesperian (Greeley et al., 2005), suggesting that significant crustal thickening might have occurred by this time.

The presence of water in martian magma has been long-debated (e.g., Watson et al, 1994; McSween et al., 2001; Usui et al., 2012; McCubbin et al., 2012). This study provides indirect support for some wet martian magmas due to the fact that Backstay requires water in order to be formed from a tholeiitic primary magma.

Summary

More than six hundred pMELTS and MELTS fractional crystallization calculations were conducted under isobaric and polybaric conditions using three martian primary and one parental magma compositions. The results provide a better understanding of the evolution of primary martian magmas and the formation of alkaline rocks.

- Fractional crystallization of the different investigated magmas explain much of the observed diversity of martian rock compositions. Residual liquids resulting from fractional crystallization of Humphrey and Fastball evolve similarly under the same conditions. The Y-98 shergottite and the nakhlite magma composition of Sautter et al. (2012) do not form alkaline magmas, whereas the Stockstill et al. (2005) dry nakhlite parental melt evolves towards a trachy-andesite composition similar to nakhlite intercumulus glass compositions.
- MELTS and pMELTS calculations demonstrate that the liquid lines of descent determined from major element trends under high-pressure isobaric conditions are similar to the polybaric paths α and β, which remain at elevated pressures for the early portions of their crystallization paths. In addition, our calculations show that liquid lines of

descent representing low-pressure isobaric conditions are similar to polybaric fractionation path γ. These results demonstrate that isobaric and polybaric calculations yield residual liquids with similar compositions, suggesting that isobaric experiments on martian primary magmas can produce realistic results, even in cases where polybaric crystallization may have occurred.

- Backstay may have formed from fractionation of a wet primary magma having a Humphrey- or Fastball-like composition, under either isobaric or polybaric conditions with 10-30% fractionation. Backstay calculations suggest that martian magmatic water was present during the early Hesperian. The best fits for Backstay suggest that considering a polybaric crystallization path may improve the quality of the fit when simulating liquid lines of descent.
- Jake_M was not formed by fractionation of any of the primary magma compositions evaluated here, but more likely formed from a magma affected by melting of a metasomatized mantle source, crustal assimilation, or by fractional crystallization of a yet unrecognized primary melt.
- Despite the fact that our models allow the nakhlite intercumulus glass to have formed by polybaric fractional crystallization of a nakhlite parental melt under dry conditions with 80% fractionation, our model seems to differ from petrological observations, arguing that nakhlites formed mostly under isobaric conditions, requiring an alternative explanation for the fit.
- Because alkaline magmas are easily formed if crystallization occurs at high pressure, progressive thickening of the martian crust may imply that alkaline magmas have become more widespread during recent martian time.

As shown in this study, MELTS and pMELTS are very useful in calculating isobaric and polybaric fractionation models with different variables. Experimental results to confirm these results are desirable, and further crystallization experiments under varying conditions can be guided by the results of these calculations.

References

Arndt N., Chauvel C., Czamanske G., and Fedorenko V. 1998. Two mantle sources, two plumbing systems: Tholeiitic and alkaline magmatism of the Maymecha River basin, Siberian flood volcanic province, *Contributions to Mineralogy and Petrology* 133:297-313.

Asimow P. D. and Longhi J. 2004. The significance of multiple saturation points in the context of polybaric near-fractional melting. *Journal of Petrology* 45:2349-2367.

Asimow, P. D., Dixon J. E., and Langmuir C. H. 2004. A hydrous melting and fractionation model for mid-ocean ridge basalts: Application to the Mid-Atlantic Ridge near the Azores, *Geochemistry, Geophysics, Geosystems* 5:Q01E16.

Balta J. B. and McSween H. Y. 2013a. Water and the composition of martian magmas. *Geology* doi:10.1130/GS34714.1.

Balta J. B. and McSween H. Y. 2013b. Application of the MELTS algorithm to Martian compositions and implications for magma crystallization. *Journal of Geophysical Research – Planets* 118:2502-2519.

Balta J. B., Sanborn M., McSween H. Y., and Wadhwa M. 2013. Magmatic history and parental melt composition of olivine-phyric shergottite LAR 06319: Importance of magmatic degassing and olivine antecrysts in martian magmatism. *Meteoritics and Planetary Sci*ences 48:1359-1382.

Baratoux D., Toplis M. J., Monnereau M., and Gasnault O. 2011. Thermal history of Mars inferred from orbital geochemistry of volcanic provinces. *Nature* 472:338–341.

Baratoux D., Toplis M. J., Monnereau M., and Sautter V. 2013. The petrological expression of early Mars volcanism. *Journal of Geophysical Research* 118:59-64.

Basu Sarbadhikari A., Goodrich C. A., Liu Y., Day J. M. D., and Taylor L. A. 2011. Evidence for heterogeneous enriched shergottite mantle sources in Mars from olivine-hosted melt inclusions in Larkman Nunatak 06319. *Geochimica et Cosmochimica Acta* 75:6803–6820.

Basaltic Volcanism Study Project. 1981. *Basaltic Volcanism on the Terrestrial Planets*, Pergamon Press, Inc., New York. 1286 pp.

Boynton W. V., Taylor G. J., Evans L. G., Reedy R. C., Starr R., Janes D. M., Kerry K. E., Drake D. M., Kim K. J., Williams R. M. S., Crombie M. K., Dohm J. M., Baker V., Metzger A. E., Karunatillake S., Keller J. M., Newsom H. E., Arnold J. R., Bruckner J., Englert P. A. J., Gasnault O., Sprague A. L., Mitrofanov I., Squyres S. W., Trombka J. I., d'Uston L., Wanke H., and Hamar D. K. 2007. Concentration of H, Si, Cl, K, Fe, and Th in the low- and mid-latitude regions of Mars. *Journal of Geophysical Research* 112:E12S99.

Dann J. C., Holzheid A. H., Grove T. L., and McSween H. Y. 2001. Phase equilibria of the Shergotty meteorite: Constraints on preeruptive H_2O contents of martian magmas and fractional crystallization under hydrous conditions. *Meteoritics and Planetary Sciences* 36:793–806.

Dasgupta R., Hirschmann M., and Smith N. 2007. Partial melting experiments of peridotite + CO2 at 3 GPa and genesis of alkalic ocean island basalts. *Journal of*

Petrology 48:2093-2124.

Day J. M. D., Taylor L. A., Floss C., and McSween H. Y. 2006. Petrology and chemistry of MIL 03346 and its significance in understanding the petrogenesis of nakhlites on Mars. *Meteoritics and Planetary Sciences* 41:581– 606.

Draper D. S. 2007. Water-undersaturated near-liquidus phase relations of Yamato 980459: Preliminary results. (abstract #1447) 38th Lunar Planetary Sience Conference. CD-ROM.

Dreibus G., and Wänke H. 1985. Mars, a Volatile-Rich Planet. *Meteoritics* 20:367-381.

Dreibus G., and Wänke H. 1987. Volatiles on Earth and Mars - a Comparison. *Icarus* 71:225-240.

Dunn T. L, McSween H. Y., and Christensen P. R. 2007. Thermal emission spectra of terrestrial alkaline volcanic rocks: Applications to Martian remote sensing. *Journal of Geophysical Research* 112:E05001.

Filiberto J. and Treiman A. H. 2009. Martian magmas contained abundant chlorine, but little water. *Geology* 37:1087-1090.

Filiberto J. and Dasgupta R. 2011. Fe^{2+}-Mg partitioning between olivine and basaltic melts: Applications to genesis of olivine- phyric shergottites and conditions of melting in the Martian interior. *Earth and Planetary Science Letters* 304:527–537.

Filiberto J., Treiman A. H., and Le L. 2008. Crystallization experiments on a Gusev Adirondack basalt composition. *Meteoritics and Planetary Science* 43:1137–1146.

Filiberto, J., Dasgupta R., Kiefer W. S., and Treiman A. H. 2010. High pressure, near‐liquidus phase equilibria of the Home Plate basalt Fastball and melting in the Martian mantle. *Geophysical Research Letters* 37:L13201.

Foley S. F. 1988 The genesis of continental basic alkaline magmas- an interpretation in terms of redox melting. *Journal of Petrology* Special Lithosphere Issue 139-161.

Gasnault O., Taylor G. J., Karunatillake S., Dohm J., Newsom H., Forni O., Pinet P., and Boynton W. V. 2010. Quantitative geochemical mapping of martian elemental provinces. *Icarus* 207:226-247.

Ghiorso M. S. and Sack R. O. 1995. Chemical mass-transfer in magmatic processes IV. A revised and internally consistent thermodynamic model for the interpolation and extrapolation of liquid-solid equilibria in magmatic systems at elevated-temperatures and pressures. *Contribution to Mineralogy and Petrology* 119:197-212.

Ghiorso M. S., Hirschmann M. M., Reiners P. W., and Kress V. C. 2001. The pMELTS: A revision of MELTS for improved calculation of phase relations and major element partitioning related to partial melting of the mantle to 3 GPa. *Geochemistry, Geophysical, Geosystems* 3:1030.

Goodrich C. A. 2002. Olivine-phyric martian basalts: A new type of shergottite, *Meteoritics and Planetary Sciences* 37:B31-B34.

Greeley R., Foing B. H., McSween H. Y., Neukum G., Pinet P., Van Kan S. C., Werner M., Williams D. A., and Zegers T. E. 2005. Fluid lava flows in Gusev Crater, Mars. *Journal of Geophysical Research* 110:E05008.

Greshake A., Fritz J., and Stoffler D. 2004. Petrology and shock metamorphism of the olivine-phyric shergottite Yamato 980459: Evidence for a two-stage cooling and a single-stage ejection history. *Geochimica et Cosmochimica Acta* 68:2359–2377.

Gross J., Treiman A. H., Filiberto J., and Herd C. D. K. 2011. Primitive olivine-phyric shergottite NWA 5789: Petrography, mineral chemistry, and cooling history imply a magma similar to Yamato-980459. *Meteoritics and Planetary Sciences* 46:116–133.

Gross J., Filiberto J., Herd C. D. K., Melwani M., Schwenzer S. P., and Treiman A. H. 2013. Petrography, mineral chemistry, and crystallization history of olivine-phyric shergottite NWA 6234: A new melt composition. *Meteoritics and Planetary Sciences* 48:854-871.

Grotzinger J. P., Blake D. F., Crisp J., Edgett K. S., Gellert R., Gomez-Elvira J., Hassler D., Mahaffy P., Malin M. C., Mitrofanov I., Meyer M., Vasavada A., Wiens R. C., and the MSL Science Team. 2013. Mars Science Laboratory: First 100 sols of geologic and geochemical exploration from Bradbury landing to Glenelg (abstract #1259) 44th Lunar Planetary Science Conference. CD-ROM.

Hallis L. J., Taylor G. J., Nagashima K., and Huss G. R. 2012. Magmatic water in the martian meteorite Nakhla. *Earth Planetary and Science Letters* 359-360:84-92.

Harris C. 1983. The petrology of lavas and associated plutonic inclusions in Ascension Islands. *Journal of Petrol*ogy 24:424-470.

Harvey R. P. and McSween H. Y. 1992a The parent magma of the nakhlite meteorites: Clues from melt inclusions. *Earth and Planetary Science Letters* 111:467-482.

Herd C. D. K. 2003. The oxygen fugacity of olivine-phyric martian basalts and the components within the mantle and crust of Mars. *Meteoritics and Planetary Sciences* 38:1793-1805.

Herd C. D. K., Schwandt C. S., Jones J. H., and Papike J. J. 2002. An experimental and petrographic investigation of Elephant Moraine 79001 lithology A: Implications for its petrogenesis and the partitioning of chromium and vanadium in a martian basalt. *Meteoritics and Planetary Sciences* 37,:987–1000.

Hirose K. 1997. Partial melt compositions of carbonated peridotite at 3 GPa and role of CO2 in alkali-basalt magma generation. *Geophysical Research Letters* 24:2837-2840.

Ikeda Y. 2004. Petrology of the Yamato 980459 shergottite. *Antarctica Meteorite Research* 17:35–54.

Hirose K. and Kushiro I. 1993. Partial melting of dry peridotites at high pressures: Determination of compositions of melts segregated from peridotite using aggregates of diamond. *Earth and Planetary Science Letters* 114:477-489.

Imae N. and Ikeda Y. 2008. Crystallization experiments of intercumulus melts for nakhlites under FMQ ± 2 at 1 bar. *Meteoritics and Planetary Sciences* 43:1299–1319.

Irvine T. N. and Baragar W. R. A. 1971 A guide to the chemical classification of the common volcanic rocks, *Canadian Journal of Earth Sciences* 8:523–548.

Le Bas M. J., Le Maitre R. W., Streckeisen A., and Zanettin B. 1986. A chemical classification of volcanic rocks based on the total alkali-silica diagram. *Journal of Petrology* 27:745–750.

Lentz R. C. F., McSween H. Y., Ryan J., and Riciputti L. R. 2001. Water in martian magmas: Clues from light lithophile elements in shergottite and nakhlite pyroxenes. *Geochimica et Cosmochimica Acta* 65:4551–4565.

Liu Y., Balta J. B., Goodrich C. A., McSween H. Y., and Taylor L. A. 2013. New constraints on the formation of shergottite Elephant Moraine 79001 lithology A, *Geochimica et Cosmochimica Acta* 108:1-20.

McCubbin F. M., Nekvasil H., Harrington A. D., Elardo S. M., and Lindsley D. H. 2008. Compositional diversity and stratification of the Martian crust: Inferences from crystallization experiments on the picrobasalt Humphrey from Gusev Crater, Mars. *Journal of Geophysical Research* 113:E11013.

McCubbin F. M., Tosca N. J., Smirnov A., Nekvasil H., Steele A., Fries M., and Lindsley D. H. 2009. Hydrothermal jarosite and hematite in a pyroxene-hosted melt inclusion in martian meteorite Miller Range (MIL) 03346: Implications for magmatic-hydrothermal fluids on Mars. *Geochimica et Cosmochimica Acta* 73:4907-4917.

McCubbin F. M., Smirnov A., Nekvasil H., Wang J., Hauri E., and Lindsley D. H. 2010. Hydrous magmatism on Mars: A source of water for the surface and subsurface during the Amazonian. *Earth and Planetary Science Letters* 292:132–138.

McCubbin F. M., Hauri E. H., Elardo S. M., Vander Kaaden K. E., Wang J., and Shearer C. K. 2012. Hydrous melting of the martian mantle produced both depleted and enriched shergottites. *Geology* 40:683-686.

McCubbin F. M., Elardo S. M., Shearer C. K., Smirnov A., Hauri E. H., and Draper D. S. 2013. A petrogenetic model for the comagmatic origin of chassignites and nakhlites: interference from chlorine-rich minerals, petrology, and geochemistry, *Meteoritics and Planetary Sciences* 48:819-853.

McSween H. Y. and Treiman A. H. 1998. Martian meteorites, in *Planetary Materials*, Rev. Mineral. Geochem., vol. 36, edited by Papike J. J., pp. 6-1-6-53, Mineralogical Society of America, Washington, D.C.

McSween H. Y., Grove T. L., Lentz R. C. F., Dann J. C., Holzheid A. H., Riciputi L. R., and Ryan J. G. 2001. Geochemical evidence for magmatic water within Mars from pyroxenes in the Shergotty meteorite. *Science* 409:487-489.

McSween H. Y., Arvidson R. E., Bell III J. F., Blaney D., Cabrol N. A., Christensen P. R., Clark B. C., Crisp J. A., Crumpler L. S., Des Marais D. J., Farmer J. D., Gellert R., Ghosh A., Gorevan S., Graff T., Grant J., Haskin L. A., Herkenhoff K. E., Johnson J. R., Jolliff B. L., Klingelhoefer G., Knudson A. T., McLennan S., A. Milam K., Moersch J. E., Morris R. V., Rieder R., Ruff S. W., de Souza Jr. P. A., Squyres S. W., Wänke H., A. Wang, M. B. Wyatt, A Yen., J. Zipfel. 2004. Basaltic rocks analyzed by the Spirit rover in Gusev Crater. *Science* 305:842–845.

McSween H. Y. Jr., Ruff S. W., Morris R. V., Bell III J. F., Herkenhoff K., Gellert R., Stockstill K. R., Tornabene L. L., Squyres S. W., Crisp J. A., Christensen P. R., McCoy T. J., Mittlefehldt D. W., and Schmidt M. 2006a. Alkaline volcanic rocks from the Columbia Hills, Gusev Crater, Mars. *Journal of Geophysical Res*earch 111:E09S91.

McSween H. Y. Jr., Wyatt M. B., Gellert R., Bell III J. F., Morris R. V., Herkenhoff K. E., Crumpler L. S., Milam K. A., Stockstill K. R., Tornabene L. L., Arvidson R. E., Bartlett P., Blaney D., Cabrol N. A., Christensen P. R., Clark B. C., Crisp

J. A., Des Marais D. J., Economou T., Farmer J. D., Farrand W., Ghosh A., Golombek M., Gorevan S., Greeley R., Hamilton V. E., Johnson J. R., Joliff B. L., Klingelhöfer G., Knudson A. T., McLennan S., Ming D., Moersch J. E., Rieder R., Ruff S. W., Schröder C., de Souza Jr. P. A., Squyres S. W., Wänke H., Wang A., Yen A., and Zipfel J. 2006b. Characterization and petrologic interpretation of olivine-rich basalts at Gusev Crater, Mars. *Journal of Geophysical Research* 111:E02S10.

McSween H. Y., Ruff S. W., Morris R. V., Gellert R., Klingelhöfer G., Christensen P. R., McCoy T. J., Ghosh A., Moersch J. M., Cohen B. A., Rogers A. D., Schröder C., Squyres S. W., Crisp J., and Yen A. 2008. Mineralogy of volcanic rocks in Gusev Crater, Mars: Reconciling Mössbauer, Alpha Particle X-Ray Spectrometer, and Miniature Thermal Emission Spectrometer spectra. *Journal of Geophysical Research* 113:E06S04.

McSween H. Y., Taylor G. J., and Wyatt M. B. 2009. Elemental composition of the martian crust. *Science* 324:736-739.

McSween H. Y., Mittlefehldt D. W., Beck A. W., Mayne R. G., and McCoy T. J. 2011. HED meteorites and their relationship to the geology of Vesta and the Dawn mission. *Space Science Reviews* 163:141-174.

Medard E. and Grove T. 2008. The effect of H2O on the olivine liquidus of basaltic melts: experiments and thermodynamic models. *Contribution to Mineralogy and Petrology* 155:417-432.

Mezies M. and Murthy V. R. 1980. Mantle metasomatism as a precursor to the genesis of alkaline magmas – isotopic evidence. *American Journal of Science* 280:622-638.

Mikouchi T., Koizumi E., Monkawa A., Ueda Y., and Miyamoto M. 2003. Mineralogy and petrology of Yamato-000593: Comparison with other Martian nakhlite meteorites. *Antarctica Meteorite Research* 16:34–57.

Ming D. W., Mittlefehldt D. W., Morris R. V., Golden D. C., Gellert R., Yen A., Clark B. C., Squyres S. W., Farrand W. H., Ruff S. W., Arvidson R. E., Klingelhöfer G., McSween H. Y., Rodionov D. S., Schröder C., De Souza P. A., and Wang A. 2006. Geochemical and mineralogical indicators for aqueous processes in the Columbia Hills of Gusev Crater, Mars. *Journal of Geophysical Research* 111: E02S12.

Mittlefehldt D. W. 1994. ALH 84001, a cumulate orthopyroxenite member of the martian meteorite clan. *Meteoritics and Planetary Sciences* 29:214-221.

Monders A. G., Médard E., and Grove T. L. 2007. Phase equilibrium investigations of the Adirondack class basalts from the Gusev plains, Gusev Crater, Mars. *Meteoritics and Planetary Sciences* 42:131-148.

Musselwhite D. S., Dalton H. A., Kiefer W. S., and Treiman A. H. 2006. Experimental petrology of the basaltic shergottite Yamato-980459: Implications for the thermal structure of the Martian mantle. *Meteoritics and Planetary Sciences* 41: 1271-1290.

Nekvasil H., Simon A., and Lindsley D. H. 2000. Crystal fractionation and the evolution of intra-plate hy-normative igneous suites: Insights from their feldspars. *Journal of Petrology* 41:1743–1757.

Nekvasil, H., Dondolini A., Horn J., Filiberto J., Long H., and Lindsley D. H. 2004. The origin and evolution of silica-saturated alkalic suites: An experimental study. *Journal*

of Petrology 45:693–721.

Nekvasil H., Filiberto J., McCubbin F. M., and Lindsley D. H. 2007a. Alkalic parental magmas for Chassignites? *Meteoritics and Planetary Sciences* 6:979-992.

Nekvasil H., McCubbin F. M., Harrington A., O'Leary M. C., Elardo S., and Lindsley D. H. 2007b. Crustal differentiation on Mars: Insights from rocks analyzed by the MER rover (abstract #3181) 7th International Conference on Mars. CD-ROM.

Nekvasil H., McCubbin F. M., Harrington A., Elardo S., and Lindsley D. H. 2009. Linking the Chassigny meteorite and the Martian surface rock Backstay: Insights into igneous crustal differentiation processes on Mars. *Meteoritics and Planetary Sciences* 44:853-869.

O'Hara M. J. 1965. Primary magmas and the origin of magmas. *Scottish Journal of Geology* 1:19-40.

Peslier A. H., Hnatyshin D., Herd C. D. K., Walton E. L., Brandon A. D., Lapen T. J., and Shafer J. T. 2010. Crystallization, melt inclusion, and redox history of a Martian meteorite: Olivine-phyric shergottite Larkman Nunatak 06319. *Geochimica et Cosmochimica Acta* 74:4543–4576.

Pilet S., Baker M. B., and Stolper E. M. 2008. Metasomatized lithosphere and the origin of alkaline lavas. *Science* 320:916-919.

Rapp J. F., Draper D. S., and Mercer C. M. 2013. Anhydrous liquid line of descent of Yamato 980459 and evolution of martian parental magmas (abstract #1688) 44th Lunar Planetary Science Conference. CD-ROM.

Righter K., Yang H., Costin G., and Downs R. T. 2008. Oxygen fugacity in the Martian mantle controlled by carbon: New constraints from the nakhlite MIL 03346. *Meteoritics and Planetary Sciences* 43:1709–1723.

Santos A. R., Agee C. B., McCubbin F. M., Shearer C. K., and Burger P. V. 2013. Martian breccia NWA 7034: Basalt, mugearite, and trachy-andesite clasts (abstract #5284) 76th Meteoritical Society Meeting.

Sautter V., Toplis M. J., Lorand J.-P., and Macri M. 2012. Melt inclusions in augite from the nakhlite meteorites: A reassessment of nakhlite parental melt and implications for petrogenesis. *Meteoritics and Planetary Sciences* 47:330-344.

Schmidt M. E. and McCoy T. J. 2010. The evolution of a heterogeneous Martian mantle: Clues from K, P, Ti, Cr, and Ni variations in Gusev basalts and shergottite meteorites. *Earth and Planetary Science Letters* 296:67-77.

Schmidt M. E., Schrader C. M., and McCoy T. J. 2011. How oxidized are the Gusev basalts? (abstract #2277) Lunar and Planetary Science Conference. CD-ROM.

Shearer C. K., McKay G., Papike J. J., and Karner J. M. 2006. Valence state partitioning of vanadium between olivine-liquid: Estimates of the oxygen fugacity of Y980459 and application to other olivine-phyric martian basalts. *American Mineralogist* 91:1657-1663.

Shearer C. K., Hess P. C., Wieczorek M. A., Pritchard M. E., Parmentier E. M., Borg L. E., Longhi J., Elkins-Tanton L. T., Neal C. R., Antonenko I., Canup R. M., Halliday A. N., Grove T. L., Hager B. H., Lee D.-C., and Wiechert U. 2006. Thermal and Magmatic Evolution of the Moon, in New views of the Moon, Reviews in Mineralogy and Geochemistry, vol. 60, Rev. Mineral. Geochem., edited by B. L. Joliff, M. A.

Wieczoreck, C. K. Shearer, and C. R. Neal, pp. 365-518, Mineralogical Society of America, Chantilly, VA.

Smith P. M. and Asimow P. D. 2005. Adiabat_1ph: A new front end to the MELTS, pMELTS, and pHMELTS models. *Geochemistry, Geophysics, Geosystems* 6:Q02004.

Squyres S. W., Grotzinger J. P., Arvidson R. E., Bell III J. F., Calvin W., Christensen P. R., Clark B. C., Crisp J. A., Farrand W. H., Herkenhoff K. E., Johnson J. R., Klingelhofer G., Knoll A. H., McLennan S. M., McSween H. Y., R. V. Morris, J. W. Rice Jr., R. Rieder, and L. A. Soderblom (2004), *In situ* evidence for an ancient aqueous environment at Meridiani Planum, Mars, *Science, 306*, 1709-1714.

Squyres, S. W., O. Aharonson, B. C. Clark, B. A. Cohen, L. Crumpler, P. A. de Souza, W. H. Farrand, R. Gellert, J. Grant, J. P. Grotzinger, A. F. C. Haldemann, J. R. Johnson, G. Klingelhöfer, K. W. Lewis, R. Li, T. McCoy, A. S. McEwen, H. Y. McSween Jr., Ming D. W., Moore J. M., Morris R. V., Parker T. J., Rice J. W., Ruff S., Schmidt M., Schröder C., Soderblom L. A., and Yen A. 2007. Pyroclastic activity at Home Plate in Gusev Crater, Mars. *Science* 316:738- 742.

Stockstill K. R., McSween H. Y., and Bodnar R. J. 2005. Melt inclusions in augite of the Nakhla Martian meteorite: Evidence for basaltic parental melt. *Meteoritics and Planetary Sciences* 40:377–396.

Stolper E. M. and Walker D. 1980. Melt density and the average composition of basalts. *Contribution to Mineralogy and Petrology* 74:7-12.

Stolper E. M., Baker M. B., Newcombe M. E., Schmidt M. E., Treiman A. H., Cousin A., Dyar M. D., Fisk M. R., Gellert R., King P. L., Leshin L., Maurice S., McLennan S. M., Minitti M., Perrett G., Rowland S., Sautter V., Wiens R. C., and the MSL Science Team. 2013. The petrochemistry of Jake_M: a martian mugearite. *Science* 341:2513.

Symes S. J. K., Borg L. E., Shearer C. K., and Irving A. J. 2008. The age of the martian meteorite Northwest Africa 1195 and the differentiation history of the shergottites. *Geochimica et Cosmochimica Acta* 72:1696–1710.

Taylor L. A., Nazarov M. A., Shearer C. K., McSween H. Y., Cahill J., Neal C. R., Ivanova M. A., Barsukova L. D., Lentz R. C., Clayton R. N. and Mayeda T. K. 2002. Martian meteorite Dhofar 019: A new shergottite. *Meteoritics and Planetary Sciences* 37:1107-1128.

Treiman A. H. 1985. Amphibole and hercynite spinel in Shergotty and Zagami: Magmatic water, depth of crystallization, and metasomatism, *Meteoritics* 20:229-243.

Treiman A. H. 1993. The parent magma of the Nakhla (SNC) meteorite, inferred from magmatic inclusions, *Geochimica et Cosmochimica Acta* 57:4753–4767.

Treiman A. H. 2005. The nakhlite meteorites: Augite-rich igneous rocks from Mars. *Chemie Erde* 65:203–270.

Treiman A. H. and Goodrich C. A. 2001 A parent magma for the Nakhla martian meteorite: Reconciliation of estimates from 1-bar experiments, magmatic inclusions in olivine, and magmatic inclusions in augite (abstract #1107) Lunar and Planetary Science Conference. CD-ROM.

Tuff J., Wade J., and Wood B. J. 2013. Volcanism on Mars controlled by early

oxidation of the upper mantle. *Nature* 498:342-345.

Udry A., McSween H. Y., Lecumberri-Sanchez P., and Bodnar R. J. 2012. Paired nakhlites MIL 090030, 090032, 090136, and 03346: Insights into the Miller Range parent meteorite. *Meteoritics and Planetary Sciences* 47:1575-1589.

Usui T., McSween H. Y., and Floss C. 2008. Petrogenesis of olivine-phyric shergottite Yamato 980459, revisited. *Geochimica et Cosmochimica Acta* 72:1711–1730.

Usui, T., O'D Alexander C. M., Wang J., Simon J. I., and Jones J. H. 2012. Origin of water and mantle-crust interactions on Mars inferred from hydrogen isotopes and volatile element abundances of olivine-hosted melt inclusions of primitive shergottite. *Earth and Planetary Science Letters* 357–358:119–129.

Varela M. E., Kurat G., and Clocchiatti R. 2001. Glass-bearing inclusions in Nakhla (SNC meteorite) augite: Heterogeneously trapped phases. *Mineralogy and Petrology* 71:155–172.

Wadhwa M. 2008. Redox Conditions on Small Bodies, the Moon and Mars. *Reviews in Mineralogy and Geochemistry* 68:493-510.

Wadhwa M. and Crozaz G. 1995. Trace and minor elements in minerals of nakhlites and Chassigny: Clues to their petrogenesis. *Geochimica et Cosmochimica Acta* 59:3629–3645.

Wadhwa M., Crozaz G., and Barrat J.-A. 2004. Trace element distributions in the Yamato 000593/000749, NWA 817 and NWA 998 nakhlites: Implications for their petrogenesis and mantle source on Mars. *Antarctica Meteorite Research* 17:97–116.

Watson L. L., Hutcheon I. D., Epstein S., and Stolper E. M. 1994. Water on Mars: Clues from Deuterium/Hydrogen and Water Contents of Hydrous Phases in SNC Meteorites. *Science* 265:86-90.

Whitaker M. L., Nekvasil H., and Lindsey D. H. 2005. Potential magmatic diversity on Mars (abstract #1440) Lunar and Planetary Science Conference. CD-ROM.

Whitaker M. L., Nekvasil H., Lindsey D. H., and Difrancesco N. J. 2007. The role of pressure in producing compositional diversity in intraplate basaltic magma. *Journal of Petrology* 48:365-393.

Wieczorek M. A. and Zuber M. T. 2004. Thickness of the Martian crust: Improved constraints from geoid-to-topography ratios. *Journal of Geophysical Research* 109:E01009.

Appendix A

Table A1. Bulk rock composition of martian basalts used in this study

	Humphrey[a]	Fastball[b]	Y98[c]	NPM Stockstill[d]	NPM Sautter[e]	Jake_M[f]	MR Nakhlite[g]
SiO_2	45.9	45.3	49.66	47.2	49.1	51.8	60.2
TiO_2	0.55	0.67	0.48	0.88	1.10	0.91	0.53
Al_2O_3	10.7	7.85	6.03	5.90	6.20	16.0	17.7
Fe_2O_3	3.55	9.26	0	0	0	0	0
Cr_2O_3	0.6	0.49	0.71	0	0.04	0	0
FeO	15.6	8.54	15.88	26.9	22.6	11.66	6.82
MnO	0.41	0.47	0.43	0.71	0.55	0.17	0.09
MgO	10.4	12	18.2	4.60	5.30	3.61	0.15
CaO	7.84	5.8	7.24	10.1	12.1	6.76	4.63
Na_2O	2.54	2.35	0.80	2.30	1.80	6.39	6.11
K2O	0.1	0.23	0.02	0.39	0.32	2.23	1.68
P_2O_5	0.56	0.79	0.31	0.09	0.36	0.56	1.09
Total	98.8	93.8	99.8	99.1	99.5	100.0	98.9

[a]McSween et al. [2008]; [b]Squyres et al. [2007]; [c]Musselwhite et al. [2006]; [d]Stockstill et al. [2005]; [e]Sautter et al. [2012]; [f]Stolper et al. [2013]; [g]average from Day et al. [2006] and Udry et al. [2012].

Table A2. MELTS and pMELTS thermodynamic calculations performed in this study

Water contents			Oxygen fugacities	Humphrey(pMELTS)	Fastball (pMELTS)	Y-98 (pMELTS)	Nakhlite parental melt (MELTS and pMELTS)
P-T path α: High pressure fractionation followed by sub-adiabatic ascent							
Dry (H_2O)	(0.0/0.07	wt%	FMQ-3.5 - FMQ-2.5			X	
			FMQ-2.5 - FMQ-2 - FMQ-1	X	X		
			FMQ-1 - FMQ				X
Wet (H_2O)	(0.5/1.67	wt%	FMQ-3.5 - FMQ-2.5			X	
			FMQ-2.5 - FMQ-2 - FMQ-1	X	X		
			FMQ-1 - FMQ				X
P-T path β: Medium pressure fractionation followed by sub-adiabatic ascent							
Dry (H_2O)	(0.0/0.07	wt%	FMQ-3.5 - FMQ-2.5			X	
			FMQ-2.5 - FMQ-2 - FMQ-1	X	X		
			FMQ-1 - FMQ				X
Wet (H_2O)	(0.5/1.67	wt%	FMQ-3.5 - FMQ-2.5			X	
			FMQ-2.5 - FMQ-2 - FMQ-1	X	X		
			FMQ-1 - FMQ				X
P-T path γ: Sub-adiabatic ascent followed by low pressure fractionation							
Dry (H_2O)	(0.0/0.07	wt%	FMQ-3.5 - FMQ-2.5			X	
			FMQ-2.5 - FMQ-2 - FMQ-1	X	X		
			FMQ-1 - FMQ				X
Wet (H_2O)	(0.5/1.67	wt%	FMQ-3.5 - FMQ-2.5			X	
			FMQ-2.5 - FMQ-2 - FMQ-1	X	X		
			FMQ-1 - FMQ				X
P-T path σ: Isobaric fractionation							
Dry (H_2O)	(0.0/0.07	wt%	FMQ-3.5 - FMQ-2.5			X	
			FMQ-2.5 - FMQ-2 - FMQ-1	X	X		
			FMQ-1 - FMQ				X
Wet (H_2O)	(0.5/1.67	wt%	FMQ-3.5 - FMQ-2.5				
			FMQ-2.5 - FMQ-2 - FMQ-1	X	X		
			FMQ-1 - FMQ				

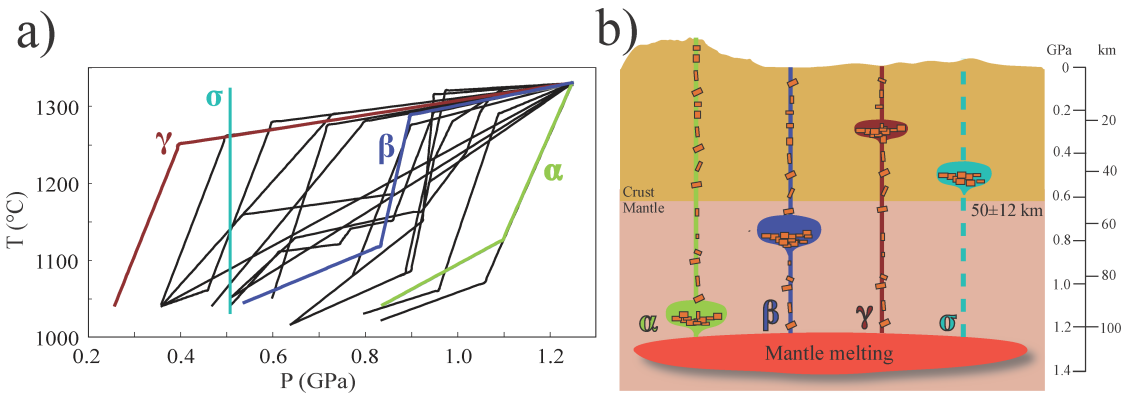

Figure A1. a) Various P-T paths used in this study with highlighted endmembers P-T paths. b) Schematic representing fractional crystallization of a primary tholeiitic magma in the martian interior following different endmembers P-T paths: Path α (green): fractionation at high pressure followed by sub-adiabatic ascent. Path β (blue): fractionation at medium pressure followed by sub-adiabatic ascent. Path γ (red): sub-adiabatic ascent of primary magma followed by stagnation at shallow level. Path σ (turquoise): Isobaric fractionation at static pressure (~0.5 GPa).

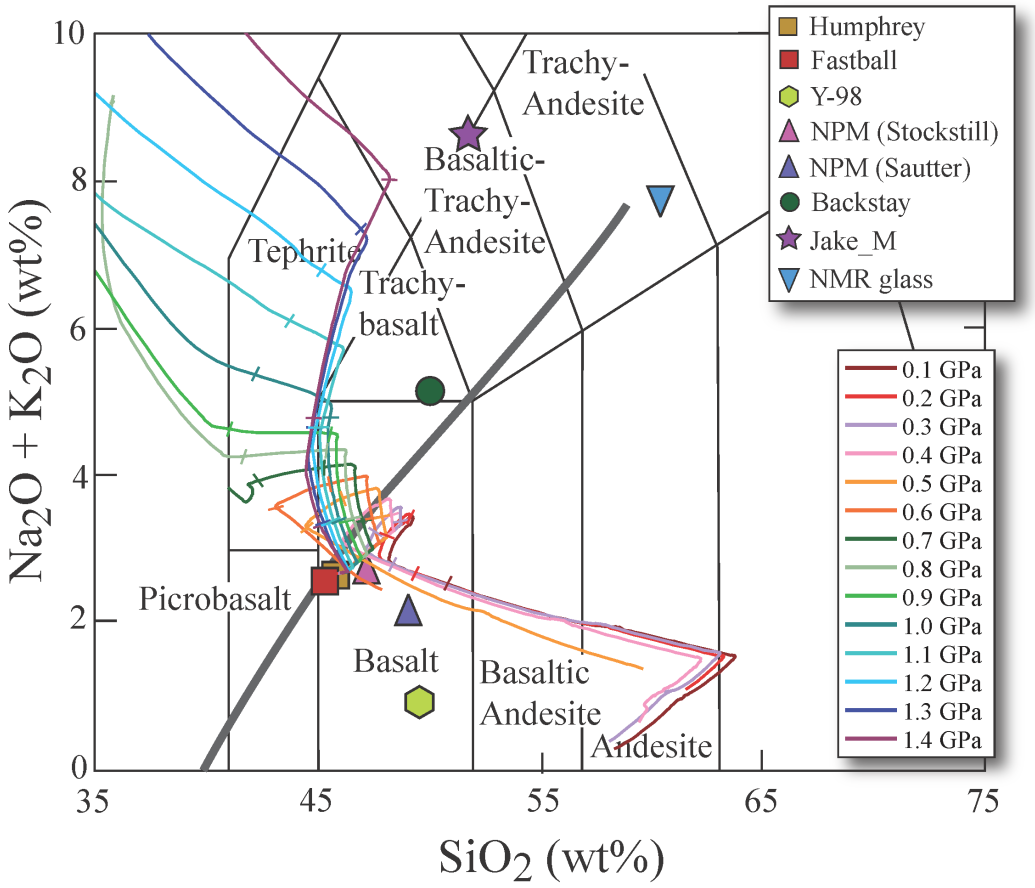

Figure A2. Total alkali-silica diagram for classifying volcanic rocks [Le Bas et al., 1986], showing the compositions of Humphrey, Fastball, Y-98, nakhlite parental melts (NPM), Backstay, Jake_M, and nakhlite Miller Range intercumulus glass average (NMR) compositions (references as in Table 1). Gray line is the boundary between alkaline and sub-alkaline compositions [Irvine and Baragar, 1971]. Different colored lines represent calculated liquid lines of descent for fractional crystallization of a Humphrey-like magma, under dry, isobaric conditions from 0.1 to 1.4 GPa at FMQ-1. Tick marks delineate 25% fractionation increments.

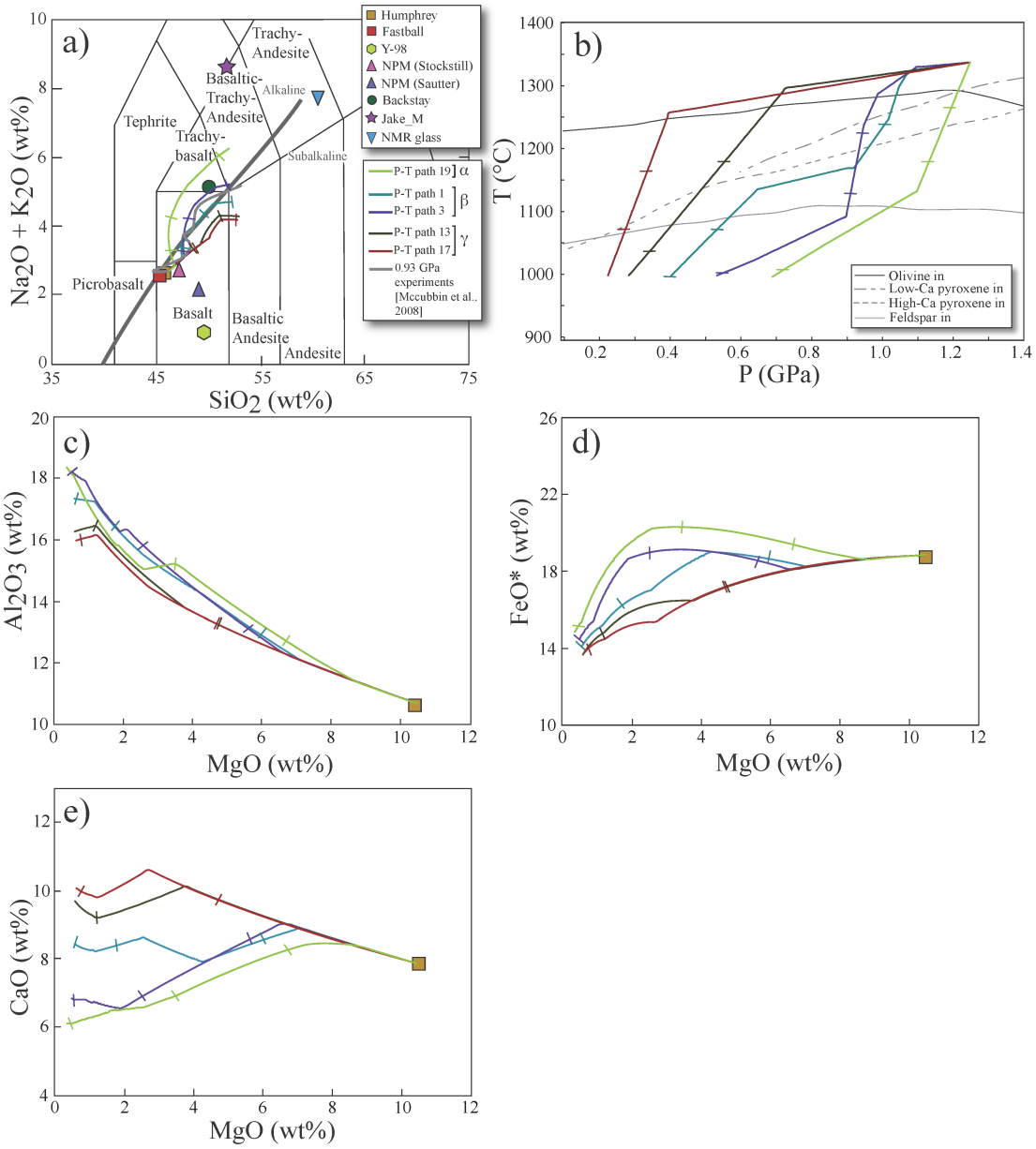

Figure A3. a) Total alkali-silica diagram showing liquid lines of descent calculated with pMELTS for fractional crystallization of the Humphrey composition with 1.67 wt% H_2O at FMQ-2 and P-T paths displayed in b). The liquid line of descent under wet conditions from McCubbin et al. (2008) is indicated in grey. b) P-T paths used to calculate liquid lines of descent in 3a and c-e). Olivine, low-Ca pyroxene, high-Ca pyroxene, and feldspar liquidi are shown as black and gray solid and dashed lines, respectively. Plots of c) Al_2O_3, d) FeO*, and e) CaO versus MgO for liquid lines of descent. Tick marks delineate 20% fractionation increments.

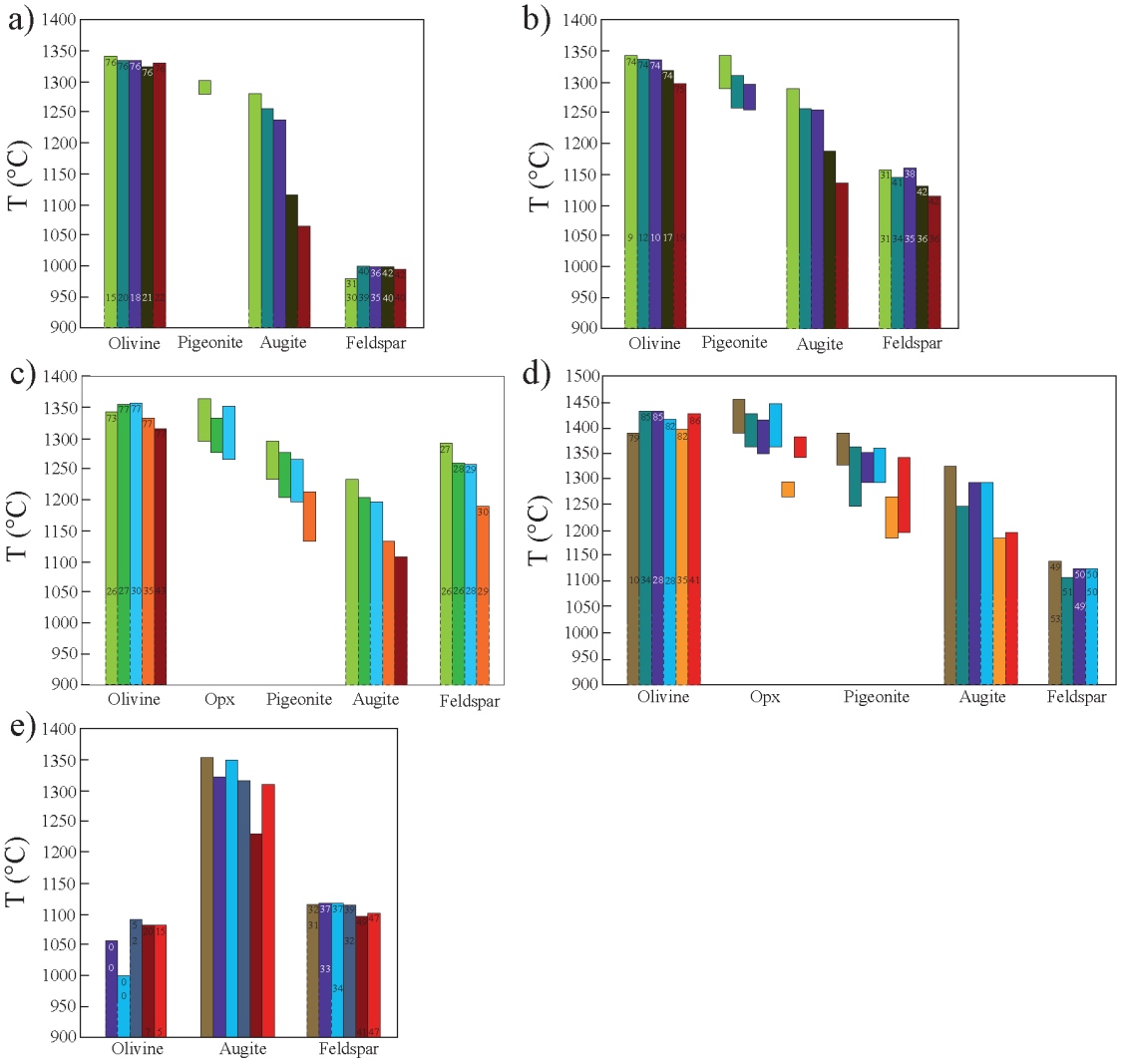

Figure A4. Order of appearance of minerals in the pMELTS liquid lines of descent for a) Humphrey melt composition (1.67 wt% H2O and FMQ-1), b) Humphrey melt composition (0.07 wt% H2O and FMQ-1), c) Fastball (0.5 wt% H2O and FMQ-1) d) Y-980459 (0.0 wt% H2O and FMQ-2.5), and e) Nakhlite parental melt from Sautter et al. [2012] (0.0 wt% H2O and FMQ-2.5 in MELTS). P-T paths represented in Figures a), b), c), d), e) correspond to the paths in Figures 3, 5, 8, 9, and 10 respectively. Numbers in olivine and plagioclase represent the forsterite and anorthite contents respectively.

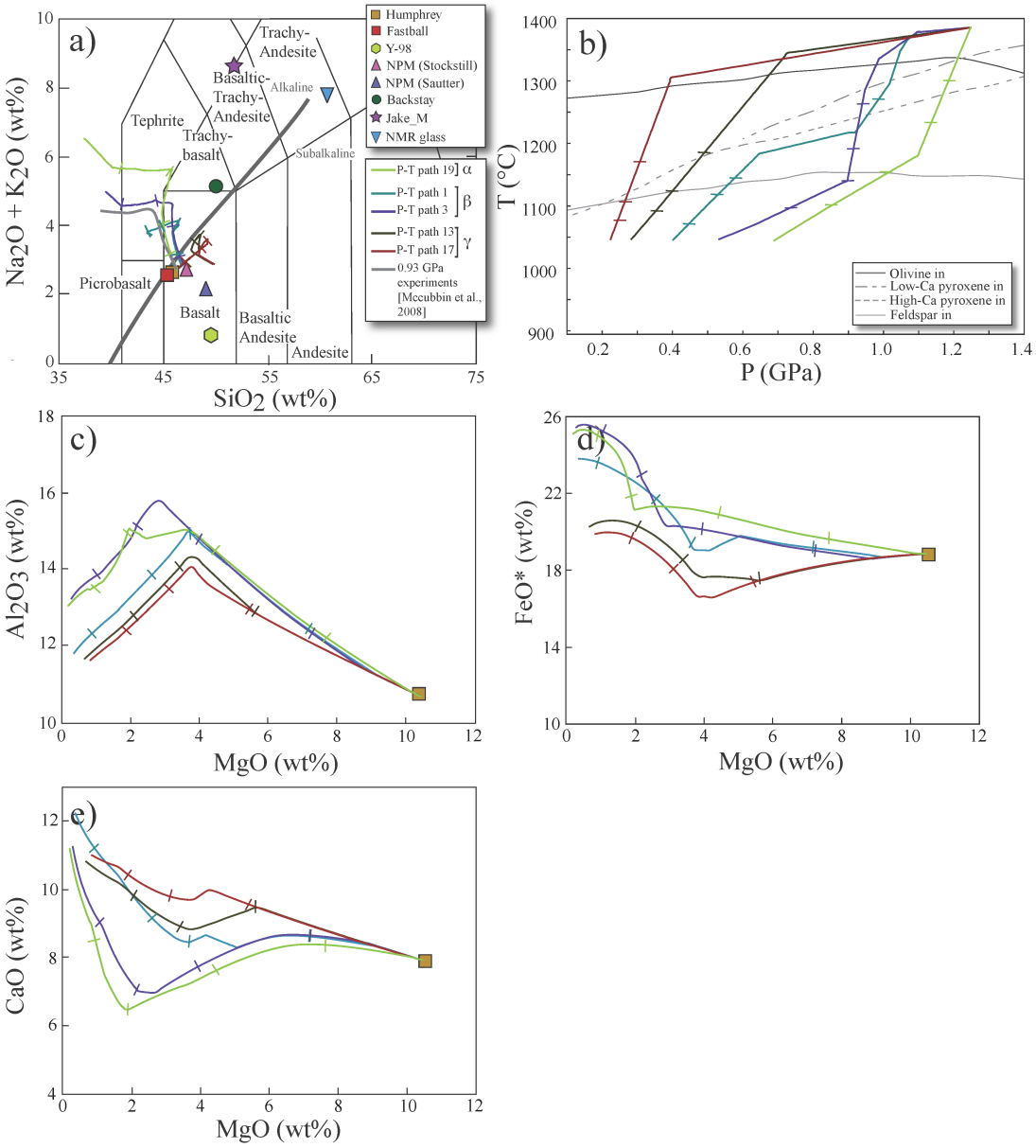

Figure A5. a) Total alkali-silica diagram showing liquid lines of descent calculated with pMELTS for the fractional crystallization of the Humphrey composition with 0.07 wt% H2O at FMQ-2 and P-T paths displayed in b). The liquid line of descent under dry conditions from McCubbin et al. (2008) is indicated in grey. b) P-T paths used to calculate liquid lines of descent in 4a and c-e). Olivine, low-Ca pyroxene, high-Ca pyroxene, and feldspar liquidi are shown as black and gray solid and dashed lines, respectively. Plots of c) Al2O3, d) FeO*, and e) CaO versus MgO for liquid lines of descent. Tick marks delineate 20% fractionation increments.

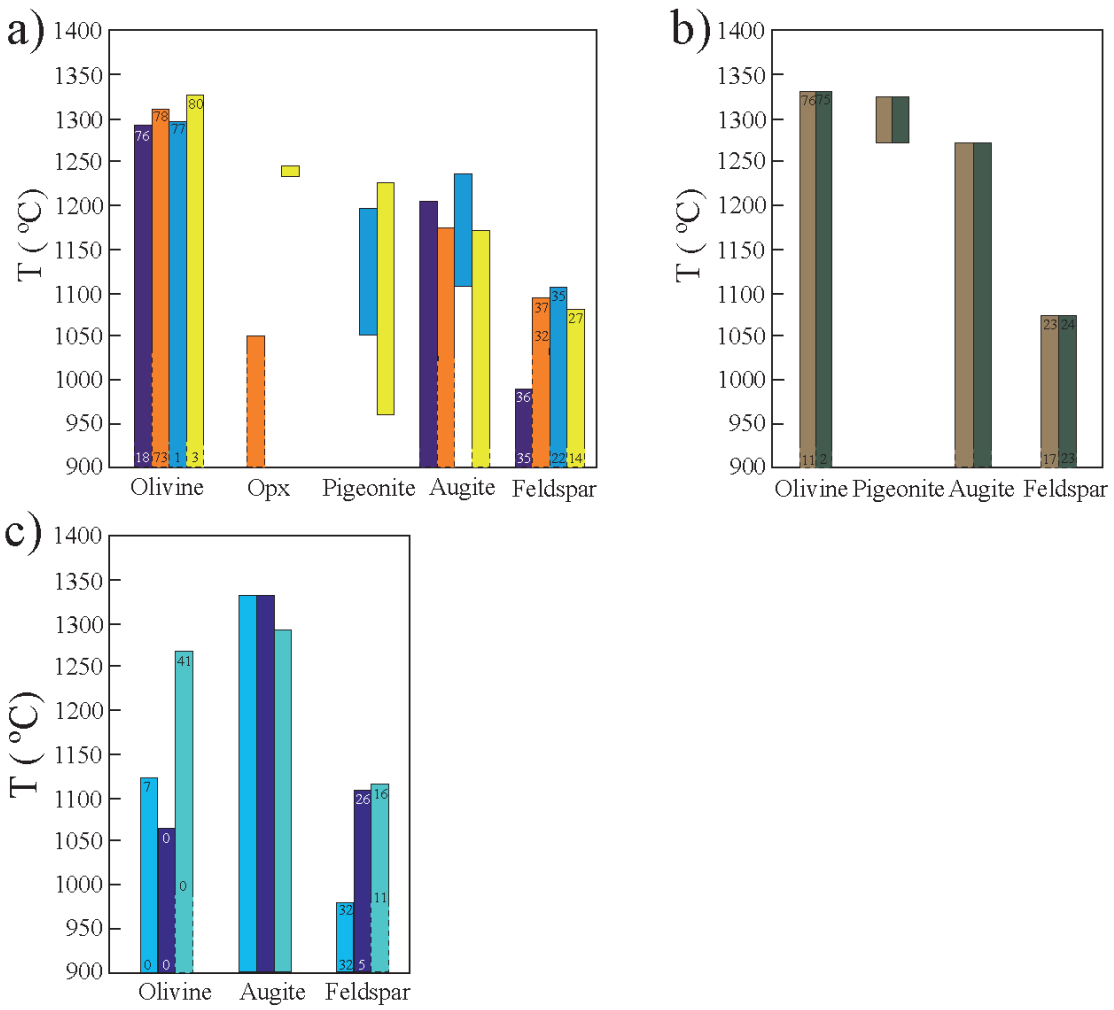

Figure A6. Order of appearance of minerals in the pMELTS and MELTS liquid lines of descent corresponding to the P-T paths in Figures 11, 12, and 13 for Figures a), b), and c) respectively. Numbers in olivine and plagioclase represent the forsterite and anorthite contents respectively.

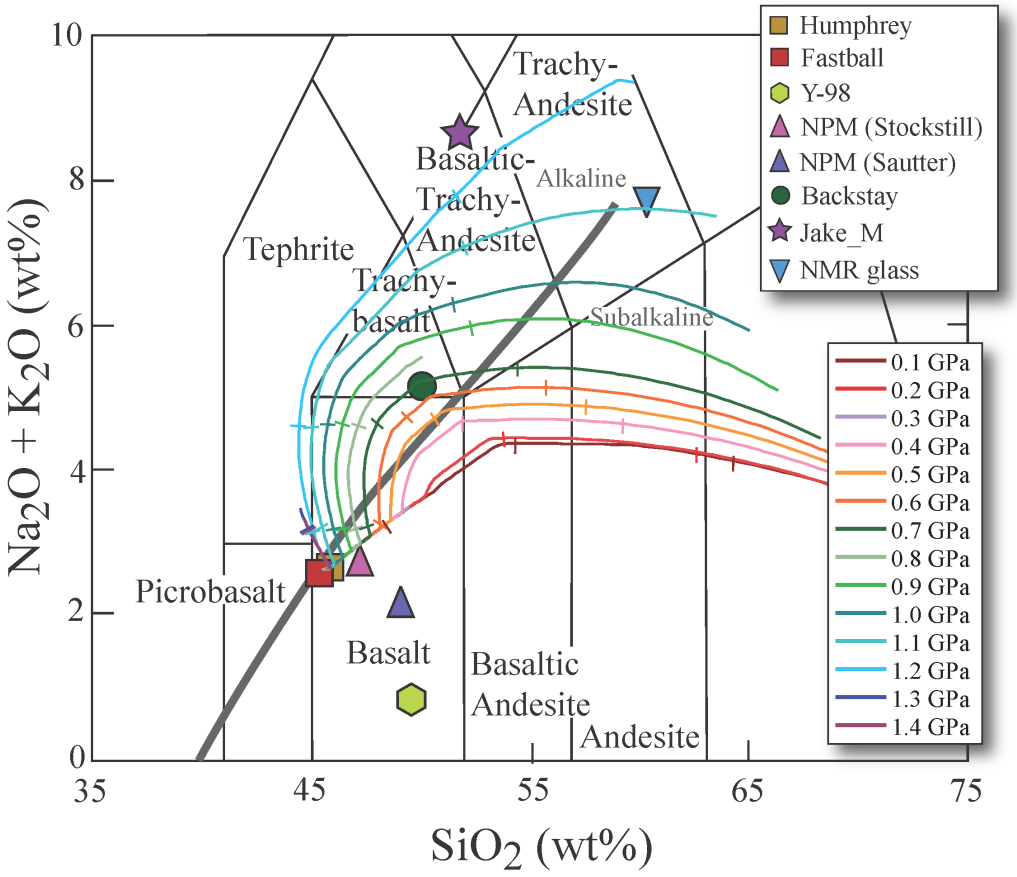

Figure A7. Total alkali-silica diagram showing liquid lines of descent of melts formed by fractional crystallization of Fastball composition, calculated with pMELTS under wet (0.5 wt% H_2O), isobaric conditions from 0.1 to 1.4 GPa at FMQ-1. Tick marks delineate 25% fractionation increments.

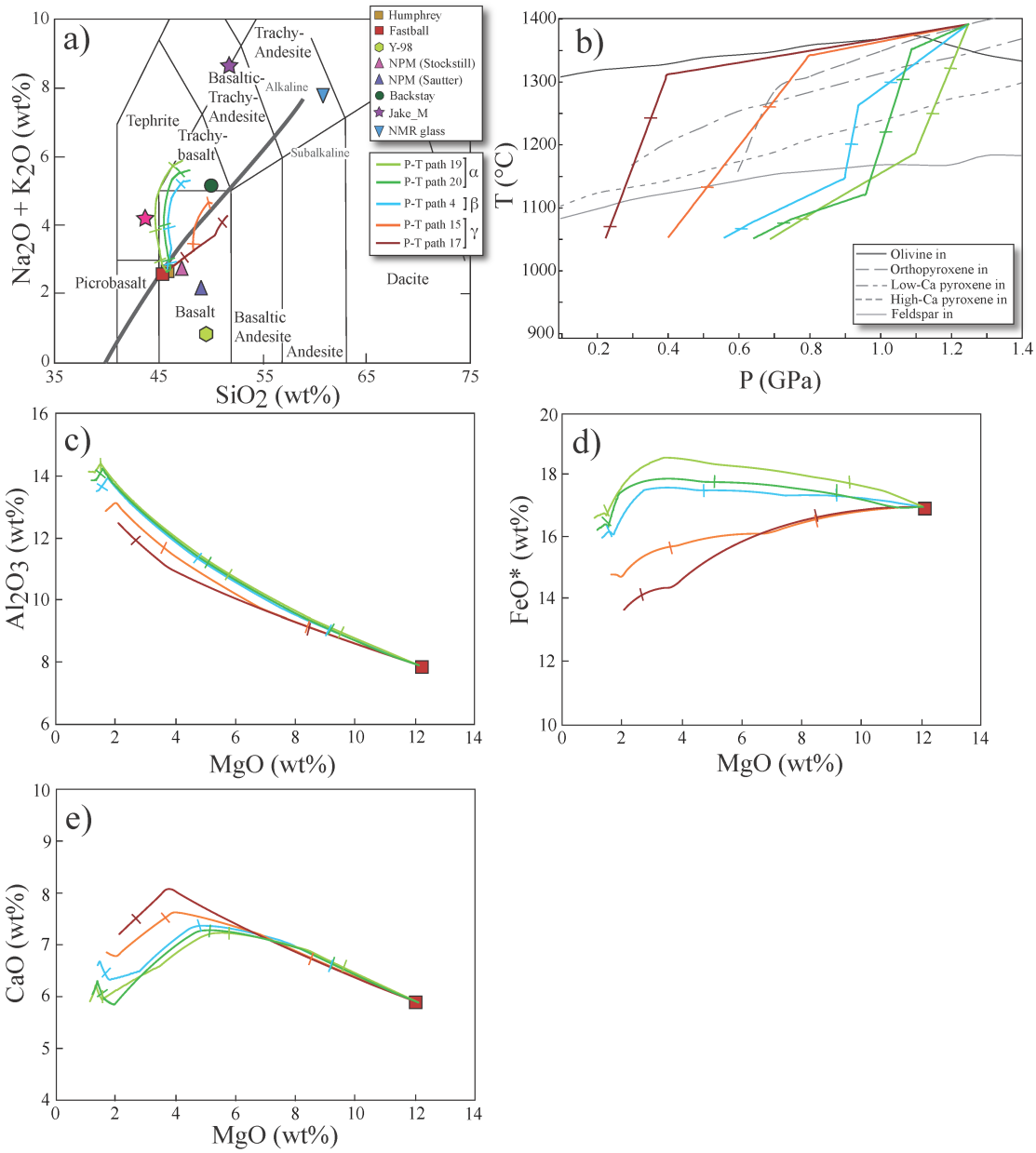

Figure A8. a) Total alkali-silica diagram showing liquid lines of descent calculated with pMELTS for the fractional crystallization of the Fastball composition with 0.5 wt% H_2O at FMQ-1 and P-T paths displayed in b). b) P-T paths used to calculate liquid lines of descent in 8a and c-e). Olivine, orthopyroxene, low-Ca pyroxene, high-Ca pyroxene, and feldspar liquidi are shown as black and gray solid and dashed lines, respectively. Plots of c) Al_2O_3, d) FeO*, and e) CaO versus MgO for liquid lines of descent. Tick marks delineate 20% fractionation increments.

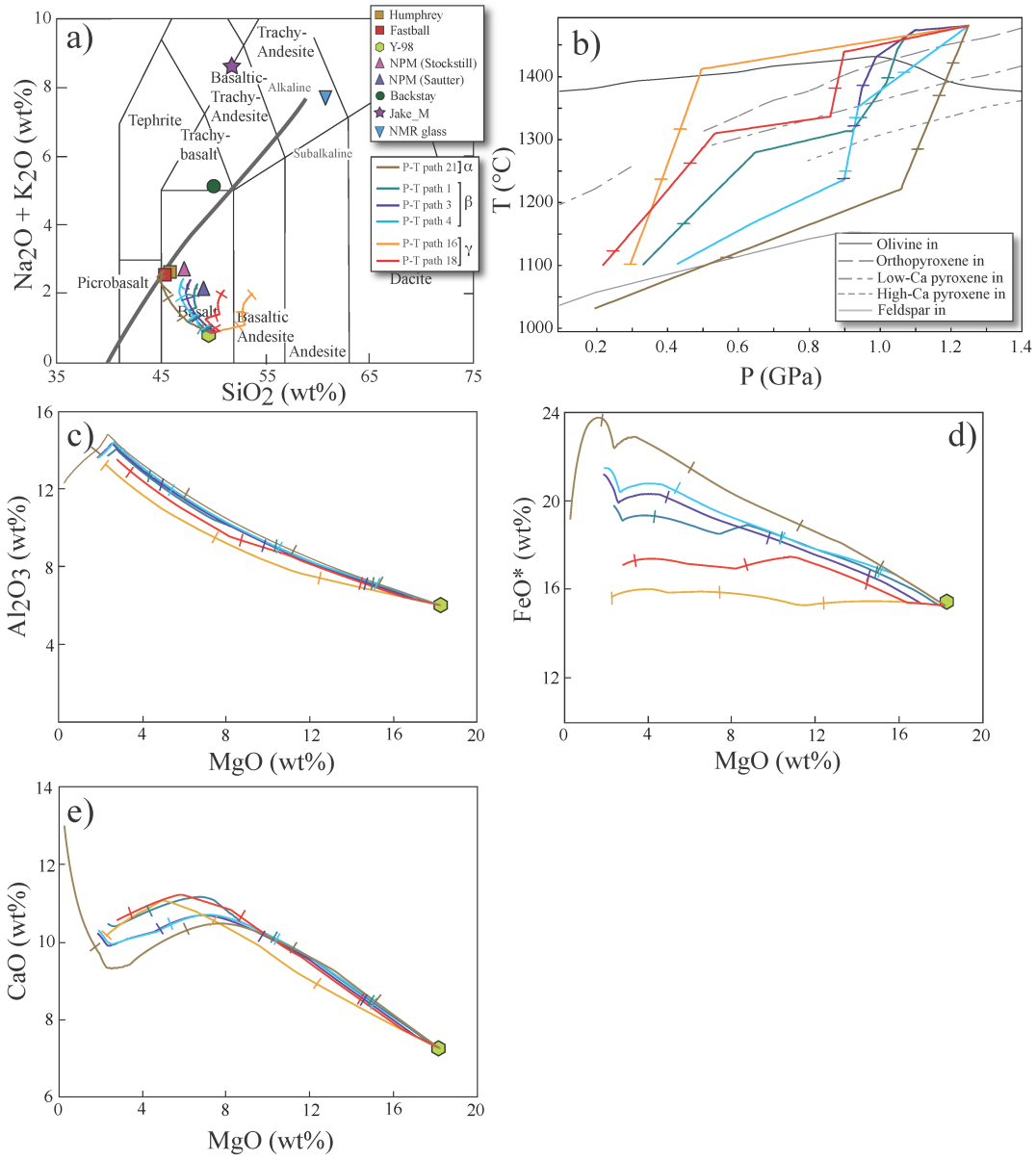

Figure A9. a) Total alkali-silica diagram showing liquid lines of descent of melts formed from fractional crystallization of the Y-98 shergottite composition, calculated with pMELTS under dry, polybaric conditions at FMQ-2.5. b) P-T paths used to calculate liquid lines of descent in 9a and c-e). Olivine, orthopyroxene, low-Ca pyroxene, high-Ca pyroxene, and feldspar liquidi are shown as black and gray solid and dashed lines, respectively. Plots of c) Al_2O_3, d) FeO*, and e) CaO versus MgO for liquid lines of descent. Tick marks delineate 20% fractionation increments.

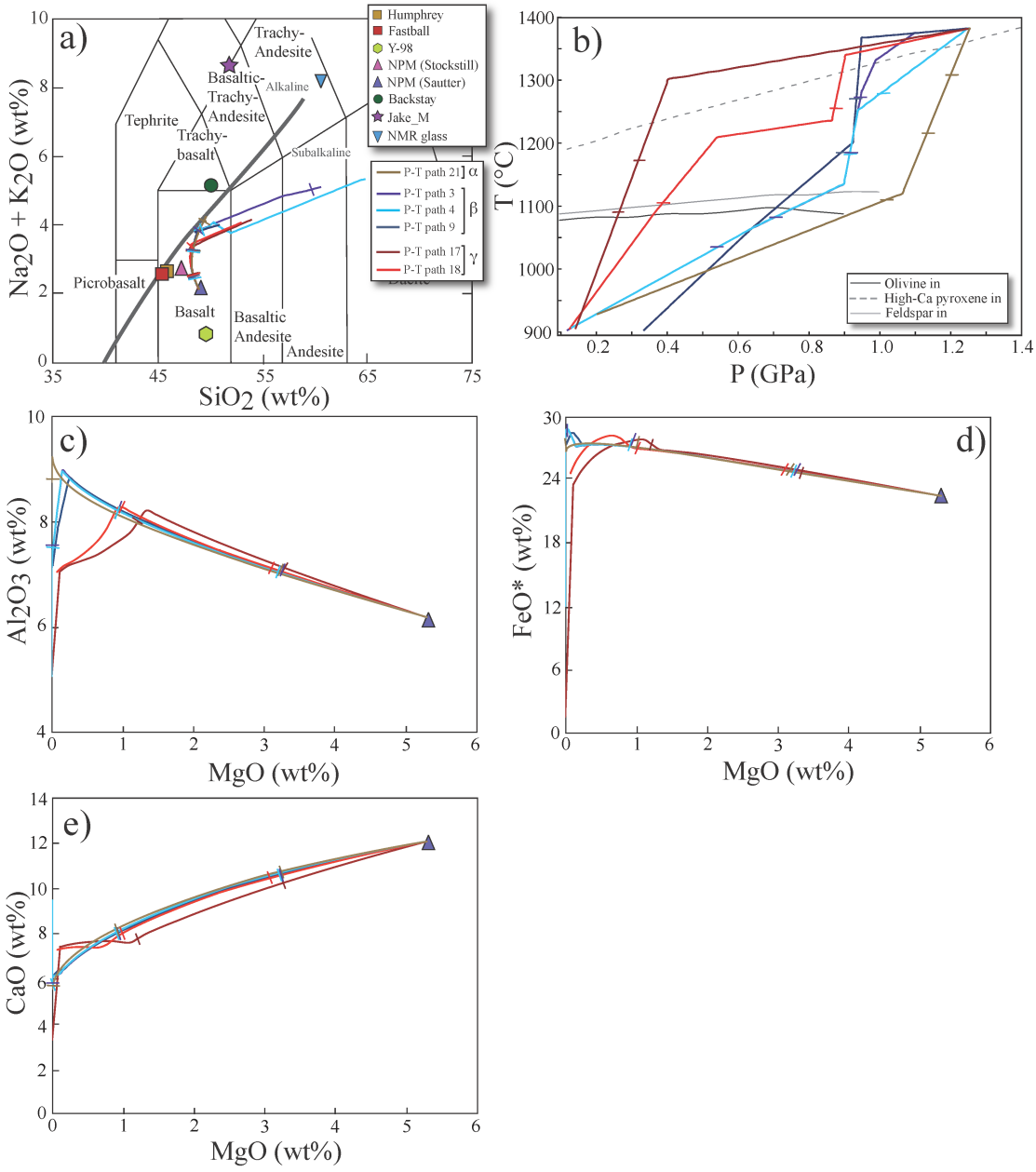

Figure A10. a) Total alkali-silica diagram showing liquid lines of descent of melts formed by fractional crystallization of the nakhlite parental melt composition from Sautter et al. (2012), calculated with MELTS under dry, polybaric conditions at FMQ-1. b) P-T paths used to calculate liquid lines of descent in 10a and c-e). Olivine, high-Ca pyroxene, and feldspar liquidi are shown as black and gray solid and dashed lines, respectively. Plots of c) Al_2O_3, d) FeO*, and e) CaO versus MgO for liquid lines of descent. Tick marks delineate 20% fractionation increments.

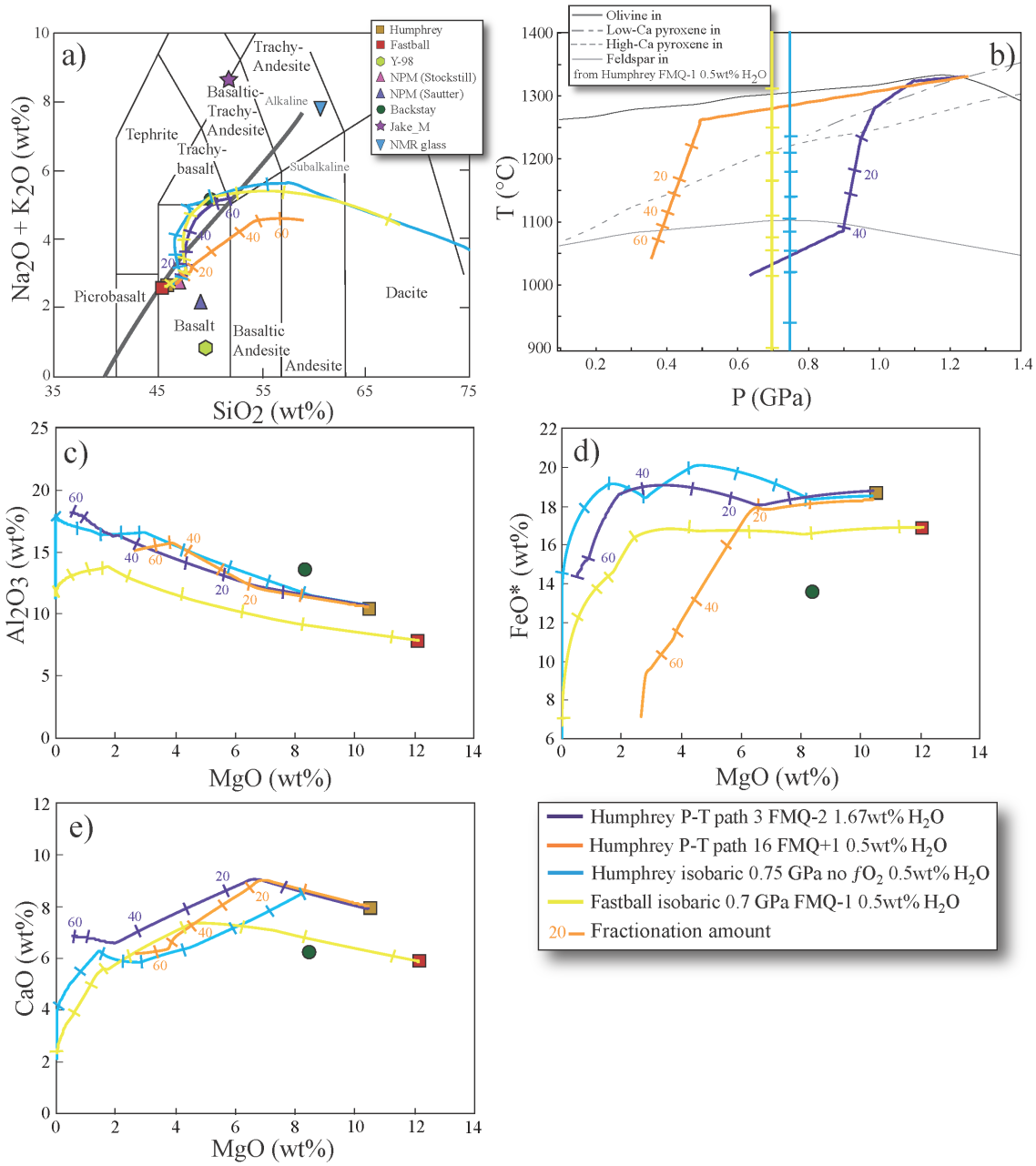

Figure A11. a) Total alkali-silica diagram showing liquid lines of descent of melts formed by fractional crystallization of Humphrey and Fastball compositions under conditions selected because the melts best matched the Backstay major element composition. b) P-T paths used to calculate liquid lines of descent in 9a) and 9c-e). Plots of c) Al_2O_3, d) FeO*, and e) CaO versus MgO for the same liquid lines of descent as in 9a). The tick marks and numbers on the liquid of lines of descent correspond to the amount of fractionation during the ascent of the primary magma (from 10% until 60% fractionation with 10% increments).

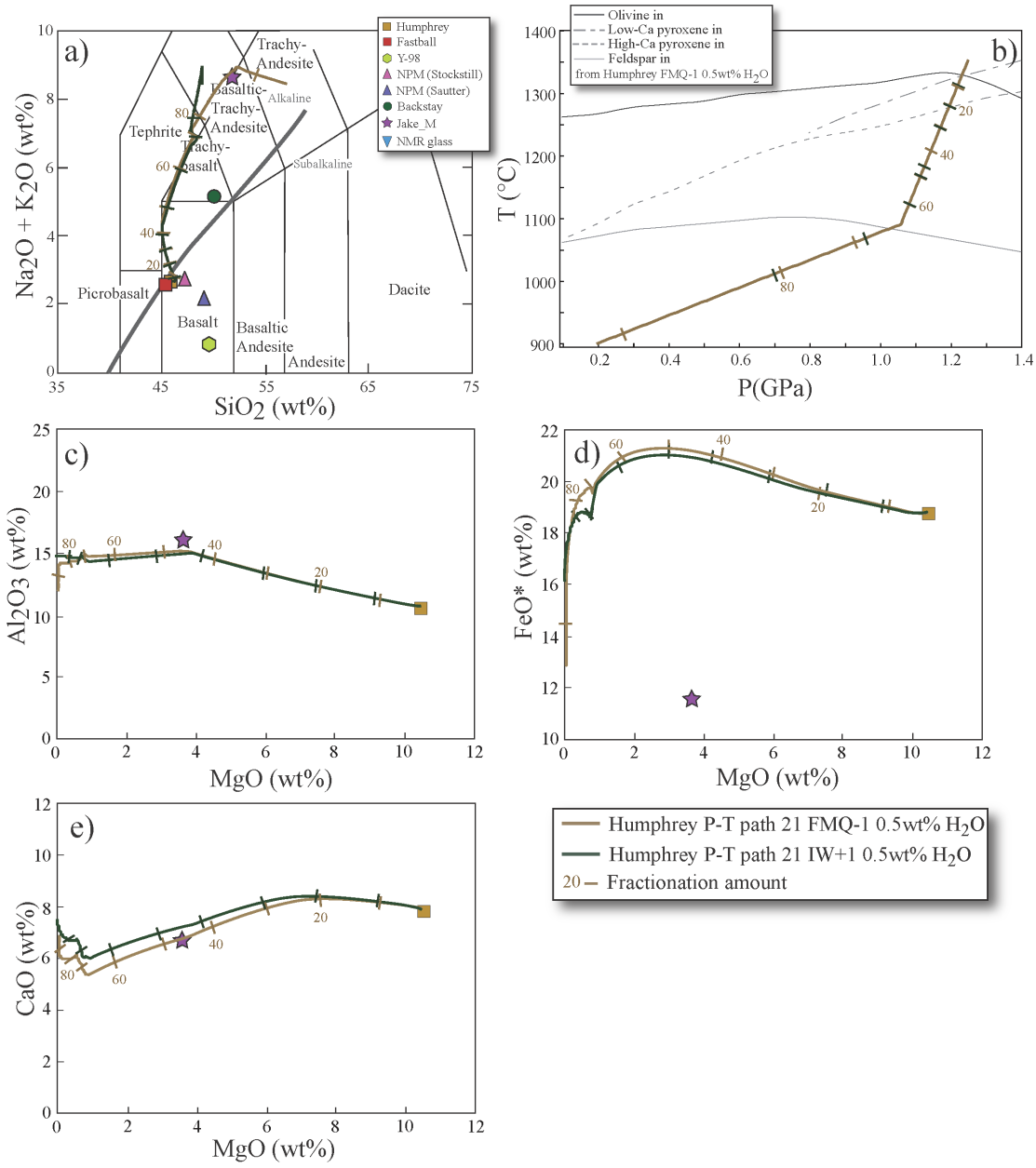

Figure A12. a) Total alkali-silica diagram showing liquid lines of descent of melts formed by fractional crystallization of Humphrey composition under conditions selected because the melts best matched the Jake_M major element composition. b) P-T paths used to calculate liquid lines of descent in 12a) and 12c-e). Plots of c) Al_2O_3, d) FeO*, and e) CaO versus MgO for the same liquid lines of descent as in 10a). The tick marks and numbers on the liquid of lines of descent correspond to the amount of fractionation during the ascent of the primary magma (from 10% until 90% fractionation with 10% increments).

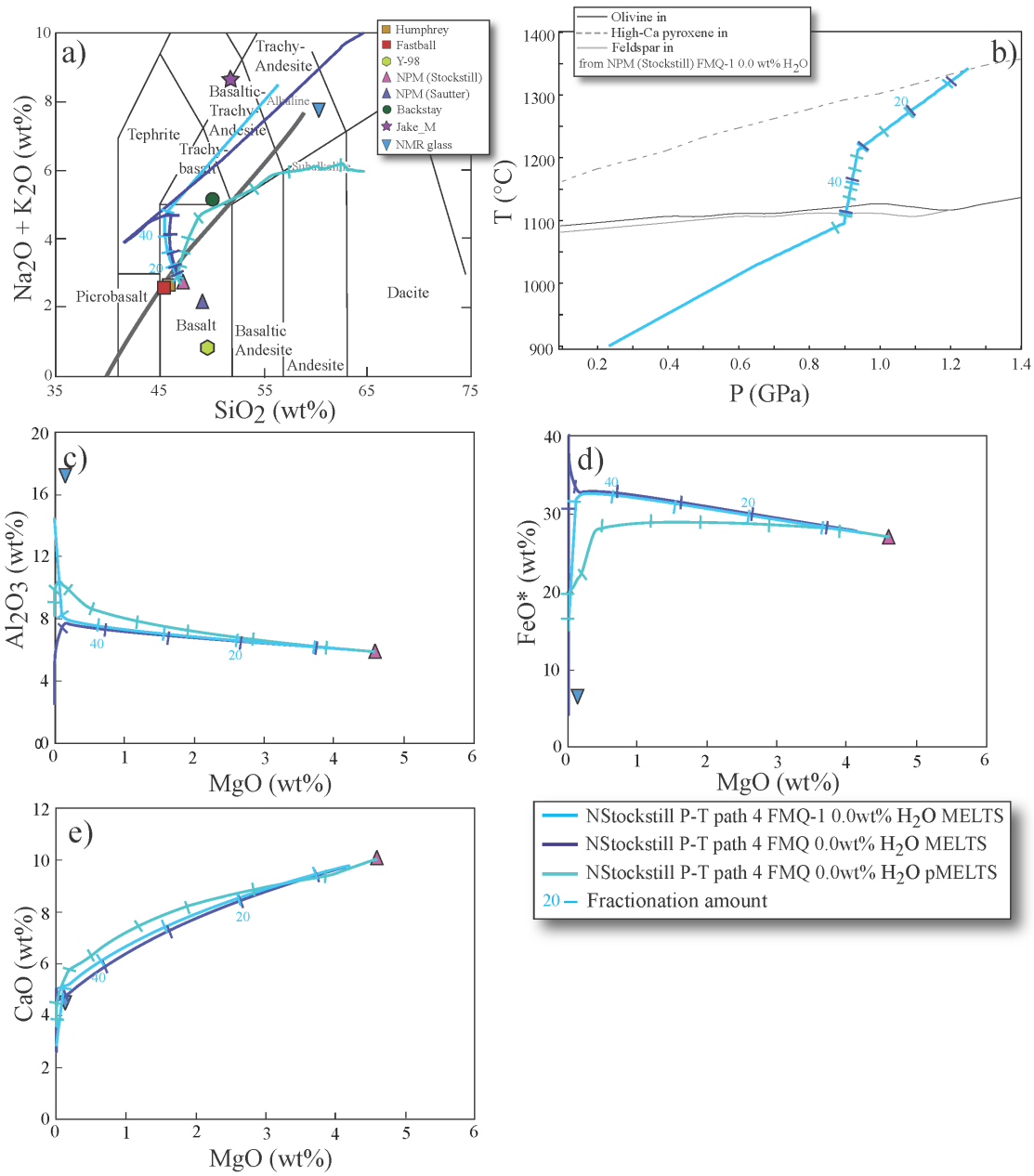

Figure A13. a) Total alkali-silica diagram showing liquid lines of descent of melts formed by fractional crystallization of Humphrey composition under conditions selected because the melts best matched the Miller Range nakhlite intercumulus glass major element composition. b) P-T paths used to calculate liquid lines of descent in 13a) and 11c-e). Plots of c) Al_2O_3, d) FeO*, and e) CaO versus MgO for the same liquid lines of descent as in 11a). The tick marks and numbers on the liquid of lines of descent correspond to the amount of fractionation during the ascent of the primary magma (from 10% until 50% fractionation with 10% increments).

CHAPTER II
LITHIUM ISOTOPES AND LIGHT LITHOPHILE ELEMENT ABUNDANCES IN SHERGOTTITES: EVIDENCE FOR MARTIAN MAGMATIC WATER

This chapter is a reformatted version of a paper of the same name that is being submitted in Meteoritics and Planetary Science. Arya Udry, Rick Hervig, Harry McSween, and Larry Taylor are authors of this paper. Arya performed all the analyses.

Abstract

Degassed magmatic water was potentially the major source of surficial water on Mars. We measured lithium, boron, and beryllium abundances and Li isotope profiles in shergottite pyroxenes, olivines, and maskelynite in four compositionally different shergottites: Shergotty, QUE 94201, LAR 06319, and Tissint, using a secondary ionization mass spectrometer (SIMS). Lithium, B, and Be are incompatible elements; Li and B are soluble in H_2O-rich magmas, whereas Be is insoluble. In the four analyzed shergottites, Li and B concentrations decrease and Be concentration increases from cores to rims in pyroxenes, suggesting water-degassing during magma ascent or eruption. Additionally, abundances of the three elements increase from cores to rims in olivine (a normal igneous fractionation trend), consistent with the crystallization of olivine before magma ascent and degassing. Lithium, B, and Be profiles in the four shergottites are consistent with water-degassing of parental magmas with an average fraction of degassed vapor of ~25%. We expect that ^{6}Li would be mobilized in the vapor phase, compared to ^{7}Li during degassing. The Li isotope profiles indicate water-degassing for only the two depleted shergottites: QUE 94201 and Tissint. Because all depleted shergottites might originate from the same magmatic complex because of their similar Mars ejection ages, and because these two meteorites bracket the crystallization ages of depleted shergottites, it seems likely that all the parental magmas of the depleted shergottites may have undergone water-degassing. Shergotty and LAR 06319, appear to have been affected by diffusion, based on their Li isotope profiles. This process may represent an overlay on a degassing pattern. The light-lithophile element profiles and some of the isotope profiles support the hypothesis that degassing of basaltic and olivine-phyric shergottite magmas could have provided water to the martian surface during the last half-billion years.

Introduction

The former occurrence of liquid water on Mars has been confirmed by numerous observations and measurements of spacecraft and rovers, most recently by the identification of an ancient stream bed by the Curiosity rover in Gale Crater (Williams et al., 2013) and the discovery of clay minerals by the Opportunity rover in Endeavour Crater (Arvidson et al., 2014). Because water is critical to life, it is important to understand its potential sources, quantities, and surface residence times during martian history. Surficial water is primarily derived from magmatic sources. It is stored deep inside the martian crust/mantle and exhaled in the form of water-vapor during magmatic eruptions. However, the role of magmatic water in the petrogenesis of martian basalts is still controversial. The samples of martian basalts that can be analyzed in the laboratory are meteorites (shergottites). Bulk-shergottite compositions are typically very dry and do not display mineralogical evidence for magmatic water, leading to the idea that these

magmas were almost anhydrous (Dreibus and Wänke, 1985). Thus, if shergottites contained magmatic water, it had to have been efficiently degassed during ascent or eruption (Wilson and Head, 1981).

Various approaches have been applied to address the possibility of magmatic water in shergottites. These approaches include the presence of hydrous phases in trapped melt inclusions, OH analyses in apatite, studies of H and O isotopic compositions, and soluble light-lithophile element (LLE: Li, B, Be) zoning in pyroxenes. Treiman (1985) showed that pre-eruptive H_2O (at least 0.2 wt%) was present in the parental magmas of Shergotty and Zagami, by identifying hydrous kaersutite in melt inclusions. Calculations using amphibole-bearing melt inclusions in shergottites by McSween and Harvey (1993) suggested that some martian magmas contained an average of 1.4 wt% H_2O. These early results implied that the martian interior is wetter than previously thought (Dreibus and Wänke, 1985). Using O isotopes in martian meteorites, Karlsson et al. (1992) argued that a hydrosphere reservoir exists on Mars. Boctor et al. (2003) showed that Shergotty, Zagami, and SaU 005 display mixing of high and low δD components, the high δD component probably derived from a martian exchangeable reservoir and the low δD component representing a primary magmatic component or a terrestrial contaminant. Usui et al. (2012) also found using H isotopes that some primitive shergottites retain undegassed-water in melt inclusions. In addition, experiments from Dann et al. (2001) showed that water (1.8 wt% H_2O) had to have been present in the parent magma in order to form the measured pyroxene-core composition. More recently, McCubbin et al. (2012) analyzed hydrous apatites in Shergotty and QUE 94201 and calculated that the parent magmas contained 730-2130 ppm H_2O. Boyce et al. (2014) mentioned that lunar hydrous apatites might not indicate the water content of their parental magmas, due to the less incompatible ions of F and Cl, versus OH. However, it is not clear if that problem applies to martian apatites. Lithium, B, and Be measurements have also been used, as discussed below.

In this study, we investigate Li, B, and Be abundances, which have different solubilities in H_2O-rich fluids, as well as Li isotopic compositions in igneous minerals (pyroxene, olivine, and maskelynite), to address the occurrence of water in shergottite parental magmas. *In situ* analyses of Li, B, and Be were first conducted in Shergotty and Zagami pyroxenes by Lentz et al. (2001) and McSween et al. (2001) using secondary ion mass spectrometry (SIMS). Shergotty and Zagami (and other basaltic shergottites) contain pigeonite and augite grains with Mg-rich cores, Fe-rich rims, and interstitial maskelynite. As Li^+ has a similar radius to $Mg^{2+}$and is incompatible, it can easily substitute for Mg in pyroxene and olivines and increasingly during fractionation (Tang et al., 2007). Stolper and McSween (1979) postulated that pyroxenes in basaltic shergottites underwent two-stages of crystallization: the cores crystallized at depth, separated by a halt in nucleation, and followed by formation of Fe-rich rims during ascent or eruption. This crystallization history is supported by crystal size distribution analyses of Shergotty pyroxenes (Lentz and McSween, 2000). Pyroxene growth was thought to have been accompanied by magma devolatilization (Lentz et al., 2001; McSween et al., 2001). Lithium, B, and Be are incompatible in olivine, pyroxene, and plagioclase during crystallization of dry magmas (Brenan et al., 1998). Boron and Li are soluble in H_2O-rich

fluids, whereas Be is insoluble. During magmatic crystallization, an increase in all three elements would be predicted from cores to rims in these minerals. However, Lentz et al. (2001) analyzed the cores and rims of Shergotty and Zagami pyroxenes, and showed that [Li] and [B] decrease whereas [Be] increases (hereafter, brackets denote element abundances in ppm). They argued that Li and B were carried away in exsolved aqueous fluids, so that the late-stage Fe-rich rims crystallized from magma that was depleted in the soluble elements (Lentz et al., 2001; McSween et al., 2001; Herd et al., 2005). The degassing hypothesis was supported by Beck et al. (2004), who examined the LLE abundances and Li isotopes in augite of the basaltic shergottite NWA 480. They inferred that Li isotopic fractionation was to be expected with degassing (i.e., ^{7}Li will be depleted relative to ^{6}Li in the volatile phase). Notably, this work is one of the few studies conducted on Li isotopes *in situ* in shergottites.

Several studies have argued that LLE zoning cannot be used as evidence for magma degassing or that a significant amount of water was not even present in the martian mantle. Because Li diffuses rapidly in minerals, several authors postulated that the zoning of LLE abundances and Li isotopic ratios in martian meteorite pyroxene are result of post-crystallization solid-state diffusion (Treiman et al., 2006; Beck et al., 2006). Thus, there is still some controversy about magmatic water and related Li studies. Further work is needed to reconcile these contradictory conclusions about the occurrence of martian magmatic water as revealed by LLE and Li isotope behavior in shergottite minerals. Additional measurements of zoning of LLEs and Li isotopes in shergottites could potentially yield important new information about the origin of surficial martian water and advance our understanding of possible magma degassing processes on Mars.

To address the contradictory results from previous studies, we measured LLE profiles and trace-element concentrations as well as Li isotope (^{7}Li and ^{6}Li) profiles, in pyroxene, maskelynite, and olivine in four compositionally different shergottites (Fig. B1): two basaltic shergottites (Shergotty and QUE 94201) and two olivine-phyric shergottites (LAR 06319 and Tissint). We measured profiles rather than only point analyses of pyroxene cores and rims: diffusion profiles might be distinguishable from degassing profiles, whereas they would not be in point analyses.

Samples and analytical procedures

Analyzed samples

Shergottites can be distinguished by their crystallization ages, major- and trace-element compositions, modes, textures, and magma-source regions (which can be geochemically enriched or depleted). These meteorites are commonly divided into three different petrologic classes: basaltic, olivine-phyric, and lherzolitic, but the latter are plutonic rocks and thus, may be less likely to have lost volatiles. Shergottites can be geochemically classified as enriched or depleted in light rare earth elements (LREE). Depleted shergottites, such as QUE 94201 and Tissint, have low La/Lu, low initial ^{87}Sr/^{86}Sr, high initial ε^{143}Nd, and formed under relatively reducing conditions, whereas enriched shergottites, such as Shergotty and LAR 06319, display high La/Lu, high initial ^{87}Sr/^{86}Sr, low initial ε^{143}Nd, and are oxidized (e.g., Bridges and Warren, 2006). The

properties of the depleted and enriched shergottites represent their mantle sources. The cause of the enrichment of some shergottites is debated; it could be a result of: an enriched mantle source (e.g., Bridges and Warren, 2006; Usui et al., 2012) or assimilation of enriched crust (e.g., McCubbin et al., 2012). We selected four martian meteorites that span both the shergottite compositional and age ranges. We also opted for shergottites that are only moderately shocked, and that have large enough pyroxene and olivine grains to conduct SIMS analyses. Pyroxenes and olivines in these samples all display Fe-Mg zoning, indicating multiple-stage growth history, which is potentially also reflected in LLE and Li isotope zoning. For each shergottite, we analyzed pyroxene and olivine grains with the highest Mg# in their cores, indicating sections probably through the centers of grains.

- Shergotty is an enriched basaltic shergottite, with a crystallization age of 165 ± 1 Ma (Stöffler et al., 1986). It consists of pigeonite and augite with Mg-rich cores and Fe-rich rims enclosed by interstitial maskelynite, with minor magnetite, ilmenite, phosphate, and silica (Stolper and McSween, 1979). Estimates of the water content of the Shergotty parental magma range from 50 ppm to 1.8 wt% (Wänke and Dreibus, 1994; Dann et al., 2001; McCubbin et al., 2012).

- QUE 94201 is a depleted basaltic shergottite with a crystallization age of 327 ± 10 Ma and represents a near-primary melt composition (McSween et al., 1996). Similar to Shergotty, it consists of pigeonite and augite with interstitial maskelynite, with minor ilmenite, ulvöspinel, phosphate, and silica. The pyroxene is zoned with Mg-rich pigeonite cores, augite mantles, and Fe-rich pigeonite exterior rims. It is more evolved than other shergottites, with more Fe-rich pyroxenes and higher phosphate contents. Prior estimates of the water content of its parental magma range from 730-2130 ppm (McCubbin et al., 2012).

- LAR 06319 is an enriched olivine-phyric shergottite with a crystallization age of 193 ± 20 Ma (Peslier et al., 2010; Shafer et al., 2010; Balta et al., 2013). Similar to QUE 94201, it represents a near-primary melt composition with very limited crystal accumulation (Basu Sarbadhikari et al., 2009). LAR 06319 shows zoning in pyroxenes that is similar to that in QUE 94201, with pigeonite cores, augite mantles, and Fe-rich pigeonite exterior rims. The only prior estimate of the water content of its parental magma is 1.1 wt% (Balta et al., 2013). A multiple-stage growth history is also indicated for the olivine-phyric shergottites (Usui et al., 2008): (1) formation of olivine megacrysts, either as phenocrysts, xenocrysts, or antecrysts; (2) crystallization of groundmass olivine and pyroxene cores, possibly during magma ascent; (3) further crystallization of plagioclase and pyroxene rims, possibly on eruption.

- Tissint is a depleted olivine-phyric shergottite, with a crystallization age of 574 ± 20 Ma (Brennecka et al., 2014). It exhibits mineralogy similar to LAR 06319 with megacrysts of olivines and interstitial zoned pyroxene, olivine, and maskelynite. Tissint contains various high-pressure phases indicating elevated shock pressures (Baziotis et al., 2013). No estimate of water content for the parental magma of this meteorite has been published.

Analyses of major and minor elements

In situ major- and minor-element compositions were determined using the CAMECA SX-100 electron microprobe (EMP) at the University of Tennessee. Operating conditions for the analyses of pyroxene, olivine, and maskelynite were an accelerating voltage of 15 kV, beam currents of 20 nA (pyroxene and maskelynite) to 30 nA (olivine), and beam sizes varying from 2 μm (pyroxene and olivine) to 10 μm (maskelynite) using the wavelength dispersive (WDS) mode and standard PAP corrections. The counting times for all elements were 20 s, except for Ca (30 s), Cr (30 s), and Ni (50 s) in olivine. The detection limits (3σ above background) were 0.03 wt% for SiO_2, TiO_2, Al_2O_3, MgO, CaO, NiO, P_2O_5, Na_2O, and K_2O and 0.05 wt% for FeO, MnO, and Cr_2O_3. Both natural and synthetic standards were used for calibration.

Analyses of trace elements and stable isotopes

Trace-element concentrations (Li, B, Be, Ti, Sr, Y, Zr, and Ce) and Li isotope ratios were obtained using the CAMECA Ims 6f SIMS at Arizona State University. We measured as many points as possible along pyroxene profiles, but it was a difficult task as shergottite pyroxenes exhibit numerous fractures and inclusions. After polishing, thin sections were washed in a 1.82% manitol solution for at least 2 hr to reduce B contamination, shown to result surface concentrations of B to <5 ppb (e.g., Guild et al. 2013). The thin sections were then dried and gold-coated. SIMS analyses were conducted using a 10 nA O^- beam with a diameter of 50-60 μm. The mass spectrometer was operated at mass-resolving power sufficient to resolve $^9Be^+$ from $^{27}Al^{3+}$ (M/ΔM of about 900). Areas of interest were pre-sputtered for ~4 min to achieve steady-state count rates. Trace ion intensities (normalized to the $^{30}Si^+$ count rate) were used to determine concentrations. The signals at the masses of interest, i.e., $^7Li^+$, $^9Be^+$, $^{11}B^+$, $^{47}Ti^+$, $^{88}Sr^+$, $^{89}Y^+$, and $^{90}Zr^+$, were integrated for 2 s per cycle, while $^{140}Ce^+$ was counted for 10 s. Each analysis consisted of 20 cycles of measurement. Each ^6Li and ^7Li isotopic analysis consisted of 100 cycles of measurement.

The M^+/Si^+ ratios on the unknowns were compared with the ion ratios determined on NIST 610 glass (Jochum et al., 2011) to determine concentrations in pyroxene, olivine, and maskelynite (after correction for different silica concentrations). The basaltic glass standards GSC-1G (δ^7Li = 24.1‰ and 4.9 ppm of Li) and BCR-2G (δ^7Li = 4.0‰ and 7.5 ppm of Li) were used for calibrating the Li isotope measurements in pyroxene and maskelynite (Kassemann et al., 2005). The relative error for the LLE corresponds to approximately 1 % of each analysis. We used the international carbonate standard L-SVEC for lithium isotopes ($^7Li/^6Li_{L\text{-}SVEC}$ = 12.0192, Flesch et al. 1973). The isotope ratios are reported here as differences in per mil (‰) relative to the L-SVEC standard (Flesch et al., 1973) as: $\delta^7Li=((^7Li / {}^6Li)_{sample} / 12.0192)-1) \times 1000$. Olivine shows a significant effect of Fe/Mg ratio on the calibration for Li isotopes (Bell et al., 2009), so lithium isotopes were not measured in this mineral.

In situ trace-element and lithium-isotopic compositions

Major- and trace-element abundances and Li isotopic data are presented in Tables B1-3.

Shergotty – Lithium ([Li]) and B ([B]) abundances in Shergotty pyroxenes decrease from cores (4.40 ppm for [Li] and 4.14 ppm for [B]) (Fig. B2a) to rims (2.00 ppm for [Li] and 3.70 ppm for [B]); [Li] is negatively correlated with Fe# (Figs. B3a-b). Shergotty pyroxene show a general [Li] depletion from cores to rims of 55 %. Beryllium abundances increase from cores (0.003 ppm) to rims (0.012 ppm) and are positively correlated with Fe# (Fig. B3c). The trace-element abundances measured in Shergotty pyroxene are consistent with data from previous studies (e.g., Wadhwa et al. 1994; McSween et al. 2001; Lentz et al. 2001; Herd et al. 2005). The δ^7Li in Shergotty pyroxenes varies from -2.2 to +6.2 ‰. Values of δ^7Li in Shergotty pyroxenes do not show a clear correlation with Fe#, despite the fact that px-2 and px-3 appear negatively correlated with Fe# (Fig. B4). Profiles of δ^7Li in px-2 and px-3 exhibit a "W" shape, whereas one rim of px-1 shows δ^7Li depletion (Fig. B5). Most pyroxene rims are in contact with maskelynite, whose Li concentrations in Shergotty range from 0.9 to 4.8 ppm and δ^7Li from -1.4 and -5.6 ‰ (Table B2).

QUE 94201 – Lithium abundances in QUE 94201 pyroxenes decrease from cores (1.25 ppm) to rims (0.87 ppm) (Fig. B2b) and are negatively correlated with Fe#. QUE 94201 pyroxenes show [Li] depletions from cores to rims of 31%. Be and B abundances are below the limits of detection. Values of δ^7Li in QUE 94201 pyroxene varies from -6.0 ‰ to +45.4 ‰, with up to ~40 ‰ difference from cores to rims in px-2 (Table B1, Fig. B5). Values of δ^7Li is positively correlated with Fe# (Fig. B4). The Li isotopic profiles show a δ^7Li increase from core to rim except for px-1 and px-3, which exhibit δ^7Li depletions at one of their rims. The δ^7Li depletion in these two pyroxenes is at the contact with ilmenite, whereas the other side of the crystals is in contact with maskelynite. Lithium concentrations in QUE 94201 maskelynite range from 3.9-5.4 ppm and δ^7Li from -5.3 and +4.4 ‰.

LAR 06319 - Lithium abundances in LAR 06319 pyroxenes decrease from cores (3.12) to rims (1.17 ppm) (Fig. B2c) and are negatively correlated with Fe# (Fig. B3). Beryllium and B abundances increase from pyroxene cores (0.02 ppm for [Be] and 0.47 ppm for [B]) to rims (0.13 ppm for [Be] and 1.47 ppm for [B]) (Fig. B3). LAR 06319 shows a 62 % [Li] depletion from cores to rims. Lithium abundances in LAR 06319 olivines increase from cores (2.00 ppm) to rims (3.26 ppm) (Fig. B2e), with positive correlation with Fe# (Fig. B6). Boron and Be abundances in olivine are both below the limits of detection. Values of δ^7Li in LAR 94201 pyroxenes vary from -9.2 to +12.7 ‰ (Table B3). Only one pyroxene (px-1) shows δ^7Li enrichment from core to rim, whereas the three other pyroxenes exhibit δ^7Li depletions toward their rims (Fig. B5). Lithium concentrations in LAR 06319 maskelynite range from 3.0-3.1 ppm and δ^7Li from -16.8 to -5.3 ‰. Note that only three analyses of maskelynite were measured in LAR 06319, due to the small grain sizes of maskelynite in this meteorite.

Tissint - Lithium abundances in Tissint pyroxenes decrease from cores (1.55 ppm) to rims (1.24 ppm) (Fig. B2d) and are negatively correlated with Fe# (Fig. B3). Tissint

shows [Li] depletion from cores to rims of 20 %. Conversely, [Li] in Tissint olivines increases from cores (0.59 ppm) to rims (1.07 ppm) (Fig. B2f) and shows a positive correlation with Fe# (Fig. B6). Boron and Be abundances in pyroxenes and olivines are below the limits of detection. Values of δ^7Li in Tissint pyroxenes vary from -10.6 to +5.1 ‰. All the δ^7Li profiles increase from core to rim, with a variation in a single crystal up to ~8 ‰ (px-1: Fig. B5). Additionally, δ^7Li values in Tissint pyroxenes show a positive correlation with Fe#. Lithium concentrations in Tissint maskelynite range from 1.1-1.4 ppm and δ^7Li from -6.6 and -4.3 ‰ (Table B3). Only two maskelynites were analyzed, due to the small grain size.

In summary, in shergottite pyroxenes, [Li] and [B] generally decrease from core to rim and show an inverse correlation with Fe#, whereas [Be] increases from core to rim. These results are consistent with those of Lentz et al. (2001) who measured LLE abundances in Shergotty and Zagami; however, we measured profiles and these authors only measured points in pyroxene cores and rims. Conversely, [Li] in olivine increases with Fe#, which indicates a normal igneous fractionation. Profiles of δ^7Li in pyroxenes are not as consistent as Li concentrations, with only QUE 94201 and Tissint showing consistent δ^7Li enrichment from cores to rims. Other incompatible-trace elements (e.g., Zr, Ti, Y, Sr, and Ce) record a normal igneous fractionation as their concentrations increase with Fe# in both pyroxene and olivine (Fig. B7 and Tables B1-2).

Discussion

Previous studies (e.g., Beck et al., 2006; Treiman et al., 2006) have suggested that the observed δ^7Li and LLE abundance profiles of pyroxene and olivine crystals in shergottites could be the result of either magmatic water degassing or sub-solidus and magmatic diffusion. Here we use LLE and δ^7Li profiles in shergottite pyroxenes, olivines, and maskelynite to determine which of these three processes is responsible for the observed zoning. We can first state that regardless of whether the studied profiles represent magmatic or diffusional processes, they were not significantly affected by subsequent aqueous alteration or shock metamorphism. Evidence of alteration, such as secondary mineral formation, is very limited in the four studied shergottites (e.g., McSween et al., 1996; Basu Sarbadhikari et al., 2009; Brennecka et al., 2014). Additionally, the shock pressures and temperatures of shergottites and nakhlites during their ejection from Mars, should not have erased their mineral zoning patterns (Chaklader et al., 2005; Beck et al., 2006).

Closed-system magmatic fractionation

If shergottite pyroxenes crystallized from fractionating liquids in a closed-system, no volatile loss would have occurred. However, the observed [Li] variations found in all the measured pyroxenes cannot be explained by closed-system fractionation. It has been previously shown that Li isotopes do not undergo fractionation during magmatism (Tomascak et al., 2004; Seitz et al., 2006; Jeffcoate et al., 2007). Consequently, the observed Li isotopic variations may indicate open-system events, such as degassing. Likewise, no assimilation-fractionation crystallization (AFC) processes (DePaolo, 1981)

occurred due to the fact that Zr, Sr, Y, and Ce behaved as expected during normal fractionation (e.g., Herd et al. 2005, Fig. B7, Tables B1-3).

Water degassing of shergottite parental magmas

The [Li] and [B] depletion in pyroxene rims likely indicate water-degassing during magma ascent, as both elements escape with the volatile phase, as argued in previous studies (e.g., Lentz et al., 2001; McSween et al., 2001; Beck et al., 2004; Herd et al., 2005). Magma degassing has been shown to be a common process in diverse terrestrial magmas (e.g., Berlo et al., 2004). On Mars, the ease of vapor escape can be amplified by the fact that the martian gravity and atmospheric pressure are relatively low compared to terrestrial conditions (Wilson and Head, 1981).

The zoning profiles obtained in this study confirm that [Li] decreases from cores to rims in pyroxenes, whereas [Be], which is not soluble in H_2O-fluids, shows a normal igneous fractionation trend. In general, pyroxene rims in the depleted shergottites are depleted in [B] compared to the cores, as predicted by degassing. Paradoxically, [B] in LAR 06319 pyroxenes show increase from cores to rims. Perhaps this might be explained by B contamination or by the fact that our B data are close of the limit of detections. Additionally, olivine trace element profiles in LAR 06319 and Tissint reflect a normal igneous trend, and were likely not affected by degassing. This result is consistent with conclusions of previous studies that olivine was the earliest crystallizing phase in olivine-phyric shergottites and may have been fully formed before magma ascent (Usui et al., 2008), with subsequent magma degassing. Consequently, LLE abundance profiles in shergottite pyroxenes and olivines are consistent with water-degassing during ascent of their parental magmas.

Regarding Li isotopes, no experimental data exists for the isotopic fractionation factor (α) between vapor and basaltic melt. However, Beck et al. (2004) calculated α = 0.966 and 0.978, using different gas species (Li_2O and Li_2S), using fractionation calculations from Davis et al. (1990). These fractionation factors suggest that ^6Li should be preferentially mobilized in the vapor phase compared to ^7Li, as might be expected from volatilization. Consequently, δ^7Li would increase from cores to rims in pyroxenes. Tissint is the only shergottite that shows such consistent δ^7Li profiles, which exhibit enrichment in the heavy isotope toward pyroxene rims. Depletion of δ^7Li in QUE 94201 px-1 and px-3 rims in contact with ilmenite might be explained by diffusion of ^6Li from ilmenite to pyroxene.

Additionally, degassing in the olivine-phyric shergottites LAR 06319 and Tissint is supported by variations in oxygen fugacities. LAR 06319 underwent an increase of oxidation state during crystallization (from QFM-2 to QFM-1/+3: Peslier et al. 2010; Balta et al. 2013). Similarly, Tissint experienced oxidation (from QFM-3.6 to QFM -1.35) during cooling, according to experiments and computer modeling (Castle and Herd, 2014). Oxidation was argued to have occurred during degassing: magma can become more oxidized as the dissolved water will dissociate into H_2 and O_2, with the former preferentially exsolved from the magma (Herd et al. 2002).

If we assume that only degassing is involved in creation of Li profiles, The Li concentrations represent the degree of depletion from pyroxene cores to rims in each

shergottite. The amount of degassed fluid can be estimated in the different shergottite parent magmas. We calculated the fraction of water vapor released in open-system Rayleigh distillation, assuming that only degassing with no diffusion, affected Li concentrations and isotopic compositions (Schiavi et al., 2010). For that purpose, we used the highest absolute values for δ^7Li and [Li]. For Shergotty, QUE 94201, and Tissint, the observed fractions of vapor released are 20 ±10 %, 40 ±30 %, and 15 ±5 %, respectively. The range of the amount of vapor released depends on the α and the $^{Li}D_{melt/fluid}$ (using α = 0.966 and 0.978 from Beck et al. 2004, and $^{Li}D_{melt/fluid}$ = 1.5 and 1.1. from Schiavi et al., 2010). The large range in the fraction of vapor released calculated for QUE 94201 is a result of the differing isotopic profiles within each pyroxene. One LAR 06319 pyroxene (px-1) shows a δ^7Li increase from core to rim with a fraction of vapor released of 25±15 %. However, three out of the four pyroxenes show a decrease of δ^7Li, therefore we used α >1 (1.005 and 1.015 from Schiavi et al., 2010). We obtained 25 ±15 % of vapor released, similar to px-1. On average, the fraction of vapor released is similar (~25 %) for the four shergottites, if only degassing processes are considered.

In addition, we investigated the fraction of [Li] depletion from pyroxene cores to rims. The enriched shergottites show ~60 % [Li] depletion, whereas the depleted shergottites show a [Li] depletion of ~25 %, on average. It appears that enriched shergottites underwent more degassing than depleted shergottites, but this pattern could be explained by process other than vapor escape. As mentioned above, some of the δ^7Li profiles cannot be readily explained, such as the W-shape of the Shergotty δ^7Li profiles and the depletion in δ^7Li from cores to rims in LAR 06319 pyroxenes. Beck et al. (2006) showed that Li abundances and isotope ratios do not display a mixing relationship and concluded that the Li systematics of nakhlite meteorites can be attributed to sub-solidus diffusion of Li from the Li-rich groundmass to the pyroxenes. No clear correlation can be identified between Li abundances and δ^7Li for the four shergottites analyzed here, with the possible exception of QUE 94201 (Fig. B8).

Sub-solidus and magmatic diffusion fractionation

Based on calculations using partition coefficients ($^{Li}D_{aq/bas}$ and $^{B}D_{aq/bas}$), Treiman et al. (2006) argued that Li patterns from Lentz et al. (2001) and Beck et al. (2004) cannot be explained by simple aqueous degassing, but alternatively could be due to intracrystalline diffusion. It has been shown that Li diffuses at very fast rates in pyroxene and olivine (e.g., Giletti and Shanahan, 1997; Coogan et al., 2005), and post-crystallization mobilization of Li is also supported by experiments (e.g., Dohmen et al., 2010; Richter et al., 2012; 2014). Because of their relatively large mass difference, ^{7}Li and ^{6}Li should diffuse at different rates in the presence of a [Li] gradient; ^{6}Li preferentially diffuses into minerals 3 % faster than ^{7}Li (Parkinson et al., 2007) and Li diffuses 4-8 % faster in pyroxenes than in olivines (e.g., Jeffcoate et al., 2007; Parkinson et al., 2007; Dohmen et al., 2010). Diffusion can create large isotopic variations of >30‰ within a single pyroxene crystal (e.g., Beck et al., 2006; Richter et al., 2014). The extent of diffusion of minerals in basaltic rocks is difficult to estimate because a number of variables can control diffusion profiles in minerals, including temperature, pressure, oxygen fugacities, crystal orientation, boundary conditions, and activity of Li_4SiO_4 can

control diffusion profiles in minerals (Gallagher and Elliott, 2009; Dohmen et al., 2010; Richter et al., 2014). In both pyroxenes and olivines, fast and slow mechanisms control diffusion involving vacancies in the interstitial site and the octahedral (metal) site, respectively. Diffusion is mostly controlled in nature by diffusion in metal sites (Dohmen et al., 2010; Richter et al., 2014). Lithium diffusion has been described in terrestrial minerals (e.g., Lundstrom et al., 2005; Tang et al., 2007; Jeffcoate et al., 2007; Parkinson et al., 2007; Gallagher and Elliott, 2009) but also in meteorites. Beck et al. (2006) observed Li diffusion in nakhlites from the groundmass to augite. Barrat et al. (2005) also observed post-magmatic diffusion in NWA 479 lunar basalt from groundmass to crystals producing an increase of δ^7Li from cores to rims. Experiments were made to determine a single β, which represents the difference of diffusion rates between the two isotopes $D_7/D_6 = (m_6/m_7)^{\beta}$, of 0.27 (Richter et al., 2014). This value is consistent with Li diffusion observations from Beck et al. (2006), Parkinson et al. (2007), and Jeffcoate et al. (2007).

Gallagher and Elliott (2009) and Richter et al. (2014) observed that Li diffusion is reflected by an increase of [Li] towards pyroxene rims. In clinopyroxene, an asymmetric negative δ^7Li trough close to the boundary, which steps back at zero in the inside of the crystal and migrates towards the center, is observed probably because ^{6}Li diffuses more rapidly than ^{7}Li through the crystals. According to these experiments, the W-shaped δ^7Li profiles in Shergotty, as well as inconsistency in LAR 06319 δ^7Li profiles could be explained by diffusion. The Shergotty pyroxene δ^7Li profiles are similar to the one produced by previous Li diffusion studies (Gallagher and Elliott, 2009; Richter et al., 2014).

No experiments have been conducted on Li concentrations and isotope diffusion at pyroxene/pyroxene interfaces/boundaries and at pyroxene/plagioclase boundaries under sub-solidus conditions. However, as [Li] in maskelynite is enriched compared to the adjacent pyroxene rims, Li concentrations should have diffused inward into pyroxene, which have not been observed. In addition, maskelynite is enriched in ^{6}Li compared to adjacent pyroxene crystals. If diffusion occurred, ^{6}Li, which is the more mobile Li isotope, should diffuse into the pyroxenes, which we have observed in three pyroxenes of LAR 06319.

The δ^7Li enrichment profiles in both QUE 94201 and Tissint pyroxenes could potentially be explained by either degassing or diffusion. However, [Li] profiles in these pyroxenes indicate a degassing process, so we use this explanation for the Li isotopes as well. We do not rule out, however, that sub-solidus diffusion occurred once the shergottite magmas degassed.

In addition to sub-solidus diffusion, diffusion can occur in both minerals and melts during magmatic processes (Lundstrom et al., 2003). It has been concluded that Li can be used as a high-resolution geo-speedometer (Coogan et al., 2005; Jeffcoate et al., 2007). It was observed that Li diffusion is a common process during cooling (e.g., Coogan et al., 2005; Jeffcoate et al., 2007; Parkinson et al., 2007; Rudnick and Ionov, 2007), and that partitioning of Li between plagioclase and pyroxene during cooling is also a function of temperature, with preferential diffusion from plagioclase to pyroxene (Coogan et al., 2005). The degree of diffusion is determined by cooling rate – i.e., at slower cooling rates, the extent of Li diffusion is higher. Shergotty shows a slower

cooling rate than LAR 06319 and Tissint (e.g., Lentz and McSween, 2000; Balta et al., 2013; Udry et al., 2013), which could explain its W-shaped δ^7Li diffusion profiles.

In order to understand the behavior of ^{6}Li and to distinguish diffusion and degassing effects on [Li] and Li isotopes, we isolated the ^{6}Li for each point analyses using the fraction of ^{7}Li (=[Li]) and ^{7}Li/^{6}Li measured to obtain δ^7Li. The ^{6}Li fraction decreases from core to rim in every pyroxene of the four shergottites, indicating the ^{6}Li was mobilized outwards in pyroxene, which is more likely the product of degassing rather than diffusion. Consequently, it appears that water degassing occurred in all the shergottites, with some subsequent lithium diffusion in Shergotty and LAR 06319 pyroxenes.

Enriched versus depleted shergottites

Based on similar Mars ejection ages, Brennecka et al. (2014) suggested that all the depleted shergottites might have come from the same volcanic complex. Therefore, this complex was active from 575 Ma to 325 Ma, and was composed of at least eight distinct lava flows during that interval. Tissint and QUE 94201 represent the oldest and youngest samples we have of this magmatic system. The present study shows that water degassing occurred during the ascent of the oldest and youngest magmas. Thus, other depleted shergottites with intermediate crystallization ages should also be expected to exhibit evidences of water degassing of their parental magmas.

In contrast to the depleted shergottites, it is very likely that enriched shergottites did not originate from the same magmatic complex, due to the fact these shergottites do not exhibit similar Mars ejection ages.

Conclusions

In order to investigate water degassing in their parental magmas, we have measured trace-element and LLE-abundance profiles and Li isotope profiles in pyroxenes, olivines, and maskelynites in four compositionally different basaltic and olivine-phyric shergottites.

- Most trace-element profiles are consistent with crystallization from a fractionating magma. However, LLE profiles suggest open system behavior. Additionally, mineral zoning in these shergottites was not disturbed by alteration or shock processes.

- Lithium and B, which are both soluble in H_2O-rich fluids, are depleted in pyroxene rims and are negatively correlated with Fe#. Beryllium, which is insoluble in water-rich liquid, shows a normal igneous fractionation trend in pyroxenes. These results likely indicate escape of Li and B in an exsolved aqueous phase and, thus water degassing in all four shergottite parental magmas.

- Unlike pyroxenes, [Li] profiles in olivines of olivine-phyric shergottites show a normal igneous fractionation trend. This indicates that olivine megacrysts probably crystallized before pyroxene rims and before degassing.

- Li isotope profiles in pyroxenes of QUE 94201 and Tissint show δ^7Li enrichment from cores to rims, which according to previous studies, is consistent with

water degassing from parental magmas. However, diffusion of ^{7}Li from pyroxene to ilmenite might explain $\delta^{7}Li$ depletion in some QUE 94201 pyroxene rims; W-shaped Li isotope profiles in pyroxenes of Shergotty and LAR 06319 suggest lithium diffusion.

- Degassing appears to have occurred in the parental magmas of all the analyzed shergottites, with an average fraction of vapor degassed of ~25%. Previous oxygen fugacity studies in LAR 06319 and Tissint also suggested magma degassing in the parental magma of these basalts. Degassing of basaltic magmas on Mars might have occurred throughout most of the age range of depleted shergottite formation.

In conclusion, we suggest that the degassing of aqueous fluids from basaltic magmas on Mars may have been the source for a significant amount of surficial water. Although the known shergottites represent only the last half billion years of magmatism on Mars, this study demonstrates the efficiency of magmatic degassing. Older (Noachian and early Hesperian) magmas may have been even wetter, so an analogous process may explain the pervasive geomorphic evidence for surface water in early Mars history.

References

Arvidson et al. (2014) Ancient aqueous environments at Endeavour Crater, Mars. *Science* 324:6169.

Basu Sarbadhikari A., Day J. M. D., Liu Y., Rumble III D., and Taylor L. A. 2009. Petrogenesis of olivine-phyric shergottite Larkman Nunatak 06319: Implications for enriched components in martian basalts. *Geochimica et Cosmochimica Acta* 73:2190–2214.

Balta, J. B., Sanborn M., McSween H. Y., and Wadhwa M. 2013. Magmatic history and parental melt composition of olivine-phyric shergottite LAR 06319: Importance of magmatic degassing and olivine antecrysts in martian magmatism, *Meteoritics & Planetary Science* 48:1359-1382.

Barrat J. A., Chaussidon M., Bohn M., Gillet Ph., Gopel C., and Lesourd M. 2005. Lithium behavior during cooling of a dry basalt: An ion-microprobe study of the lunar meteorite Northwest Africa 479 (NWA 479). *Geochimica et Cosmochimica Acta* 69:5597-5609.

Baziotis I. P., Liu Y., DeCarli P. S., Melosh H. J., McSween H. Y., Bodnar R. B., and Taylor L. A. 2013. The Tissint martian meteorite as evidence for the largest impact excavation. *Nature communications* 4:1404.

Beck P., Barrat J.-A., Chaussidon M., Gillet P. H., and Bohn M. 2004. Li isotopic variations in single pyroxenes from the Northwest Africa 480 shergottite (NWA 480): A record of degassing of Martian magmas? *Geochimica et Cosmochimica Acta* 68:2925-2933.

Beck P., Chaussidon M., Barrat J.-A., Gillet Ph., and Bohn M. 2006. Diffusion induced Li isotopic fractionation during the cooling of magmatic rocks: The case of pyroxene phenocrysts from nakhlite meteorites. *Geochimica et Cosmochimica Acta* 70:4813-4825.

Bell D. R., Hervig R. L., Buseck P. R., and Aulbach S. 2009. Lithium isotope analysis of olivine by SIMS: Calibration of a matrix effect and application to magmatic phenocrysts. *Chemical Geology* 258:5-16.

Berlo K., Blundy J., Turner S., Cashman K., Hawkesworth C., and Black S. 2004. Geochemical precursors to volcanic activity at Mount St. Helens, USA. *Science* 306:1167.

Boctor N. Z., Alexander C. M. O'D., Wang J., and Hauri E. 2003. The sources of water in Martian meteorites: Clues from hydrogen isotopes. *Geochimica et Cosmochimica Acta* 67:3971–3989.

Boyce J. W., Tomlinson S. M., McCubbin F. M., Greenwood J. P., and Treiman A. H. 2014. The lunar apatite paradox. *Science* 344:400.

Brenan J. M., Neroda E., Lundstrom C. C., Shaw H. F., Ryerson F. J., and Phinney D. L. 1998. Behaviour of boron, beryllium, and lithium during melting and crystallization: Constraints from mineral melt partitioning experiments. *Geochimica et Cosmochimica Acta* 62:2129–2141.

Brennecka G. A., Borg L. E., and Wadhwa M. (2014) Insights into the martian mantle: The age and isotopics of the meteorite fall Tissint. *Meteoritics & Planetary Sciences* 49:412-416.

Bridges J. C. and Warren P. H. 2006. The SNC meteorites: basaltic igneous processes on Mars. *Journal of the Geological Society* 163:229–251.

Castle C. and Herd C. D. K. 2014. Observational and Experimental Results for Tissint Magma Formation: The Story Thus Far (abstract #2334) 45th Lunar and planetary Science Conference. CD-ROM.

Chaklader, J., Shearer, C.K., Hörz, F., 2005. Li, B—behavior in lunar basalts during shock and thermal metamorphism: implications for H_2O in Martian magmas (abstract #1426) 36th Lunar and Planetary Science Conference

Coogan L. A., Kasemann S. A. and Chakraborty S. 2005. Rates of hydrothermal cooling of new oceanic crust derived from lithium-geospeedometry. *Earth and Planetary Science Letters* 240:415–424.

Dann J. C., Holzheid A. H., Grove T. L., and McSween H. Y. 2001. Phase equilibria of the Shergotty meteorite: Constraints on preeruptive H_2O contents of martian magmas and fractional crystallization under hydrous conditions. *Meteoritics & Planetary Sciences* 36: 793–806.

Davis A. M., Hashimoto A., Clayton R. N., and Mayeda K. 1990. Isotope mass-fractionation during evaporation of Mg_2SiO_4. *Nature* 347:655–658

DePaolo D. J. (1981) Trace-element and isotopic effects of combined wallrock assimilation and fractional crystallization. *Earth and Planetary Science Letters* 53:189–202.

Dohmen R., Kasemann S. A., Coogan L. A. and Chakraborty S. 2010. Diffusion of Li in olivine. Part 1: Experimental observations and a multiple species diffusion model. *Geochimica et Cosmochimica Acta* 74:274–292.

Dreibus G. and Wanke H. 1985. Mars, a volatile-rich planet. *Meteoritics* 20:367-381.

Flesh G. D., Anderson A. R., and Svec H. J. 1973. A secondary isotopic standard for $^7Li/^6Li$ determination. *International Journal of Mass Spectrometry and Ion Physics* 12:265–272.

Gallagher K. and Elliott T. 2009. Fractionation of lithium isotopes in magmatic systems as a natural consequence of cooling. *Earth and Planetary Science Letters* 278:286–296.

Giletti B. J. and Shanahan T. M. 1997. Alkali diffusion in plagioclase feldspar. *Chemical Geology* 139:3-20.

Guild M. R., Bell D. R., Hervig, R. L. 2013. Boron isotopic variation in the subcontinental lithospheric mantle (abstract #2782) American Geophysical Union Fall Meeting.

Herd C. D. K., Treiman A. H., McKay G. A., and Shearer C. K. 2002. Implications of experimental lithium and boron partition coefficients for the petrogenesis of Martian basalts. *Meteoritics & Planetary Sciences* 37:A62.

Herd C. D. K., Treiman A. H., McKay G. A., and Shearer C. K. 2004. The behavior of Li and B during planetary basalt crystallization. *American Mineralogist* 89:832–840.

Herd C. D. K., Treiman A. H., McKay G. A., and Shearer C. K. 2005. Light lithophile elements in martian basalts: Evaluating the evidence for magmatic water degassing. *Geochimica et Cosmochimica Acta* 69:2431–2440.

Jeffcoate A. B., Elliott T., Kasemann S. A., Ionov D., Cooper K. and Brooker R. 2007. Li isotope fractionation in peridotites and mafic melts. *Geochimica et Cosmochimica Acta* 71:202–218.

Jochum K. P., Weis U., Stoll B., Kuzmin D., Yang Q., Raczek I., Jacob D. E., Stracke A., Birbaum K., Frick D. A., Gunther D., and Enzweiler J. 2011 Determination of Reference Values for NIST SRM 610—617 Glasses Following ISO Guidelines. *Geostandards and Geoanalytical Research* 35:397-429.

Karlsson H. R., Clayton R. N., Gibson E. K., and Mayeda T. K. 1992. Water in SNC meteorites: Evidence for a martian hydrosphere. *Science* 255:1409-1411.

Kassemann S. A., Jeffcoate A. B., and Elliott T. 2005. Lithium isotope composition of basalt glass reference material. *Analytical Chemistry* 77:5251-5257

Lentz R. C. F. and McSween H. Y. 2000. Crystallization of the basaltic shergottites: Insights from crystal size distribution (CSD) analysis of pyroxenes. *Meteoritics & Planetary Sciences* 35: 919-927.

Lentz R. C. F., McSween H. Y., Ryan J., and Riciputti L. R. 2001. Water in martian magmas: Clues from light lithophile elements in shergottite and nakhlite pyroxenes. *Geochimica et Cosmochimica Acta* 65: 4551–4565.

Lundstrom C. C., Chaussidon M. Hsui A. T., Kelemen P., and Zimmerman M. 2005. Observations of Li isotopic variations in the Trinity Ophiolite: Evidence for isotopic fractionation by diffusion during mantle melting. *Geochimica et Cosmochimica Acta* 69:735–751

McCubbin, F. M., E. H. Hauri, S. M. Elardo, K. E. Vander Kaaden, J. Wang, and C. K. Shearer, Jr. 2012. Hydrous melting of the martian mantle produced both depleted and enriched shergottites. *Geology* 40:683-686.

McSween H. Y. and Harvey R. P. 1993. Outgassed water on Mars: Constraints from melt inclusions in SNC meteorites. *Science* 26:1890-1892.

McSween, H. Y., Eisenhour D. D., Taylor L. A., Wadhwa M., and Crozaz G. 1996. QUE94201 shergottite: crystallization of a Martian basaltic magma. *Geochimica et Cosmochimica Acta* 60, 4563–9.

McSween H. Y., Grove T. L., Lentz R. C. F., Dann J. C., Holzheid A. H., Riciputi L. R., and Ryan J. G. 2001. Geochemical evidence for magmatic water within Mars from pyroxenes in the Shergotty meteorite. *Science* 409:487-489.

Parkinson I. J., Hammond S. J., James R. H. and Rogers N. W. 2007. High-temperature lithium isotope fractionation: Insights from lithium isotope diffusion in magmatic systems. *Earth and Planetary Science Letters* 257:609–621.

Peslier A. H., Hnatyshin D., Herd C. D. K., Walton E. L., and Brandon A. D. 2010. Crystallization, melt inclusion, and redox history of a Martian meteorite: Olivine-

phyric shergottite Larkman Nunatak 06319. *Geochimica et Cosmochimica Acta* 74:4543–4576.

Richter F., Watson B., Chaussidon M., Mendybaev R., and Ruscitto D. 2014. Lithium isotope fractionation by diffusion in minerals. Part 1: Pyroxenes. Geochimica et Cosmochimica Acta 126: 352–370.

Schiavi F., Kobayashi K., Morigu T., Nakamura E., Pompilio M., Tiepolo M., and Vannucci R. 2010 Degassing, crystallization and eruption dynamics at Stromboli: trace element and lithium isotopic evidence from 2003 ashes. *Contributions to Mineralogy and Petrology* 159:541–561

Seitz H.-M., Brey G. P., Weyer S., Durali S., Ott U., Münker C., and Mezger K. 2006. Lithium isotope compositions of Martian and lunar reservoirs. *Earth and Planetary Science Letters* 245:6–18.

Stöffler D., Ostertag R., Jammes C., Pfannschmidt G., Sen Gupta P. R., Simon S. B., Papike J. J., and Beauchamp R. H. 1986. Shock metamorphism and petrology of the Shergotty achondrite. *Geochimica et Cosmochimica Acta* 50:889–903.

Stolper E. and McSween H. Y. 1979. Petrology and origin of the shergottite meteorites. *Geochimica et Cosmochimica Acta* 43:1475-1498.

Tang Y.-L., Zhang H.-F., and Ying J.-F. 2007. Review of the Lithium Isotope System as a Geochemical Tracer. *International Geology Review*. 49:374-388.

Tomascak P. B. 2004. Development sin the understanding and application of lithium isotopes in earth and planetary sciences. *Reviews in Mineralogy and Geochemistry* 55:153–195.

Treiman A. H. 1985. Amphibole and hercynite spinel in Shergotty and Zagami: magmatic water, depth of crystallization, and metasomatism. *Meteoritics* 20:229-243.

Treiman A. H., Musselwhite D. S., Herd C. D. K., and Shearer C. K. Jr. 2006. Light lithophile elements in pyroxenes of Northwest Africa (NWA) 817 and other Martian meteorites: Implications for water in Martian magmas. *Geochimica et Cosmochimica Acta* 70:2919–2934.

Udry A., Balta J. B., and McSween H. Y. 2013. CSD measurements on olivine grains in the Tissint meteorite (abstract #1266). 44th Lunar and Planetary Science Conference. CD-ROM

Usui T., McSween H. Y., and Floss C. 2008. Petrogenesis of olivine-phyric shergottite Yamato 980459, revisited, *Geochimica et Cosmochimica Acta.* 72:1711-1730.

Usui T., Alexander C. M. O'D, Wang J., Simon J. I., and Jones J. H. 2012. Origin of water and mantle–crust interactions on Mars inferred from hydrogen isotopes and volatile element abundances of olivine-hosted melt inclusions of primitive shergottite. *Earth and Planetary Science Letters* 357–358:119–129.

Williams R. M. E. et al. 2013 Martian Fluvial Conglomerates at Gale Crater. *Science* 340:1068.

Wilson L. and Head, J. W. 1981 Ascent and eruption of basaltic magma on the Earth and Moon. *Journal of Geophysical* Research 86:2971-3001.

Appendix B

Table B1. Major- and trace-element analyses and Li isotopic compositions of pyroxenes in shergottites.

#	En	Wo	Fs	Fe#	Ti (ppm)	Sr (ppm)	Y (ppm)	Zr (ppm)	Ce (ppm)	Li (ppm)	B (ppm)	Be (ppm)	δ7Li (± 2 σ) (‰)
Shergotty													
Px-1													
1	12	21	67	0.85	2585	0.51	2.57	6.95	n.d.	1.40	2.10	0.019	1.3 ± 1.4
2	25	31	44	0.64	2463	2.33	9.19	9.22	0.51	2.60	n.d.	0.010	4.6 ± 1.2
3	34	35	31	0.48	1216	2.67	4.43	6.43	0.29	3.77	n.d.	n.d.	2.9 ± 1.1
4	36	35	29	0.45	955	3.62	3.88	3.90	0.18	3.74	n.d.	n.d.	2.3 ±1.1
5	23	12	65	0.74	1843	0.63	3.55	5.36	0.11	1.97	3.42	0.035	4.3 ± 1.5
Px-2													
1	27	13	60	0.69	1171	1.10	2.55	7.25	0.54	2.36	3.57	0.025	2.3 ± 1.1
2	46	14	39	0.46	811	0.48	1.27	4.76	0.04	2.70	n.d.	n.d.	-0.3 ± 0.6
3	47	13	40	0.46	980	0.55	1.90	5.43	0.07	2.83	n.d.	n.d.	-1.2 ± 1.3
4	36	36	28	0.43	941	1.61	2.54	4.29	0.20	5.85	n.d.	n.d.	3.3 ± 0.8
5	28	31	41	0.60	1045	1.78	2.58	4.00	0.19	4.54	n.d.	n.d.	-2.2 ± 0.8
6	13	22	65	0.84	n.d.	n.d.	n.d.	n.d.	n.d.	n.d.	n.d.	n.d.	1.5 ± 1.5
Px-3													
1	23	27	50	0.69	0.47	4.32	9.15	15.3	1.31	2.46	3.93	0.040	6.2 ± 1.1
2	47	15	38	0.44	0.11	0.83	0.82	n.d.	0.04	3.61	n.d.	n.d.	5.5 ± 0.8
3	44	11	45	0.50	0.14	0.72	1.03	3.40	0.09	2.42	n.d.	n.d.	8.7 ± 0.8
4	28	13	59	0.68	0.28	1.02	3.47	6.81	0.14	1.97	3.44	0.027	2.7 ± 1.3
5	19	14	67	0.78	0.54	1.31	4.61	8.50	0.21	1.71	3.04	0.044	1.7 ± 1.8
6	16	14	70	0.81	0.50	1.32	4.61	7.92	0.19	1.14	2.09	0.021	2.2 ± 1.4
QUE 94201													
Px-1													
1	7	11	82	0.92	3934	0.85	3.02	16.9	0.01	0.51	0.08	0.010	6.7 ± 5.3
2	25	29	46	0.64	4265	1.51	10.36	6.74	0.06	1.08	0.19	n.d.	22.1 ± 1.8
3	34	37	29	0.46	3395	1.90	12.01	6.22	0.08	1.49	0.20	n.d.	-0.4 ± 2.6
4	46	11	42	0.48	2026	0.46	4.78	2.24	0.03	1.25	0.47	n.d.	3.3 ± 2.7
5	35	34	30	0.46	3033	1.66	10.54	5.15	0.08	1.16	0.66	0.002	-2.6 ± 2.7
6	30	33	37	0.56	3897	1.79	12.76	0.38	0.03	1.34	0.46	n.d.	16.3 ± 2.6
Px-2													
1	14	15	71	0.84	4213	0.64	3.26	4.96	0.06	0.43	0.16	n.d.	45.6 ± 1.6
2	23	21	56	0.71	4444	1.35	9.60	2.15	0.03	1.06	0.40	n.d.	13.3 ± 6.3
3	38	13	49	0.56	2525	0.39	4.85	7.47	0.03	1.32	0.41	n.d.	2.2 ± 2.9
4	32	41	27	0.46	3555	1.91	12.6	2.42	0.10	1.47	0.62	n.d.	5.8 ± 2.4
5	37	13	49	0.57	2585	0.35	5.00	0.00	0.02	1.21	0.29	n.d.	6.5 ± 3.3
6	19	12	68	0.78	4115	0.56	7.34	4.27	0.04	1.01	0.18	n.d.	26.5 ± 3.5
Px-3													
1	39	26	35	0.47	4227	1.82	3.33	38.5	0.02	0.92	0.72	0.074	-6.0 ± 2.3
2	44	17	40	0.48	3307	1.60	11.7	6.98	0.08	1.15	n.d.	n.d.	0.9 ± 3.6
3	46	12	42	0.48	3485	2.16	10.3	6.72	0.14	1.59	n.d.	n.d.	-1.0 ± 3.3
4	32	22	46	0.59	2542	0.49	5.91	3.45	0.03	0.92	n.d.	n.d.	n.d.
5	18	13	69	0.79	4387	0.62	7.14	4.56	0.04	0.90	n.d.	n.d.	16.9 ± 3.5
Px-4													
1	18	13	69	0.79	4447	0.62	4.85	5.51	0.01	1.00	n.d.	n.d.	15.8 ± 1.3
2	27	33	40	0.60	n.d.	n.d.	n.d.	n.d.	n.d.	n.d.	n.d.	n.d.	-4.7 ± 0.9
3	35	35	30	0.46	3439	3.32	13.1	7.10	0.11	1.06	n.d.	n.d.	-7.3 ± 1.6
4	44	14	42	0.48	2182	1.10	6.81	3.10	0.04	0.84	n.d.	n.d.	-4.1 ± 1.5
5	22	16	61	0.73	3939	1.38	8.54	4.92	0.03	0.87	n.d.	n.d.	6.7 ± 1.3
6	15	11	75	0.84	2621	0.54	2.27	2.91	0.01	0.70	n.d.	n.d.	9.0 ± 1.8

Table B1. (Continued)

#	En	Wo	Fs	Fe#	Ti (ppm)	Sr (ppm)	Y (ppm)	Zr (ppm)	Ce (ppm)	Li (ppm)	B (ppm)	Be (ppm)	δ7Li (± 2 σ) (‰)
LAR 06319													
Px-1													
1	10	5	85	0.46	1679	4.59	5.67	9.54	0.31	2.13	2.13	0.08	1.5 ± 1.2
2	15	13	72	0.39	284	0.19	0.36	1.24	0.03	4.08	n.d.	n.d.	-9.2 ± 3.2
3	15	15	70	0.39	370	0.24	0.50	1.61	0.06	4.14	n.d.	0.01	0.6 ± 2.5
4	13	10	77	0.43	1041	1.24	1.11	3.69	0.11	3.02	0.90	0.02	n.d.
5	14	2	85	0.65	2722	1.34	5.86	10.2	0.20	1.05	2.73	0.10	6.7 ± 2.9
Px-2													
1	12	9	79	0.44	1156	1.09	2.43	2.71	0.16	2.59	0.78	0.02	-3.2 ± 2.4
2	16	14	69	0.40	700	0.19	0.62	0.69	0.03	2.90	0.25	0.02	-3.7 ± 2.5
3	13	11	76	0.41	745	0.16	0.71	1.22	0.02	2.66	0.26	0.03	-4.9 ± 2.9
4	11	3	85	0.51	2507	2.61	7.15	18.5	0.57	2.58	0.84	0.11	5.5 ± 1.8
5	9	0	90	0.69	n.d.	0.97	6.43	18.1	2.08	0.74	1.23	0.28	-8.0 ± 3.6
Px-3													
1	16	13	71	0.41	831	0.52	1.87	3.92	0.06	2.28	1.76	0.04	11.9 ± 1.9
2	16	14	70	0.40	924	0.68	2.13	5.65	0.08	2.43	1.74	0.06	11.6 ± 1.7
3	17	16	67	0.40	698	0.26	1.01	3.42	n.d.	2.61	n.d.	n.d.	12.7 ± 2.0
4	9	1	89	0.61	3143	0.90	9.11	9.00	0.21	1.13	1.04	0.12	6.3 ± 2.0
Px-4													
1	11	0	89	0.69	n.d.	n.d.	n.d.	n.d.	n.d.	n.d.	n.d.	n.d.	-5.3 ± 2.2
2	16	12	73	0.43	593	0.58	1.12	1.23	n.d.	2.83	0.26	0.02	1.9 ± 1.0
3	11	2	86	0.65	2613	0.74	7.52	5.75	0.19	1.20	0.24	0.06	1.8 ± 1.7
Tissint													
Px-1													
1	49	14	37	0.43	2044	8.76	6.22	3.34	n.d.	1.19	n.d.	0.25	2.5 ± 1.6
2	57	5	38	0.40	1272	1.44	3.05	2.18	0.07	1.32	0.25	0.11	0.8 ± 1.3
3	50	12	38	0.43	643	0.30	1.15	0.40	0.00	1.41	0.21	0.05	-4.9 ± 1.3
4	61	4	35	0.37	571	0.50	0.91	0.42	0.00	1.88	0.62	0.07	1.6 ± 1.1
5	36	18	46	0.57	1944	2.64	6.79	4.27	0.08	1.15	1.05	0.16	4.6 ± 1.6
Px-2													
1	36	15	48	0.57	2898	2.28	7.07	5.01	0.23	1.18	0.34	0.09	-2.5 ± 1.8
2	60	5	35	0.37	928	0.84	2.64	0.81	n.d.	1.39	0.39	n.d.	-7.1 ± 1.6
3	60	5	35	0.37	3242	4.08	3.93	4.84	0.14	1.36	n.d.	n.d.	-6.3 ± 1.3
4	50	12	38	0.43	806	0.73	2.26	0.51	n.d.	1.60	n.d.	n.d.	2.2 ± 1.2
Px-3													
1	28	27	45	0.61	n.d.	n.d.	n.d.	n.d.	0.08	n.d.	n.d.	n.d.	4.5 ± 1.5
2	53	9	38	0.42	1045	2.30	2.36	3.29	0.10	1.67	0.36	n.d.	5.1 ± 1.2
3	60	4	35	0.37	2691	2.40	5.16	4.51	0.08	1.51	n.d.	n.d.	2.2 ± 1.7
4	52	10	38	0.42	1169	0.54	2.22	1.45	0.06	1.58	n.d.	n.d.	3.9 ± 1.2
5	38	13	50	0.57	1204	0.53	2.96	0.90	n.d.	1.51	n.d.	n.d.	0.8 ± 1.5
Px-4													
1	40	11	49	0.55	1295	1.20	4.12	1.48	n.d.	1.47	n.d.	n.d.	1.9 ± 1.5
2	60	4	35	0.37	584	0.30	1.06	0.34	n.d.	1.54	n.d.	n.d.	-3.4 ± 1.1
3	42	11	47	0.53	4796	0.82	2.94	2.81	0.06	1.52	n.d.	n.d.	2.7 ± 1.6
4	36	14	50	0.58	1754	0.93	4.60	4.87	0.04	1.15	n.d.	n.d.	2.7 ± 1.6

Table B2. Major- and trace-element analyses of olivines in shergottites.

#	Fe#	Ti (ppm)	Sr (ppm)	Y (ppm)	Zr (ppm)	Ce (ppm)	Li (ppm)	B (ppm)	Be (ppm)
LAR 06319									
Ol-1									
1	59	85.2	0.14	0.21	2.84	0.05	3.40	1.38	0.000
2	55	60.6	0.13	0.28	2.42	0.04	2.05	1.13	0.007
3	47	40.6	0.24	0.34	2.65	0.08	1.88	1.29	0.007
4	42	62.7	0.24	0.25	2.58	0.04	1.41	2.09	0.008
5	41	44.0	0.18	0.22	3.15	0.04	2.16	2.44	0.000
6	58	70.0	0.10	0.15	2.42	0.03	6.46	1.20	0.002
Ol-2									
1	56	92.1	0.10	0.19	2.65	0.04	3.62	1.03	0.003
2	51	55.8	0.12	0.24	1.89	0.05	2.09	1.16	0.003
3	46	76.1	0.25	0.20	2.74	0.02	1.91	2.28	0.004
4	43	39.8	0.29	0.22	3.56	0.03	1.65	2.46	0.007
Ol-3									
1	56	166	0.24	0.19	4.20	0.05	4.09	2.28	0.006
2	55	88.0	0.14	0.25	2.44	0.02	8.53	1.50	0.003
3	42	63.9	0.41	0.27	3.11	0.04	1.71	n.d.	0.009
4	42	68.9	0.20	0.25	3.75	0.04	2.12	2.41	0.013
5	48	45.5	0.18	0.15	3.02	0.03	1.29	n.d.	0.006
6	48	55.0	0.25	0.29	3.33	0.04	2.63	n.d.	0.004
7	50	46.9	0.15	0.18	2.66	0.03	2.88	1.87	0.005
8	53	144	0.47	0.19	3.54	0.13	2.30	n.d.	0.007
Ol-4									
1	55	76.8	0.17	0.17	0.45	0.02	4.71	0.13	n.d.
2	53	54.9	0.21	0.29	0.56	0.01	2.53	n.d.	n.d.
3	53	52.7	0.20	0.16	0.59	n.d.	3.40	0.21	n.d.
4	55	62.1	0.21	0.14	0.72	n.d.	3.10	n.d.	n.d.
Ol-5									
1	63	105	0.17	0.15	1.12	0.01	6.31	n.d.	n.d.
2	58	82.6	0.23	0.17	1.00	0.04	3.42	n.d.	n.d.
3	61	92.7	0.17	0.20	1.23	0.02	6.78	n.d.	n.d.
4	65	116	0.43	0.16	1.35	0.03	4.80	n.d.	n.d.
Ol-6									
1	59	61.8	0.18	0.15	0.76	0.02	4.21	n.d.	n.d.
2	53	81.0	0.15	0.13	0.37	n.d.	4.15	n.d.	n.d.
Tissint									
Ol-1									
1	42	49.4	0.24	0.14	0.21	n.d.	0.78	n.d.	n.d.
2	33	44.4	0.24	0.11	0.20	0.02	0.55	n.d.	n.d.
3	30	46.3	0.19	0.15	0.14	0.02	0.52	n.d.	n.d.
4	29	53.5	0.18	0.13	0.22	n.d.	0.50	n.d.	n.d.
5	30	101	0.23	0.14	0.23	n.d.	0.41	n.d.	n.d.
6	31	39.2	0.17	0.12	0.15	0.02	0.54	0.14	0.004
7	42	51.7	0.18	0.10	0.25	0.02	0.60	0.59	0.005
Ol-2									
1	71	73.0	0.26	0.25	0.33	0.04	1.23	n.d.	n.d.
2	42	67.3	0.32	0.20	n.d.	0.02	0.78	n.d.	n.d.
3	37	85.7	0.27	0.19	0.29	n.d.	0.72	n.d.	n.d.
Ol-3									
1	59	82.1	0.37	0.26	0.55	0.02	1.56	n.d.	n.d.
2	31	46.4	0.29	0.15	0.36	0.03	0.50	n.d.	n.d.
3	31	39.8	0.32	0.13	0.28	n.d.	0.58	n.d.	n.d.
4	32	42.4	0.29	0.15	0.38	0.03	0.52	n.d.	n.d.
5	33	43.2	0.31	0.16	0.74	0.02	0.54	n.d.	n.d.
6	40	52.5	0.30	0.16	0.35	0.03	0.66	n.d.	n.d.
7	44	56.2	0.33	0.16	0.35	0.03	0.66	n.d.	n.d.
8	58	69.9	0.29	0.23	0.31	0.02	1.00	n.d.	n.d.
Ol-4									
1	56	115	0.54	0.26	0.63	0.03	1.11	n.d.	n.d.
2	34	72.7	0.50	0.19	0.49	n.d.	0.81	n.d.	n.d.
3	32	41.7	0.41	0.14	0.53	n.d.	0.65	n.d.	n.d.
4	31	42.4	0.31	0.13	0.40	0.02	0.56	n.d.	n.d.
5	31	46.9	0.30	0.15	0.46	n.d.	0.50	n.d.	n.d.
6	33	55.7	0.37	0.15	0.52	n.d.	0.53	n.d.	n.d.
7	43	51.1	0.28	0.16	0.34	n.d.	0.52	n.d.	n.d.
8	55	72.8	0.29	0.24	0.27	n.d.	1.25	n.d.	n.d.
Ol-5									
1	66	85.2	0.36	0.26	0.22	0.03	1.23	n.d.	n.d.
2	49	72.8	0.33	0.15	0.30	0.02	1.15	n.d.	n.d.
3	44	43.6	0.27	0.11	0.22	n.d.	0.67	n.d.	n.d.
4	57	77.9	0.31	0.23	0.61	n.d.	1.12	n.d.	n.d.
Ol-6									
1	60	62.9	0.24	0.18	0.21	n.d.	0.98	n.d.	n.d.
2	46	62.4	0.29	0.16	0.20	n.d.	0.78	n.d.	n.d.
3	58	113	0.41	0.45	0.53	n.d.	2.80	n.d.	n.d.

Table B3. Major- and trace-element analyses of maskelynite in shergottites.

#	An	Ti (ppm)	Sr (ppm)	Y (ppm)	Zr (ppm)	Ce (ppm)	Li (ppm)	B (ppm)	Be (ppm)	δ7Li (± 2 σ) (‰)
Shergotty										
Mask-1										
1	58	254	201	0.03	1.38	0.09	4.83	0.45	0.659	-4.3 ± 1.1
2	67	205	140	n. d.	1.25	0.20	4.06	0.24	0.218	-3.6 ± 1.0
Mask-2										
1		1779	68.7	0.51	443	0.17	0.94	27.7	1.113	-5.6 ± 1.9
2	n.d.	1599	60.8	0.49	433	0.23	0.92	27.9	1.044	-2.5 ± 1.9
Mask-3										
1	67	1697	44.5	0.43	630	0.14	1.31	22.7	1.063	-1.4 ± 1.6
2	67	171	124	0.05	1.59	0.16	3.61	0.27	0.177	-1.8 ± 1.0
QUE 94201										
Mask-1										
1	71	348	84.3	0.11	0.42	0.03	4.58	0.07	0.047	-2.2 ± 2.4
2	72	294	79.8	n. d.	0.69	0.03	4.65	0.07	0.039	-5.8 ± 1.4
3	72	300	81.2	0.09	9.24	0.02	4.56	0.12	0.043	-5.3 ± 1.6
Mask-3										
1	71	313	50.8	0.11	0.74	0.02	5.39	0.14	0.057	4.4 ± 2.7
2	71	293	47.3	0.10	0.90	0.04	5.30	0.14	n.d.	0.6 ± 2.5
Mask-4										
1	76	265	76.8	0.00	0.52	0.02	3.80	0.36	0.029	-4.7 ± 1.1
2	76	331	77.9	0.11	0.41	0.02	3.94	0.08	0.020	-6.3 ± 0.9
LAR 06319										
Mask-1										
1	65	446	0.35	0.31	0.24	0.12	2.96	5.94	0.385	n.d
2	65	453	0.40	0.02	n. d.	0.01	2.95	10.30	1.345	-6.3 ± 1.4
3	66	478	0.40	0.01	5.58	0.01	3.19	13.52	0.813	n.d.
Tissint										
Mask-1										
1	77	224	105	0.10	n. d.	0.05	1.08	0.08	4.133	-4.3 ± 1.9
2	77	219	101	0.08	0.30	0.07	1.41	0.72	4.198	-6.5 ± 1.9

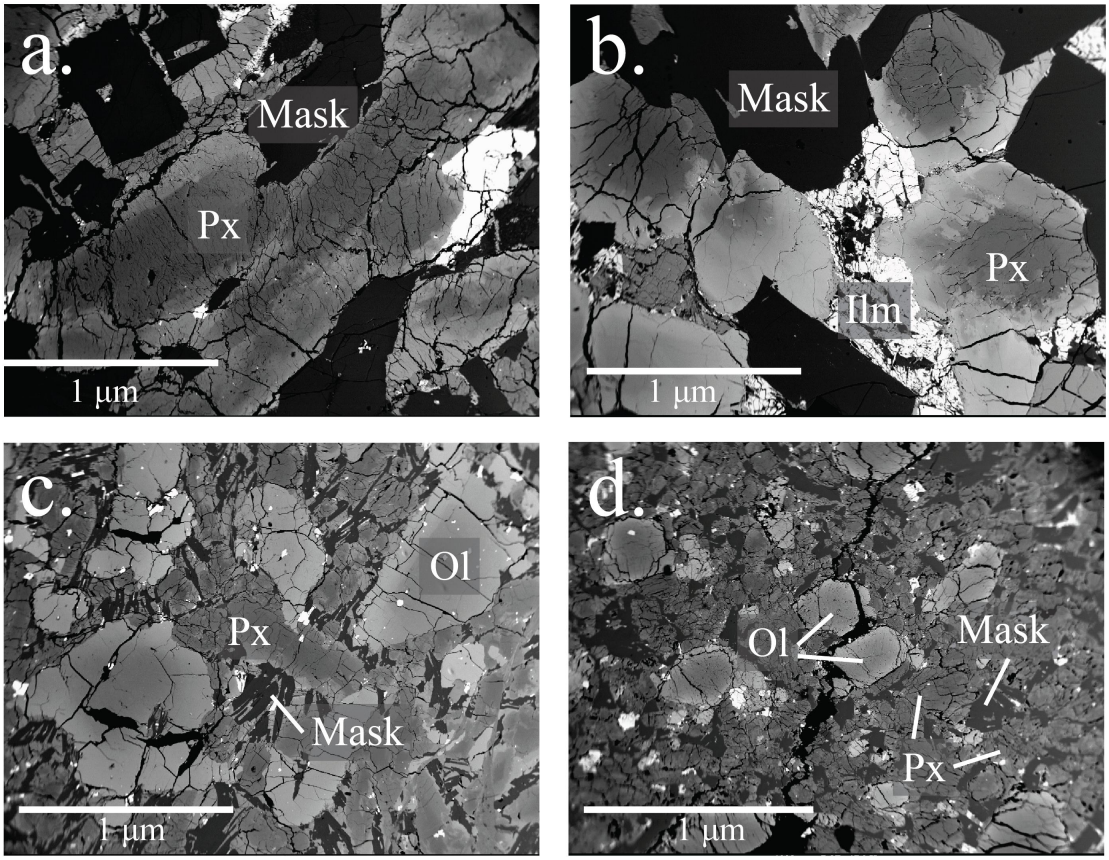

Figure B1. Back-scattered electron images of a) Shergotty, b) QUE 94201, c) LAR 06319, and d) Tissint, showing pyroxene (Px), maskelynite (Mask), olivine (Ol), and ilmenite (Ilm).

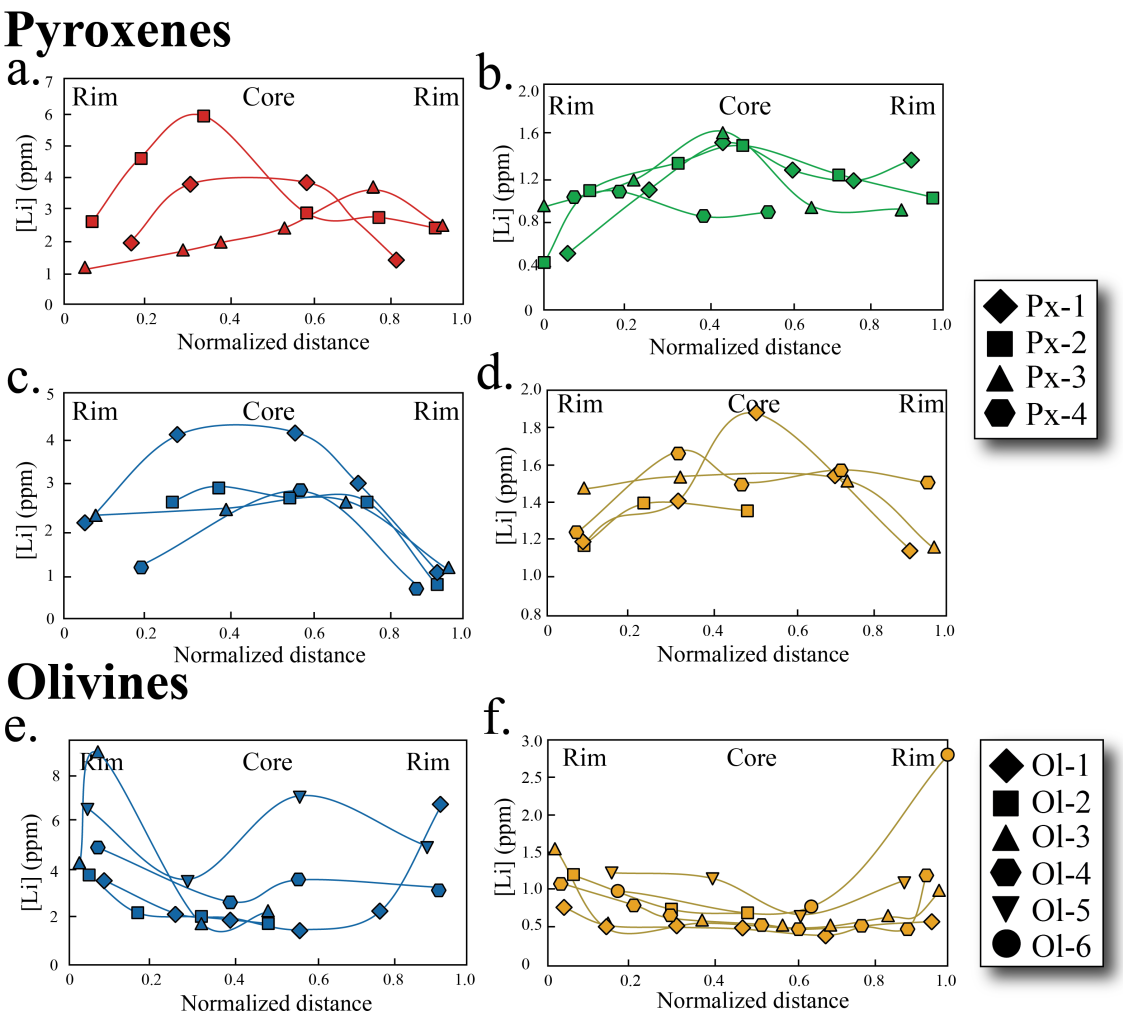

Figure B2. Lithium concentration profiles in pyroxenes and olivines, with distance (mm) normalized by the length of the profiles, in pyroxenes (each traverse was at least 200 µm): a) Shergotty, b) QUE 94201, c) LAR 06319, and d) Tissint, and in olivines e) LAR 06319 and f) Tissint. Each symbol represents a different pyroxene crystal. Lithium concentrations can be seen to decrease from cores to rims of all analyzed shergottites. The relative error (1 %) is smaller than the symbol size.

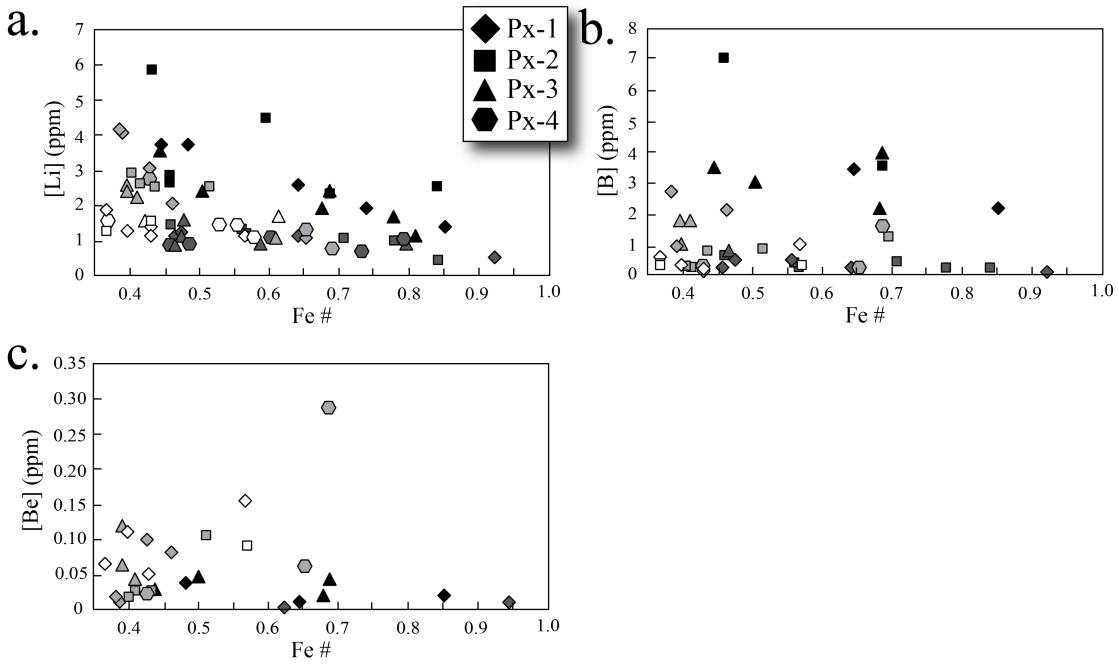

Figure B3. a) Lithium, b) boron, and c) beryllium concentration in pyroxenes versus Fe#. Each symbol represents a different pyroxene for each shergottites. Li and B show distinct decreases with increasing Fe#, and Be shows a slight increase with increasing Fe# for all shergottites. The relative error (1 %) is smaller than the symbol size.

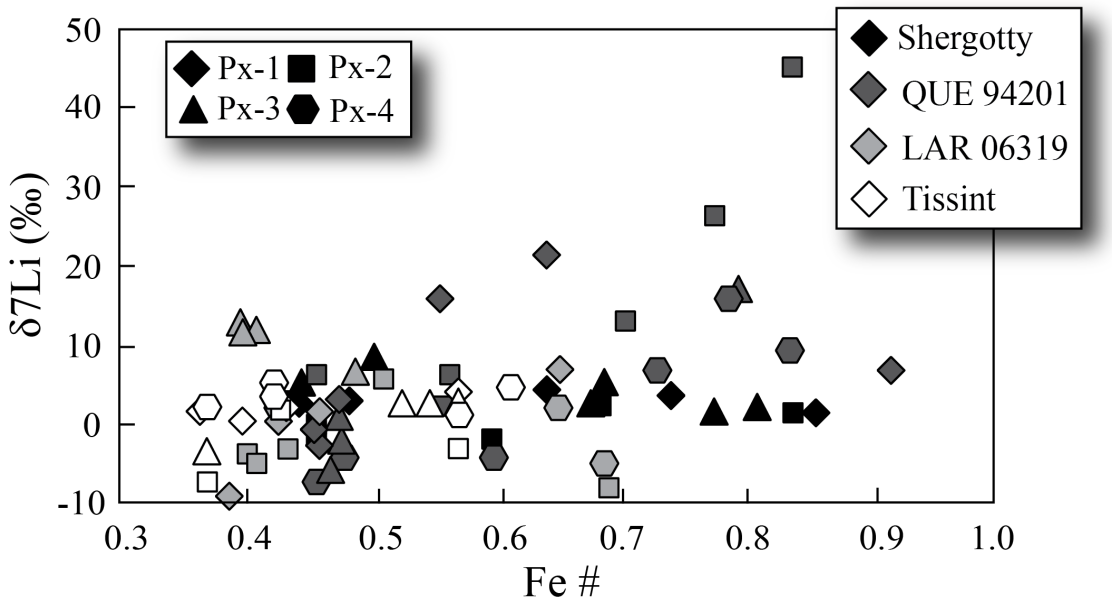

Figure B4. The δ^7Li (‰) profiles in pyroxenes of the four shergottites, with distance (mm) normalized by the length of the profiles (each profile at least 200 μm): a) Shergotty, b) QUE 94201, c) LAR 06319, and d) Tissint. Each symbol represents a different pyroxene. In pyroxenes, δ^7Li increases from cores to rims.

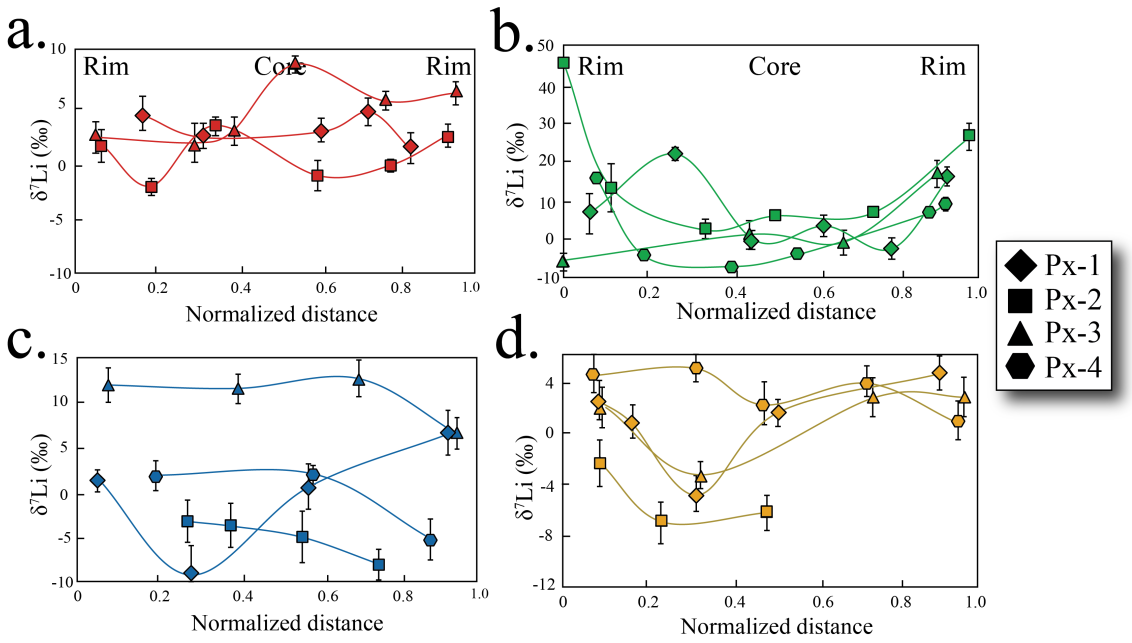

Figure B5. δ^7Li (‰) profiles in pyroxenes, with distance (mm) normalized by the length of the profiles, for a) Shergotty, b) QUE 94201, c) LAR 06319, and d) Tissint. Each symbol represents a different pyroxene. In pyroxenes, δ^7Li increases from cores to rims.

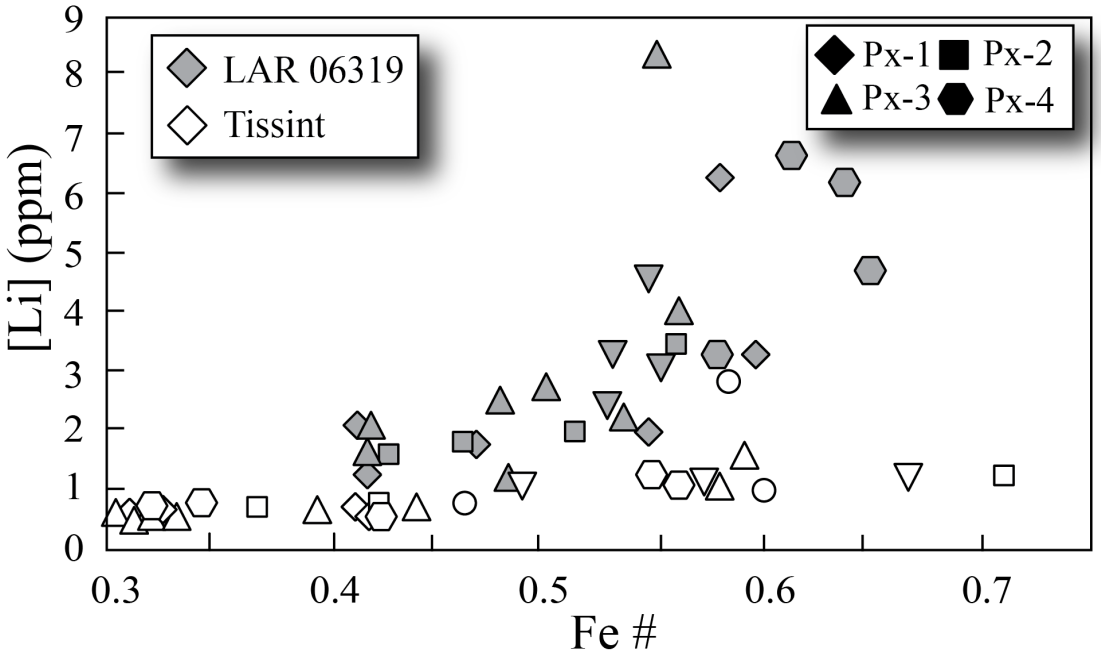

Figure B6. Lithium concentrations (ppm) versus Fe# in olivines in LAR 06319 and Tissint. Lithium concentrations in shergottite olivines are positively correlated with Fe#, indicating a normal igneous fractionation pattern. The relative error (1 %) is smaller than the symbol size.

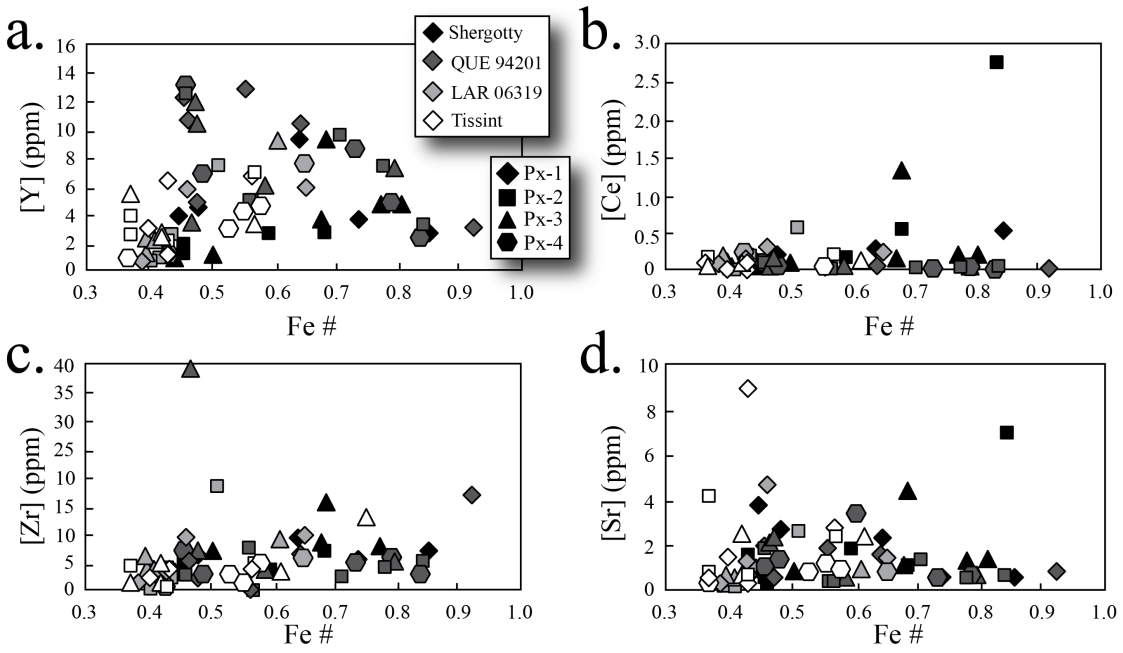

Figure B7. a) Yttrium, b) cerium, c) zirconium, and d) strontium concentrations (ppm) in pyroxenes versus Fe#. Each symbol represents a different pyroxene grain. All these incompatible elements increase with Fe# for all four shergottites.

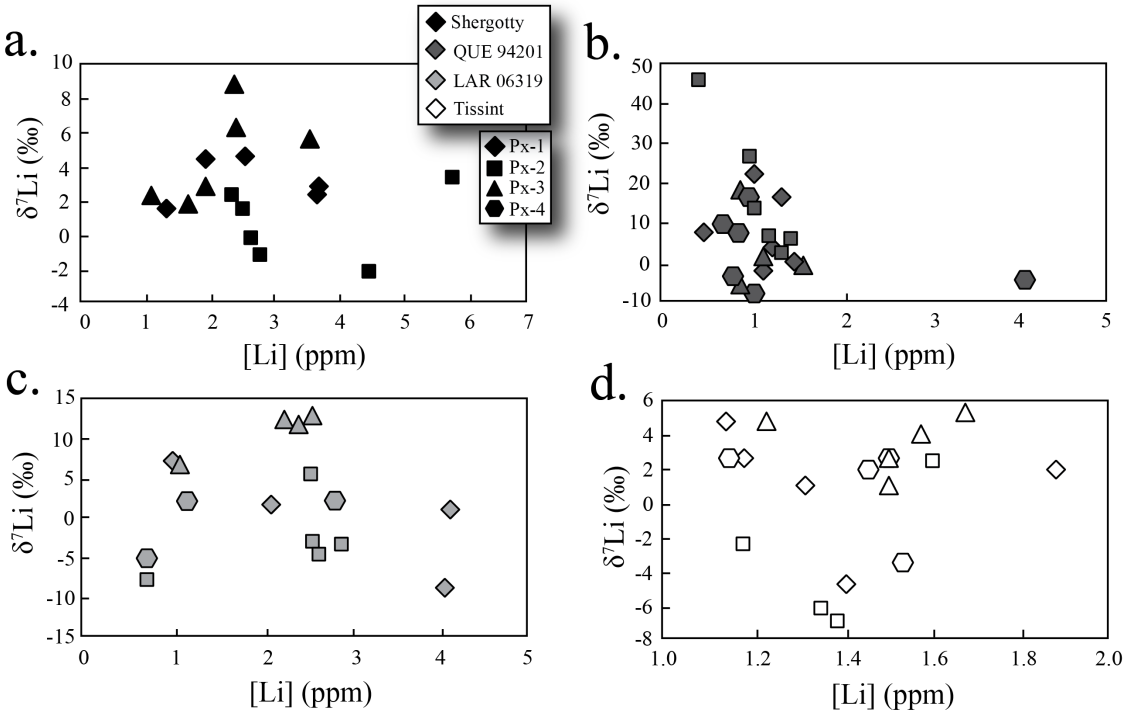

Figure B8. The δ^7Li (‰) versus [Li] (ppm) in pyroxenes for a) Shergotty, b) QUE 94201, c) LAR 06319, and d) Tissint. No clear correlation between δ^7Li (‰) and Li concentrations appear to exist.

CHAPTER III
PAIRED METEORITES MIL 090030, 090032, 090136, AND 03346: INSIGHTS INTO THE MILLER RANGE PARENT METEORITE

This chapter is a reformatted version of a paper of the same name published in Meteoritics and Planetary Science. All the authors wrote this manuscript. Arya Udry collected all the data analyses and was helped by Pilar Leccumberri-Sanchez and Robert Bodnar for LA-ICP-MS data collection.

Udry A., McSween H. Y., Lecumberri-Sanchez P., and Bodnar R. J. 2012. Paired nakhlites MIL 090030, 090032, 090136, and 03346: Insights into the Miller Range parent meteorite. Meteoritics and Planetary Science 47:1575-1589.

Abstract

Miller Range 03346 is the most oxidized and least equilibrated nakhlite known and displays the highest amount of intercumulus phase. The discovery of three new nakhlites, MIL 090030, MIL 090032, and MIL 090136, in the Miller Range, Antarctica, geographically close to the location of MIL 03346, suggests that they may come from the same parent meteorite. In this study, we investigate the mineralogy and texture for cumulus and intercumulus phases, *in situ* major and trace element compositions for the cumulus phases, as well as pyroxene crystal size distribution patterns and spatial distribution patterns of MIL 090030, 090032, and 090136. Using these combined results, we conclude that the three nakhlites studied here are paired with MIL 03346. However, modal mineral abundances of MIL 090030, 090032, 090136, and 03346 exhibit variations indicating that a single sample of a Miller Range nakhlite is not modally representative of the parent meteorite and that analyses of multiple samples for a single nakhlite may be necessary to obtain representative modal data for placement in the pile. Our calculated parental melt composition based on all the paired samples confirms a previous study suggesting that the nakhlite parent melt crystallized as a closed-system.

Introduction

Nakhlites are clinopyroxenites that are thought to derive from Mars (e.g. McSween, 1985; Treiman et al., 2000). At present, a total of eight nakhlites, assuming that the Miller Range nakhlites studied here come from the same parent meteorite, have been recovered. Nakhlites share similar cumulate textures, whole-rock (Light Rare Earth Elements - LREE-enriched) compositions, and mineralogies. Furthermore, they all have a similar cosmogenic exposure age of ~10-11 Ma, indicating a similar ejection time from Mars (Nyquist, 2001), and the same igneous crystallization age of ~1.3 Ga, which has been unambiguously defined by four independent dating techniques: $^{87}Rb/^{87}Sr$, $^{147}Sm/^{144}Nd$, $^{39}Ar/^{40}Ar$, and U/Pb (Nyquist, 2001).

Nakhlites are cumulates consisting of euhedral to subhedral augite and less abundant olivine with a fine-grained intercumulus phase. This intercumulus phase mainly consists of glass, usually with laths of sodic plagioclase (except in MIL 03346; Day et al., 2006), silica, phosphate, pyroxene, and minor opaque phases such as titanomagnetite and

sulfides (e.g. Treiman, 2005). The large pyroxene and olivine grains that dominate nakhlites are interpreted as cumulus phases that crystallized at low pressure in a shallow magma body (Day et al., 2006). Moreover, the presence of cumulus and intercumulus materials indicates a two-stage cooling history. Both pyroxene and olivine are zoned. Augite and olivine cores are relatively magnesium-rich, whereas the rims of both minerals are increasingly ferroan with an average thickness of 10-20μm (Treiman, 2005). The thin rims indicate continuous diffusive exchange with a fractionating magma (McSween and Treiman, 1998).

Because nakhlites all have textural, compositional, and chronologic similarities, it is believed that they all were ejected from a single thick lava flow or sill sequence. Based on their modal abundances and equilibration differences (e.g. thickness of the rims, enrichment in Fe and depletion in Ca in rims), each nakhlite is considered to have originated from a different location in the nakhlite cumulate pile. The model put forth by Treiman (2005), Day et al. (2006), and Mikouchi et al. (2003) suggests that cumulus phases first crystallized at a shallow level from magma derived from a LREE-depleted mantle source. Treiman (2005) and Day et al. (2006) suggested that the LREE-enrichment observed in the whole-rock composition is due to limited partial melting of the mantle source, which probably contains garnet, or to LREE-enrichment prior to segregation of the parental magma. The crystallization of cumulus phases was followed by an entrainment of cumulus phases within the melt and eruption at, or emplacement near, the martian surface. Pyroxene and olivine then settled, and partially equilibrated with the intercumulus phase. Thus, nakhlites that experienced the greatest extent of equilibration are inferred to have been located near the base of the cumulate pile, whereas nakhlites showing less equilibration are assigned to positions nearer the top of the pile. Because stratigraphically lower samples would likely have squeezed out intercumulus melt that would be redistributed upward, the proportion of intercumulus phases, as well as its crystallinity and the phases present in it could also indicate relative position within the pile (e.g. Day et al., 2006; Mikouchi et al., 2003; Mikouchi et al., 2012; Sautter et al., 2003; Jambon et al., 2010).

MIL 03346 was recovered in the Miller Range, Antarctica during the 2003 season. It has been postulated that MIL 03346 was located at or near the top of the cumulate pile because it displays the least extensive equilibration of cumulus minerals, has a high proportion of intercumulus phase (Day et al., 2006), and is the most highly oxidized of the nakhlites (Dyar et al., 2005). Another nakhlite, NWA 5790, displays a higher amount of intercumulus phase; consequently, it was placed at the topmost section of the cumulate pile by Jambon et al. (2010). However, complete results have yet to be published, so this nakhlite will not be considered here. Nakhlites MIL 090030 (452.63 g), MIL 090032 (532.19 g), and MIL 090136 (170.98 g) were collected during the 2009 season in the Miller Range, geographically close to the location of MIL 03346 (Fig. C1). The fact that multiple samples of such a rare meteorite type were found in such geographically close proximity indicates the possibility that the four meteorites may be paired. Using textural, geochemical, and petrographic evidence, we confirm the pairing of MIL 090030, MIL 090032, MIL 090136, and MIL 03346. We also examine the scale

of petrologic variability in the combined, more representative sample, and consider whether modes vary systematically at different levels within the nakhlite cumulate pile.

Methods

One thin section of each nakhlite was analyzed, with surface areas of 58 mm^2 for MIL 090030,21; 101 mm^2 for MIL 090032,21; and 29 mm^2 for MIL 090136,22.

The modal abundances of cumulus pyroxene and olivine as well as intercumulus phase were estimated using pixel counting with *Image J* software. Each cumulus phase grain was drawn in *Adobe Illustrator* and the rest of the thin section was assumed to correspond to the intercumulus phase (Fig. C2). Then, a grey value was assigned for each phase. Using *Image J*, we calculated the proportion of pixels of each grey tone.

In situ major and minor element compositions were determined using the CAMECA SX-100 electron microprobe (EMP) at the University of Tennessee. Operating conditions for the analyses of pyroxene, olivine, chromite, glass, and sulfides were an accelerating voltage of 15 kV, beam currents of 20 nA (pyroxene, glass, chromite, and metals) to 30 nA (olivine), and beam sizes of 2 μm (pyroxene, olivine, and chromite) to 5 μm (glass) using the Wavelength Dispersive (WDS) mode and standard PAP corrections. The counting times for all elements were 20 s, except for Ca (30 s), Cr (30 s) and Ni (50 s) in olivine. The detection limits (3σ above background) were 0.03 wt% for SiO_2, TiO_2, Al_2O_3, Cr_2O_3, MgO, CaO, NiO, P_2O_5, Na_2O and K_2O, and 0.05 wt% for FeO and for Co and Ni in metals. Natural and synthetic standards were used for calibration.

Trace element abundances were measured at Virginia Tech using an Agilent 7500ce inductively coupled plasma mass spectrometer (ICP-MS) combined with an Excimer 193 nm GeoLasPro Laser Ablation (LA) system. We used spot sizes between 16 and 32 μm depending on the grain size. Reference glass NIST SRM610 was used as the external standard. Ca abundances measured with the EMP were used as the internal standard to quantify elemental concentrations using the ratios obtained from the LA-ICP-MS analysis. For each of the analyses, a ~60 s background signal was collected before the ablation process was initiated. The NIST standard was measured two times for 60 s before and after analysis of each sample. Each point-analysis was measured for 40-60 s. The samples were ablated in a He atmosphere. The He gas carrying the ablated particles was then mixed with the make up gas (Ar) before entering the ICP-MS system. The analytical precision for the LA-ICPMS system for the elements analyzed for this study (compared to NIST612) is better than ± 5% (for V, Co, Cr, Ce, Zn, Ga); between ± 5-10% (for Sr, Ba, Pr, Eu, Hf); between ± 10-20% (for Y, Zr, La, Nd, Sm, Gd, Dy, Er, Yb, Lu, Th, Tb, Ho), and poorer than ± 20% for Sc. The detection limits are dependent on several factors such as spot size, element analyzed, and the duration of the analysis. Therefore, each analysis and element has a different detection limit. For all of the trace elements analyzed, the detection limit obtained during our calibration runs described above was less than one ppm. Data reduction was done using the *Analysis Management System* (AMS) software (Mutchler et al., 2008) enabling time-resolved signal analysis.

Petrology and Geochemistry

Petrographic Descriptions

MIL 090030, MIL 090032, and MIL 090136 all display the same mineralogy. They are cumulate clinopyroxenites with minor amounts of olivine set in a vitrophyric intercumulus phase (Fig. C3). Modal abundances for the three nakhlites, listed in the order MIL 090030, MIL 090032, MIL 090136, are as follows: 66.3%, 74.3%, and 64.1% pyroxene, 9.8%, 3.9%, and 9.5% olivine, and 23.9%, 21.9%, and 26.4% intercumulus phase, respectively (also see Table C1).

The pyroxenes are euhedral to subhedral augite prisms, which display Fe-rich rims averaging 10 μm in thickness (Figs C3-4). Their average sizes are 0.38 x 0.23 mm; 0.40 x 0.24 mm, and 0.41 x 0.24 mm for MIL 090030, MIL 090032, and MIL 090136, respectively. Pyroxene lengths can reach 1.8 cm. No Fe-rich rims are present at pyroxene grain boundaries, indicating that the rims formed after pyroxene grains were in contact with each other. They sometimes show single twin planes, a feature probably due to impact shock. Some rare Fe-rich pyroxenes are present in the intercumulus phase. Large patchy melt inclusions (~100 μm), as observed by Sautter et al. (2006) in MIL 03346, were also found in the pyroxenes of MIL 090030/32/136. However, the sizes of the different phases within these melt inclusions were too small to obtain accurate major element compositions with the electron microprobe. No Cl-amphiboles, which were observed in MIL 03346 (Sautter et al., 2006), were detected in this study.

Two types of olivine are distinguished in MIL 090030/32/136: rare, large euhedral to subhedral olivines, which display Fe-rich rims (Fig. C4a), and skeletal fayalites found in the intercumulus phase (Fig. C4c). Unlike the pyroxenes, the large olivines display thick Fe-rich rims that can reach ~100 μm. Olivines enclose rounded pyroxene grains, showing that pyroxene crystallized before olivine. Olivine also displays rounded crystallized melt inclusions ranging up to 100 μm.

The intercumulus phase is mainly composed of incompletely crystallized feldspathic glass containing fine-grained fayalite laths (~5 μm, see Fig. C4c), pyrrhotite, pyroxene, small acicular P-rich phases, and "filaments" (Fig. C4b) composed of aligned sulfide, fayalite, and Fe-Ti-oxides (e.g. Day et al. 2006). P-rich phases are more abundant in MIL 090136 than in the other two nakhlites. The intercumulus phase also displays cruciform (Haggerty, 1976) titanomagnetite with skeletal growth morphologies (Fig. C4a), which has only previously been found in MIL 03346 (Day et al., 2006) and one other nakhlite, NWA 817 (Sautter et al., 2002). These textures are indicative of rapid cooling. No plagioclase was found in the intercumulus phase, unlike in nakhlites farther down in the cumulus pile. The main alteration phase is orange-brown iddingsite, found mainly in veins and cracks within olivine. Iddingsite in Miller Range nakhlites, described by Hallis and Taylor (2011), consists of a mixture of Fe-phyllosilicates and fine-grained Fe-oxides with possible presence of an amorphous silica gel component. Iddingsite forms through low-temperature aqueous alteration of olivine and basalt glass (Treiman, 2005). We did not find other alteration minerals observed by Day et al. (2006) in MIL 03346 and by Hallis and Taylor (2011), who thoroughly described the textures and compositions of secondary minerals in MIL 090030/32/136.

Crystal Size Distribution (CSD) and Spatial Distribution Patterns (SDP) Analyses

Crystal size distribution (CSD) is a useful tool that allows quantification of crystal sizes and an assessment of the growth histories of crystal populations. Magma residence time, which can be useful for understanding nakhlite formation, can be estimated from CSD analyses (Marsh, 1988). CSD is based on steady-state open-system crystallization, during which continuous nucleation and growth result in a negative log-linear plot of population density versus crystal size. The population density n is represented by $n = n_0 \exp(-L/G\tau)$, where n_0 is the final nucleation density, L is the crystal size, G is the growth rate, and τ is the magma residence time (Marsh, 1998).

CSD analyses were applied to pyroxene grains in MIL 090030, MIL 090032, and MIL 090136 (Table C2), using the CSDslice software (Morgan and Jerram, 2006). Pyroxene is the only mineral used in this analysis because it is the most abundant phase crystallizing in nakhlites (Lentz and McSween, 2003). CSDslice converts two-dimensional crystal sizes of random slices through grains by converting them into a true three-dimensional crystal size distribution using a database of 703 discrete crystal shapes. The best matching habit is obtained, representing the short-, intermediate-, and long-axis ratios. The calculated grain shape ratios are 1.0:1.25:1.30; 1.0:1.25:1.40; and 1.0:1.2:1.5 for pyroxenes in MIL 090030/32/136, respectively. Morgan and Jerram (2006) argue that CSD calculations have to be conducted on a minimum of 250 grains per sample in order to establish a statistically significant distribution. 380 pyroxene grains were measured in MIL 090030, 712 grains in MIL 090032, and 153 grains (all that were available) in MIL 090136. Thus, the data for MIL 090136 should be treated with caution. These measured grain size ratios were subsequently entered in CSDcorrection software (Higgins, 2000), which calculates pyroxene population density versus crystal size (Fig. C5; Table C2). The three nakhlites display the same CSD pattern with an overall negative slope and similar intercept. A decrease in population density is observed for the smallest grain sizes. Lentz et al. (1999), who applied CSD measurements to other nakhlites (although without the newer CSDslice software), reported that the turnover at small grain sizes observed for MIL 090030/32/136 reflected the absence of new grains nucleating. MIL 090136 exhibits a discrepancy for small crystal sizes, which can likely be explained by the low number of measured pyroxene crystals in this small thin section.

Residence times of pyroxenes were calculated using the slopes of the CSD plots with the equation: $m = -1/(G\tau)$ (Marsh, 1998). The residence times of all three nakhlites are 54.5± 19.5 Earth years, using the growth rate of 1×10^{-10} mm/s used by Day et al. (2006; Table C2).

Spatial Distribution Pattern (SDP) is a useful tool to determine arrangement of crystals and constrain processes of rock formation. This technique is based on the R-value and the porosity of the thin section (Jerram et al., 1996; 2003). The R-value represents the ratio of the observed versus predicted mean distribution of nearest neighbor distances using the density of the observed distribution. R is defined as $R = (2\sqrt{\rho}\Sigma r) / N$ where ρ is the density of the observed distribution, r the nearest neighbor distance, and N the total number of measured grains (Jerram et al., 1996). Similar to MIL 03346 and other nakhlites (Nakhla, Lafayette, and Governador Valadares), the MIL 090030/32/136 pyroxene population consists of a clustered and touching framework,

comparable to terrestrial phenocrysts in igneous cumulate rocks (Jerram et al., 2003; Fig. C6; Table C2). As mentioned by Day et al. (2006), these phenocrysts form by poor sorting during accumulation in the cumulate pile.

Mineral Major/Minor Element Compositions

Cumulus pyroxene cores are homogeneous and display consistent augite compositions in all three meteorites (Table C3, Fig. C7). The core compositions are magnesian ($Wo_{39-41}En_{35-38}Fs_{22-25}$) and are similar to pyroxene cores in other nakhlites (e.g. Treiman, 2005). They display Fe-rich hedenbergite rims (Fig. C7) with a composition of $Wo_{34-42}En_{6-24}Fs_{37-49}$. As shown in Fig. C7, pyroxene rim wollastonite contents decrease slightly as they become more hedenbergitic in composition. Rims are also enriched in minor incompatible element oxides such as Al_2O_3 and TiO_2, compared to the cores. Fe-rims are only present where they are in contact with the intercumulus phase and do not occur where pyroxenes are in contact with other pyroxenes or with olivine. The pyroxene compositions are indistinguishable among the three meteorites.

The large olivines are zoned, ranging from Fo_{43} in the cores to Fo_{13} in the rims (Table C4, Fig. C7). The olivine cores are similar in composition to those in MIL 03346 and NWA 817 but are slightly more magnesian than in other nakhlites (Day et al., 2006). The intercumulus olivines have fayalitic compositions of Fo_{2-15}. As for pyroxenes, the olivine compositions are similar for all three meteorites. Cumulus phase major element compositions reported here are consistent with the results of Hallis and Taylor (2011).

The intercumulus phase mainly consists of feldpathic glass, with a variable composition from trachy-basalt to trachyte (Fig. C8; Table C5). A pure glass analysis has been difficult to obtain because of the many tiny grains present in the intercumulus phase. Although the range of compositions found in these glasses is similar to those reported by Hallis and Taylor (2011), we do not observe a compositional cluster for MIL 090032 at the extreme right of the MIL 03346 envelope (i.e. MIL 090032 glass is not systematically silica rich). "Filaments", found throughout the intercumulus phase, consist of fayalite, titanomagnetite, and sulfides. Larger intercumulus sulfides than those present in the filaments are pyrrhotites having a composition of $Fe_{0.89-0.92}S$ (Table C5). The compositions of skeletal titanomagnetite are shown in Table C6 and illustrated in Fig. C9. Compared to MIL 03346 (Day et al., 2006), the magnetites display a smaller range of composition from Usp_{33}-Mt_{67} to Usp_{65}-Mt_{35}. Pure magnetite, reported in MIL 03346 (Day et al., 2006), was not found in any of our samples. P-rich needles and Si-rich phases of unresolved mineralogy also occur in the intercumulus phase.

Trace Element Compositions

Pyroxene rims are enriched in incompatible elements such as Y and Ti, and depleted in compatible elements such as Cr (Fig. C10). Pyroxene cores and Fe-rich rims display similar REE patterns, but the rims are enriched in REEs compared to the cores (Fig. C11 and Table C7). The LREEs show a positive slope, whereas a slight negative slope is observed for the heavy REEs (HREEs). The pyroxenes are not enriched in HREEs, contrary to typical terrestrial augites. Small negative Eu anomalies are observed in most pyroxenes. MIL 090030/32/136 REE compositions are similar to the MIL 03346

compositions (Day et al., 2006; Fig. C11). Furthermore, MIL 090030/32/136 REE patterns are parallel to those of other nakhlites (e.g. Wadhwa et al., 2004).

Discussion

Evidence of Pairing

As noted earlier, the geographic proximity of the Antarctic locations where MIL 090030, MIL 090032, MIL 090136, and MIL 03346 were found, was the first indication of pairing. We compared textures, CSD patterns and SDP analyses, *in situ* major and trace element compositions for cumulus phases and mineralogy and major element compositions for intercumulus phases.

Fig. C3 compares plane-polarized light images of the four meteorites at the same scale. All show similar overall textures with equivalent size cumulus pyroxene grains (see also Table C2). Skeletal titanomagnetites have been found in the intercumulus phases of all four meteorites (Fig. C12 a-d). This phase was also observed in NWA 817 (Sautter et al., 2002), but not in other nakhlites. The skeletal texture of the titanomagnetite indicates fast quenching, presumably at or near the top of the cumulate pile.

Pyroxene habits of MIL 090030/32/136 calculated with CSDslice are very similar to that of MIL 03346 calculated by Day et al. (2006). CSD patterns and intercepts for MIL 090030/32/136 and MIL 03346 are similar (Fig. C5). Moreover, the calculated magma average residence time of 54.5±19.5 Earth years (Table C2) is consistent with the residence times of Day et al. (2006) of 20-100 years using the minimum growth rate ($1x10^{-10}$ mm/s) from Jerram et al. (2003). The residence time calculated using the maximum growth rate ($5x10^{-10}$ mm/s) from Jerram et al. (2003), which also corresponds to the growth rate from Leu at al. (2010), is 10.8 ± 5 Earth years, consistent with residence times estimated by Day et al. (2006) (Table C2). The growth rate from Jerram et al. (2003) corresponds to silicate phases in basaltic melt, whereas the growth rate from Leu et al. (2010) is for clinopyroxene in mafic melt. Comparable data obtained using the same technique for different nakhlites are not available in the literature, so comparisons of residence times with nakhlites from deeper levels in the cumulate pile are not possible. However, we should not expect significant differences in pyroxene residence times between the different nakhlites. This is due to the fact that the pyroxenes crystallized at deeper levels in a common magma chamber, before being emplaced at or near the martian surface to form the cumulate pile. Assuming nakhlites all come from the same lava flow sequence (e.g. Day et al., 2006), we would expect to observe the same crystal population, with similar residence times. Thus, pyroxene grain sizes should not vary with depth, except if overgrowths occurred. Furthermore, SDP analyses, which are similar for the Miller Range nakhlites, show that the cumulus phases underwent poor sorting during accumulation in the cumulate pile.

One of the most obvious similarities between MIL 090030/32/136 and MIL 03346 is the pyroxene major element composition. Major and trace element compositions of pyroxene cores and rims in MIL 090030/32/136 plot within the field of MIL 03346 (Figs. C7 and C11). Although cumulus pyroxene cores display the same augitic composition in

all nakhlites, pyroxene rim compositions are different (Fig. C7): NWA 998, which is inferred to have come from the base of the pile (Treiman and Irving, 2008), exhibits pyroxene rims with the highest Mg/Fe, whereas MIL 03346, inferred to be near the top of the pile (Day et al, 2006), is enriched in the wollastonite component. Furthermore, the olivine major element compositions for MIL 090030/32/136 plot within the MIL 03346 field (Fig. C7), as do the glass compositions (Fig. C8) and the Ti-magnetite compositions (Fig. C9). Figure C9 shows the MIL 090030/32/136 data clustered in a narrower compositional range compared to the MIL 03346 envelope, probably due to sampling bias. Trace element compositions of MIL 090030/32/136 pyroxenes are indistinguishable from other nakhlite compositions, except for some REE-enriched rims (e.g. Wadhwa et al., 2004).

Taken together, similar textures and grain sizes, the presence of skeletal titanomagnetite, pyroxene CSD patterns and SDP analyses, cumulus mineral major and trace element compositions as well as intercumulus phase major element compositions, all support pairing of the four meteorites, as also suggested by Hallis and Taylor (2011) and Corrigan et al. (2011). This confirmation of pairing significantly increases the amount of material available for study, so that collectively the four meteorites provide a more representative sampling of this nakhlite.

Nakhlite Modal Abundances

The degree of crystallinity and modal abundance of intercumulus phases, the inferred cooling rate, and the degree of equilibration of cumulus material, are characteristics that could assist with placement of nakhlites within the cumulate pile (e.g. Mikouchi et al. 2003; Mikouchi et al., 2012; Day et al., 2006; Sautter et al., 2002; Jambon et al., 2010). Cumulus phases are expected to be more abundant at the base of the pile whereas the intercumulus phase should be more abundant near the top. This is because of packing of cumulus phases at the base (Mikouchi et al., 2003) as well as quenching near the top, which prevents crystallization of cumulus phases (Sautter at al., 2002). Modal abundances are significantly different for MIL 090030/32/136 and MIL 03346. MIL 090030,21 and 090136,22 contain significantly more olivine than MIL 03346 (see Table C1 and Figs C2 and C13). Moreover, pyroxene content is higher and intercumulus phase is lower in MIL 0990136,21 (Hallis and Taylor, 2011) than in MIL 090136,22 (our thin section). As observed in Fig. C13 and Table C1, modal abundances for pyroxene, olivine and intercumulus phase among the four paired nakhlites in this study vary, as does the intercumulus/cumulus area ratio, indicating that individual Miller Range samples are not modally representative of the entire parent meteorite. Such variations are consistent with studies of terrestrial cumulate piles, in which modal abundances can vary significantly (Lentz et al., 1999). The surface areas of our three nakhlite sections are comparable to nakhlite thin sections reported in the literature (e.g. Day et al. 2006; Imae and Ikeda, 2007; Sautter et al., 2002; Imae et al., 2003; and Lentz et al., 1999) but the modal abundance variations of the nakhlites and intercumulus/cumulus ratio do not show clear trends throughout the cumulate pile (Fig. C13). Thus, we can conclude that modal analyses of multiple samples for a single nakhlite may be necessary to obtain representative modal data. Modal abundances of

pyroxene, olivine, and intercumulus phase for various Miller Range nakhlite samples assumed to come from the same parent sample were used to calculate a weighted mode, taking into account the corresponding areas for each analyzed thin section, to provide a more representative sampling of the parent meteorite (Table C1). A weighted modal abundance was calculated using data from MIL 090030/32/136 from this study, and MIL 03346 data from Day et al. (2006) and Imae and Ikeda (2007). The weighted modal abundance does not include other Miller Range thin sections because not all paper published the areas of the analyzed thin sections. The modal abundance of the parent meteorite is 72.3% pyroxene, 3.9% olivine, and 23.7% intercumulus phase (Table C1). Modal analyses of multiple samples of other nakhlites are required for valid comparisons with MIL nakhlites.

Nakhlite parental melt compositions for MIL 090030/32/136

Nakhlites are cumulate rocks and therefore their compositions are not representative of the parental melt composition. However, it is possible to calculate the parental magma melt composition by inverting REE compositions of the most primitive pyroxene cores using suitable partition coefficients (D-values). The experimental partition coefficients used in this study are the same as those previously employed by Day et al (2006), Wadhwa et al. (2004), and Oe et al. (2001) and were calculated from nakhlite compositions. The fact that MIL 090030/32/136 REE patterns of the calculated parental magma compositions and the measured whole-rock MIL 03346 pattern are parallel (Fig. C14a; Day et al., 2006) supports the conclusion that nakhlites formed by closed-system crystallization of the parental magma (Day et al., 2006; Wadhwa and Crozaz, 1995). Moreover, the average compositions for the intercumulus phases of MIL 090030/32/136 correspond to those of MIL 03346 (Day et al., 2006), confirming closed-system crystallization. These compositions fall on the 30% fractional crystallization line according to the model of Day et al. (2006; Fig. C14b), which is the amount of fractional crystallization necessary to explain the intercumulus phase REE-enriched compositions. The identical intercumulus phase REE patterns for the four MIL nakhlites and the 30% late stage fractional crystallization line support the REE calculations and conclusions of Day et al. (2006). Furthermore, because the REE pyroxene rim composition range is the same for the four Miller Range nakhlites (Day et al., 2006; Fig. C11), 30-100% fractional crystallization is necessary to explain the Fe-rich pyroxene rim compositions.

Conclusions

The MIL 0900030, MIL 090032, and MIL 090136 nakhlites appear to be paired with MIL 03346, as demonstrated by the following:

- similar mineralogy and texture for the cumulus and intercumulus phases
- similar *in situ* major and minor element compositions for the cumulus minerals, glass and Ti-magnetites and trace element compositions for pyroxenes.
- similar CSD patterns and spatial distribution pattern analyses.

However, modal mineral abundances of MIL 090030/32/136 and MIL 03346 show variations indicating that individual Miller Range samples alone are not modally

representative of the parent meteorite. Modal abundances show variations throughout the nakhlite cumulate pile, indicating that analyses of multiple samples of a single nakhlite may be necessary to obtain representative modal data in order to be able to be placed in the nakhlite cumulate pile. Modal analyses of multiple samples of other nakhlites are required for valid comparisons with MIL nakhlites.

Calculated parental melt compositions confirmed closed system fractionation and that a late-stage fractional crystallization of 30% is required to explain REE enrichments of the intercumulus phase.

References

Anders E. and Grevesse N. 1989. Abundances of the elements: Meteoritic and solar. *Geochimica et Cosmochimica Acta* 53:197–214.

Berkley J. L., Keil K., and Prinz M. 1980. Comparative petrology and origin of Governador Valadares and other nakhlites. *Proceedings*, 11th Lunar and Planetary Science Conference. pp.1089–1102.

Corrigan C. M., Vicenzi E. P., Konicek A. R., and Lunning N. 2011. An examination of the new Miller Range nakhlites (MIL 090030, 090032, and 090136) (abstract #2657). 42nd Lunar and Planetary Science Conference. CD-ROM.

Day J. M. D., Taylor L. A., Floss C., and McSween H. Y. 2006. Petrology and chemistry of MIL 03346 and its significance in understanding the petrogenesis of nakhlites on Mars. *Meteoritics & Planetary Science* 41:581–606.

Dyar D., Treiman A. H., Pieters C. M., Hiroi T., Lane M. D., and O'Connor V. 2005. MIL 03346, the most oxidized Martian meteorite: A first look at spectroscope, petrography, and mineral chemistry. *Journal of Geophysical Research* 110: E09005, 2005JE00246.

Haggerty S. E. 1976. Opaque mineral oxides in terrestrial igneous rocks. *Reviews in Mineralogy* 3:101–300.

Hallis L. J. and Taylor G. J. 2011. Comparisons of the four Miller Range nakhlites, MIL 03346, 090030, 090032 and 090136: Textural and compositional observations of primary and secondary mineral assemblages. *Meteoritics & Planetary Science* 46:1787-1803.

Higgins M. D. 2000. Measurement of crystal size distributions. *American Mineralogist* 85:1105–1116.

Imae N. and Ikeda Y. 2007. Petrology of the Miller Range 03346 nakhlite in comparison with the Yamato-000593 nakhlite. *Meteoritics & Planetary Science* 42:171–184.

Imae N., Ikeda Y., Shinoda K., Kojima H., and Iwata N. 2003. Yamato nakhlites: Petrography and mineralogy. *Antarctic Meteorite Research* 16:13–33.

Imae N., Ikeda Y., and Kojima H. 2005. Petrology of the Yamato nakhlites. *Meteoritics & Planetary Science* 40:1581–1598.

Jambon A, Barrat J. A., Bollinger C., Sautter V., Boudouma O., Greenwood R. C., Franchi I., and Badia D. 2010. Northwest Africa 5790. Top sequence of the nakhlite pile (abstract #1696). 41st Lunar and Planetary Science Conference. CD-ROM.

Jerram D. A., Cheadle M. J., Hunter R. H., and Elliot M.T. 1996. The spatial distribution of grains and crystals in rocks. *Contributions to Mineralogy and Petrology* 125:60–74.

Jerram D. A., Cheadle M. J., and Philpotts A. R. 2003. Quantifying the building blocks of igneous rocks: Are clustered crystal frameworks the foundation? *Journal of Petrology* 44:2033–2051.

Lentz R. C. F. and McSween H. Y. 2003. Crystal size distribution analysis of new nakhlites and Los Angeles: How do they compare with SNCs of old? (abstract #1914).

34th Lunar and Planetary Science Conference. CD-ROM.

Lentz R. C. F., Taylor G. J., and Treiman A. H. 1999. Formation of a Martian pyroxenite: A comparative study of the nakhlite meteorites and Theo's flow. *Meteoritics & Planetary Science* 34:919–932.

Leu A.R. 2010 Clinopyroxene growth rate in mafic melts (abstract #33-8). *Geological Society of America* Abstracts with Programs 42(5):100.

Marsh B. D. 1988. Crystal size distribution (CSD) in rocks and the kinetics and dynamics of crystallization, i. Theory. *Contributions to Mineralogy and Petrology* 99:277–291.

Marsh B. D. 1998. On the interpretation of crystal size distributions in magmatic systems. *Journal of Petrology* 39:553–599.

McKay G. and Schwandt C. 2005. Mineralogy and petrology of a new Antarctic meteorite MIL 03346 (abstract #2351). 36th Lunar and Planetary Science Conference. CD-ROM.

McSween H.Y. 1985. SNC meteorites: Clues to Martian petrologic evolution? *Reviews of Geophysics* 23:391–416.

McSween H. Y. and Treiman A. H. 1998. Martian meteorites. In *Planetary materials*, edited by Papike J. J. Washington D. C.: Mineralogical Society of America, pp. 6.1–6.53.

Mikouchi T., Makishima J., Kurihara T., Hoffmann V. H., and Miyamoto M. 2012. Relative burial depth of nakhlites revisited (abstract# 2363). 43rd Lunar and Planetary Science Conference. CD-ROM.

Mikouchi T., Koizumi E., Monkawa A., Ueda Y., and Miyamoto M. 2003. Mineralogy and petrology of Yamato-000593: Comparison with other Martian nakhlite meteorites. *Antarctic Meteorite Research* 16:34–57.

Morgan D. J. and Jerram D. A. 2006. On estimating crystal shape for crystal size distribution analysis. *Journal of Volcanology and Geothermal Research* 154:1–7.

Mutchler S. R., Fedele L., and Bodnar R. J. 2008. Analysis Management System (AMS) for reduction of laser ablation ICPMS data. In *Laser-Ablation-ICPMS in the Earth Sciences: Current Practices and Outstanding Issues*, edited by Sylvester P. Vancouver: Mineralogical Association of Canada Short Course Series, pp. 318-327.

Norman M. D., Pearson N. J., Sharma A., and Griffin W. L. 1996. Quantitative analysis of trace elements in geological materials by Laser Ablation ICPMS: Instrumental operating conditions and calibration values of NIST glasses. *Geostandards Newsletter* 20:247-261.

Nyquist L. E., Bogard D. D., Shih C.-Y., Greshake A., Stöffler D., and Eugster O. 2001. Ages and geologic histories of Martian meteorites. *Chronology and Evolution of Mars* 96:105–164.

Oe K., McKay G., and Le L. 2001. REE and strontium partition coefficients for Nakhla pyroxenes (abstract #2174). 32nd Lunar and Planetary Science Conference. CD-ROM.

Righter K., Yang H., Costin G., and Downs R. T. 2008. Oxygen fugacity in the Martian mantle controlled by carbon: New constraints from the nakhlite MIL 03346. *Meteoritics & Planetary Science* 43:1709–1723.

Sautter V., Barrat J. A., Jambon A., Lorand J. P., Gillet P. H., Javoy M., Joron J. L., and Lesbourd M. 2002. A new Martian meteorite from Morocco: The nakhlite Northwest Africa 817. *Earth and Planetary Science Letters* 195:223–238.

Treiman A. H. 2005. The nakhlite meteorites: Augite-rich igneous rocks from Mars. *Chemie der Erde* 65:203–270.

Treiman A. H. and Irving A. J. 2008. Petrology of the nakhlite (Martian) meteorite Norwthwest Africa (NWA) 998. *Meteoritics & Planetary Science* **43**:829-854.

Treiman A. H., Gleason J. D., and Bogard D. D. 2000. The SNC meteorites are from Mars, *Planetary and Space Sciences* 48:1213 – 1230.

Wadwha M. and Crozaz G. 1995. Trace and minor elements in minerals of nakhlites and Chassigny: Clues to their petrogenesis. *Geochimica et Cosmochimica Acta* 59:3629–3645.

Wadhwa M., Crozaz G., and Barrat J.-A. 2004. Trace element distributions in the Yamato 000593/000749, NWA 817 and NWA 998 nakhlites: Implications for their petrogenesis and mantle source on Mars. *Antarctic Meteorite Research* 17:97-116.

Appendix C

Table C1. Modal abundances of nakhlites. Different modal analyses are represented for MIL 03346.

Sample	Pyroxene	Olivine	Intercumulus matrix
MIL 090030,21	66.3	9.8	23.9
MIL 090032,21	74.3	3.8	21.9
MIL 090136,22	64.1	9.5	26.4
MIL 090030,23[a]	66.4	8.3	22.6
MIL 090032,24[a]	75.0	3.0	21.2
MIL 090136,21[a]	75.2	5.6	18.1
MIL 03346[b]	78.4	1.3	19.8
MIL 03346[c]	67.7	0.8	31.5
MIL 03346[d]	70.8	3.0	26.2
MIL 03346[e]	79.8	4.6	15.7
Weighted modal abundance[f]	72.3	3.9	23.7
NWA 817[g]	69.0	12.5	18.5
Y000593[h]	76.7	12.2	11.1
Nakhla[i]	80.8	10.8	8.4
Gov. Vala.[i]	81.2	8.9	9.8
Lafayette[i]	73.5	16.7	9.8
NWA 998[j]	70.0	10.0	19.0

[a] Hallis and Taylor (2011); [b] Day et al., 2006; [c] Imae and Ikeda, 2007; [d] Dyar et al., 2005; [e] McKay and Schwandt, 2005; [g] Sautter et al., 2002; [h] Imae et al., 2003; [i] Lentz et al., 1999; [j] Treiman, 2005

[f] Weighted modal abundances using MIL 090030/32/136 areas and modal abundances from this study and MIL 03346 values from [b] and [c]

Table C2. Crystal size distribution results for MIL 090030/32/136 and MIL 03346.

Sample	Orientation	Area (mm2)	# grains	Average dimensions (mm)	Slope (mm^{-1})	Intercept	Residence time (10^{-10})[b] (Earth years)	Residence time ($5x10^{-10}$)[c](Earth years)
MIL 090030,21	Length	58	380	0.38	-5.8	6.15	55	11
	Width			0.23	-9.0	7.71	35	7
MIL 090032,21	Length	101	712	0.40	-4.9	5.69	65	13
	Width			0.24	-7.2	7.12	44	9
MIL 090136,22	Length	29	153	0.41	-4.3	5.34	74	15
	Width			0.24	-6.2	6.58	52	10
MIL 03346,111[a]	Length	110	596	0.43	-4.0	5.01	79	16
	Width			0.26	-5.8	6.08	55	11
MIL 03346,118[a]	Length	119	545	0.4	-3.7	4.58	86	17
	Width			0.25	-6.1	5.88	52	10

[a] From Day et al, 2006.

[b] Using growth rate from Jerram et al. (2003)

[c] Using growth rate from Leu (2010)

Table C3. Representative major and minor element compositions of cumulus pyroxenes in MIL 090030/32/136.

wt%	MIL 090030 - Px		MIL 090032 - Px		MIL 090136 - Px	
	Core	Rim	Core	Rim	Core	Rim
SiO_2	51.6	46.0	51.0	47.4	51.1	46.7
TiO_2	0.25	1.01	0.30	0.78	0.32	0.92
Al_2O_3	0.77	3.83	0.85	2.38	0.93	3.10
Cr_2O_3	0.26	<0.03	0.16	-	0.49	<0.03
MgO	12.7	5.30	12.1	5.84	12.8	5.75
CaO	19.7	18.0	19.2	16.8	19.2	17.5
MnO	0.41	0.60	0.44	0.64	0.42	0.61
FeO	14.0	24.4	15.2	25.8	14.2	24.6
Na_2O	0.31	0.39	0.25	0.29	0.28	0.34
Total	100.0	99.6	99.5	100.0	99.7	99.5
Fs	23	43	23	45	23	43
En	37	17	37	18	37	18
Wo	41	41	40	37	40	39

Table C4. Representative major and minor element compositions of cumulus and intercumulus olivines in MIL 090030/32/136.

wt%	Cumulus olivine						Intercumulus fayalite		
	MIL 090030 - Ol		MIL 090032 - Ol		MIL 090136 - Ol		MIL 090030	MIL 090032	MIL 090136
	Core	Rim	Core	Rim	Core	Rim			
SiO_2	33.85	30.78	33.78	30.36	32.61	31.04	30.06	29.99	30.56
Al_2O_3	0.03	0.06	0.03	0.04	0.02	0.03	0.05	0.06	0.03
Cr_2O_3	-	<0.03	<0.03	<0.03	-	0.04	-	-	<0.03
MgO	19.63	8.10	19.11	5.62	16.04	8.04	3.92	2.70	5.96
CaO	0.55	0.44	0.55	0.53	0.54	0.45	0.12	0.21	0.27
MnO	0.94	1.37	0.95	1.47	0.97	1.55	1.92	2.00	1.71
FeO	45.88	59.06	46.40	61.97	49.62	58.51	63.2	64.5	61.6
NiO	<0.05	-	0.05	<0.05	-	-	<0.05	<0.05	-
Total	100.9	99.8	100.9	100.0	99.8	99.7	99.3	99.5	100.2
Fo	43	20	42	14	37	20	10	7	15

Table C5. Representative major and minor element compositions of intercumulus glass and pyrrhotites in MIL 090030/32/136.

wt%	Intercumulus Al-rich glass		
	MIL 090030	MIL 090032	MIL 090136
SiO_2	64.3	60.1	57.0
TiO_2	0.57	0.57	0.34
Al_2O_3	17.8	17.5	18.0
Cr_2O_3	-	-	-
MgO	0.16	0.14	0.58
CaO	3.33	3.30	3.75
MnO	0.05	0.04	0.25
FeO	4.19	10.17	10.90
Na_2O	6.28	6.14	6.32
K_2O	1.69	1.09	1.54
P_2O_5	0.36	0.42	0.85
Total	98.7	99.5	99.6

wt%	Pyrrhotite		
	MIL 090030	MIL 090032	MIL 090136
Si	<0.03	0.03	<0.03
P	-	-	-
S	38.8	38.0	38.6
Fe	61.4	61.5	61.1
Ni	<0.05	<0.05	<0.05
Co	<0.05	0.05	0.05
Total	100.3	99.6	99.8

Table C6. Representative major and minor element compositions of skeletal titanomagnetites in MIL 090030/32/136.

wt%	Titanomagnetite		
	MIL 090030	MIL 090032	MIL 090136
SiO_2	0.22	0.28	0.22
TiO_2	18.2	18.3	19.0
Al_2O_3	2.77	2.30	3.14
V_2O_3	0.30	0.33	0.51
Cr_2O_3	<0.05	<0.05	0.05
Fe_2O_3	28.4	29.6	27.4
FeO	47.0	47.8	48.1
MgO	0.24	0.14	0.34
CaO	0.05	0.06	0.07
MnO	0.57	0.55	0.59
Total	97.8	99.3	99.4
Molar%			
Usp.	53	52	54
Mt.	47	48	46

Table C7. Representative trace element compositions of cumulus pyroxenes in MIL 090030/32/136.

ppm	MIL 090030 - Px		MIL 090032 - Px		MIL 090136 - Px	
	Core	Rim	Core	Rim	Core	Rim
Sc	81.4	97.9	96.4	98.7	85.8	98.6
V	208	460	289	406	228	346
Cr	2984	90.8	1045	68.9	3246	55.0
Co	36.8	45.1	44.6	48.2	39.7	47.9
Zn	48.9	62.6	49.4	65.0	47.3	122.0
Ga	3.69	7.51	2.63	6.85	2.50	10.0
Sr	34.0	33.6	33.2	28.4	32.7	41.0
Y	4.31	10.4	4.65	8.10	3.95	13.7
Zr	2.88	12.2	2.99	10.1	2.53	20.9
Ba	n.d.	n.d.	0.40	0.45	n.d.	1.16
La	0.40	1.37	0.45	0.76	0.53	1.74
Ce	2.17	4.91	2.21	3.63	2.19	7.39
Pr	0.46	1.06	0.42	0.93	0.49	1.38
Nd	2.78	6.61	2.72	4.40	4.25	11.25
Sm	0.86	2.13	0.76	1.42	0.89	1.74
Eu	0.15	0.64	0.25	0.32	0.19	0.78
Gd	0.75	2.57	0.65	1.41	1.09	5.58
Tb	0.31	0.54	0.19	0.38	n.d.	n.d.
Dy	1.12	n.d.	0.96	2.08	0.68	3.05
Ho	0.17	0.46	0.18	0.39	0.23	0.54
Er	0.39	1.55	0.51	1.02	0.43	1.67
Yb	0.53	n.d.	0.47	0.67	0.59	1.84
Lu	n.d.	n.d.	n.d.	n.d.	0.28	n.d.
Hf	n.d.	n.d.	0.18	0.39	n.d.	n.d.
Th	n.d.	n.d.	0.03	n.d.	n.d.	n.d.

n.d. = not detected. In addition, Cu, Rb, Nb, Cs, Tm, Ta, Pb, and U were below detection limit in all pyroxene analyses. Accuracy and precision of analysis is 2-5% relative (Norman et al., 1996).

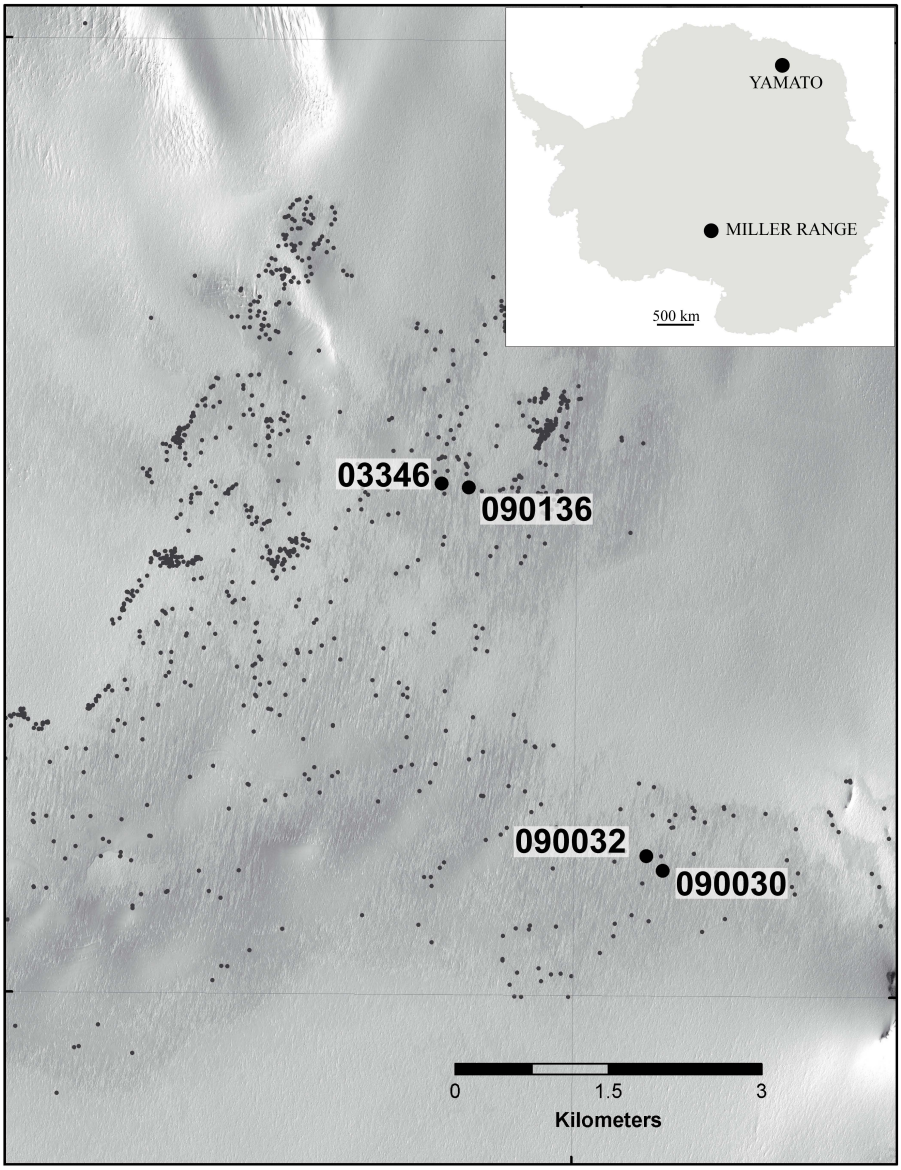

Figure C1. Map of the Miller Range, Antarctica showing the location of MIL 090030, MIL 090032, MIL 090136, and MIL 03346. The meteorites were found in two pairs approximately 4 km apart, and each specimen in the pair was found about 200 m apart. The lines represent undisclosed latitude and longitude and smaller points are other MIL meteorites. Map courtesy of J. Schutt. The inset represents the Antarctica continent showing the Miller Range and Yamato location sites.

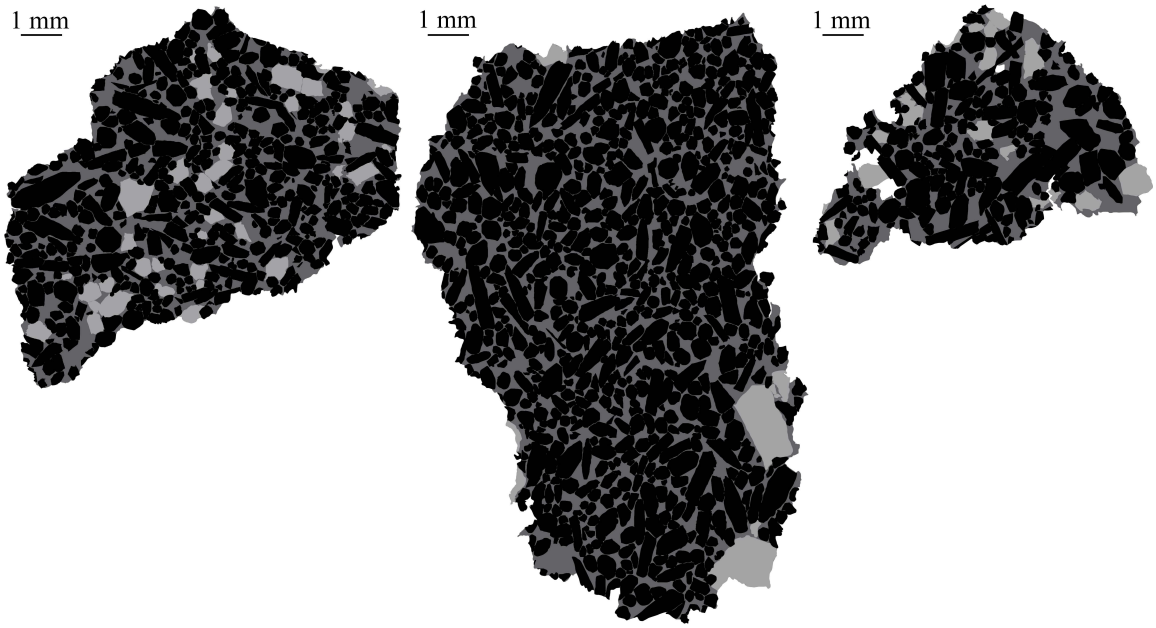

Figure C2. Rendering of the distribution of textures and phases from reflected optical microscopic images in MIL 090030 (a), MIL 090032 (b), and MIL 090136 (c) nakhlites, with pyroxene shown in black, olivine in light grey, and intercumulus phase in dark grey. The three images are at the same scale and were made using *Adobe Illustrat*

Figure C3. Plane polarized photomicrographs (a, b, c, e, and h) and back scattered electron images (b, d, and f) of a) and b): MIL 090030, c) and d): MIL 090032, e) and f): MIL 090136, and g) and h): MIL 03346. The top photographs show whole thin sections all at the same scale. The bottom images, at higher magnification, show cumulus pyroxene and minor olivine with the dark intercumulus phase. Images g) and h) reprinted from Day et al. (2006) with permission.

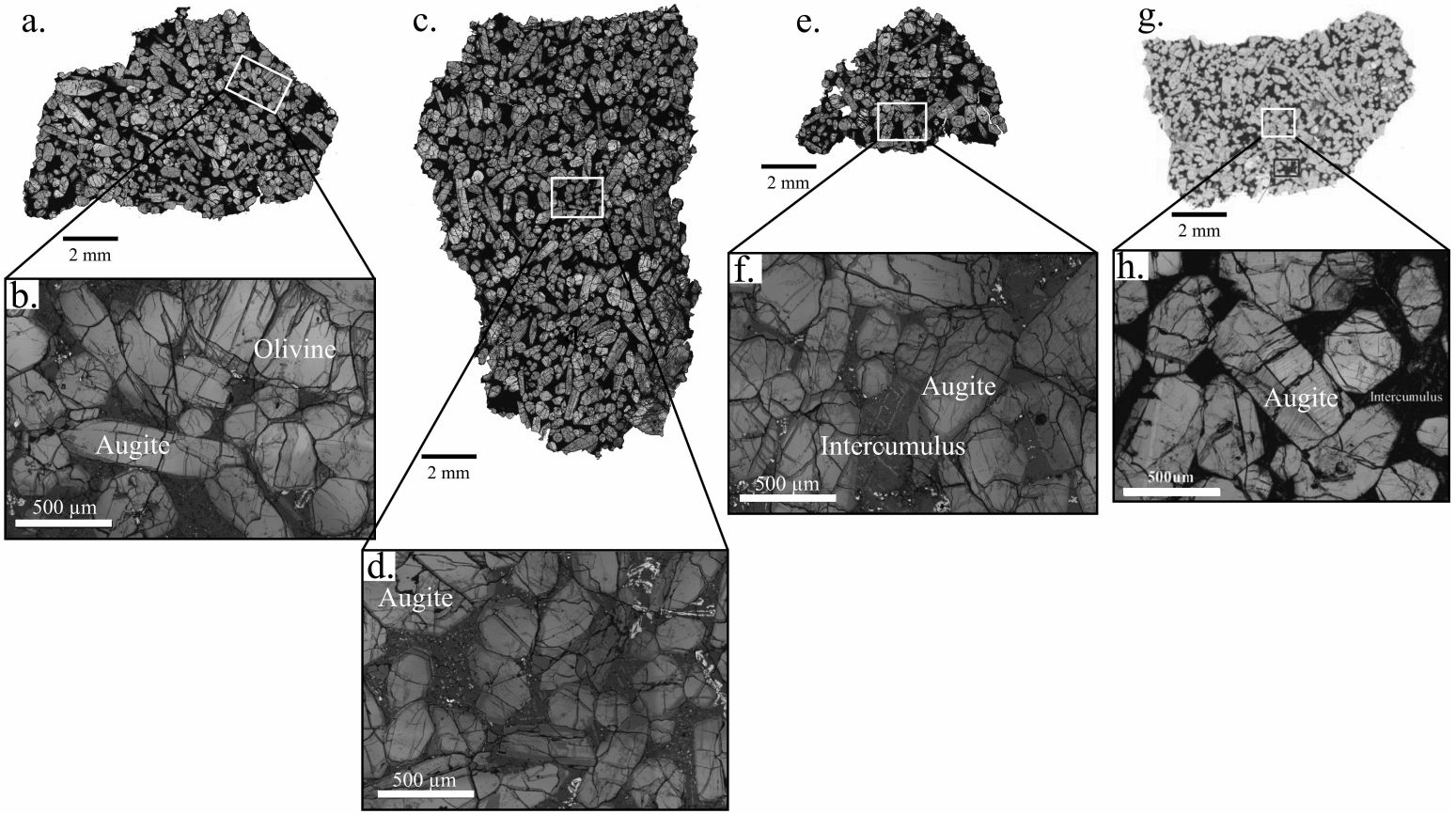
a.
2 mm
b.
Olivine
Augite
500 µm
c.
2 mm
d.
Augite
500 µm
e.
2 mm
f.
Augite
Intercumulus
500 µm
g.
2 mm
h.
Augite
Intercumulus
500µm

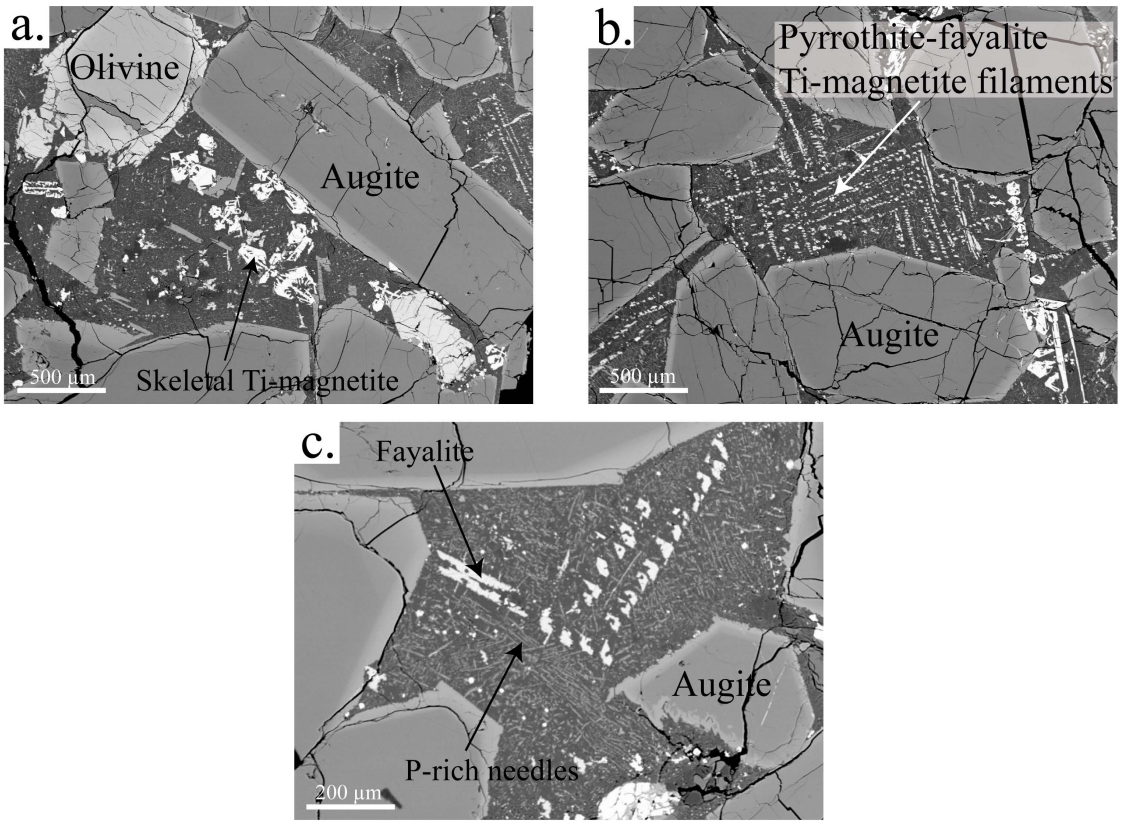

Figure C4. Backscattered electron images of intercumulus phase. a) skeletal Ti-magnetite in MIL 090030, b) pyrrhotite-fayalite-Ti-magnetite "filaments" in MIL 090032, and c) fayalite and P-rich needles in MIL 090136. The Fe-rich pyroxene rims appear lighter than the cores.

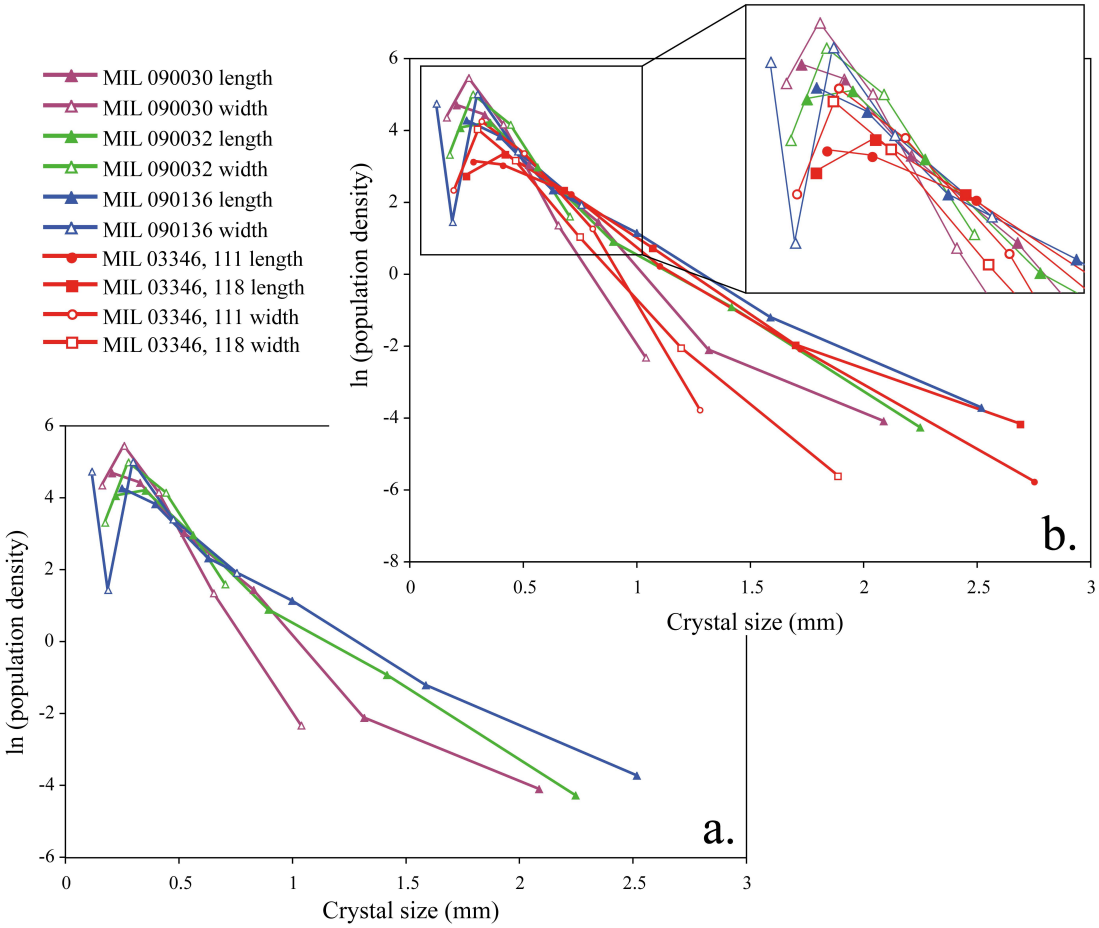

Figure C5. Crystal Size Distribution (CSD) analysis plots (population density versus crystal size) for a) MIL 090030/32/136 augites and b) MIL 090030/32/136 and MIL 03346 augites (the latter from Day et al., 2006), with crystal sizes calculated for both pyroxene crystal lengths and widths. The four meteorites display similar CSD patterns.

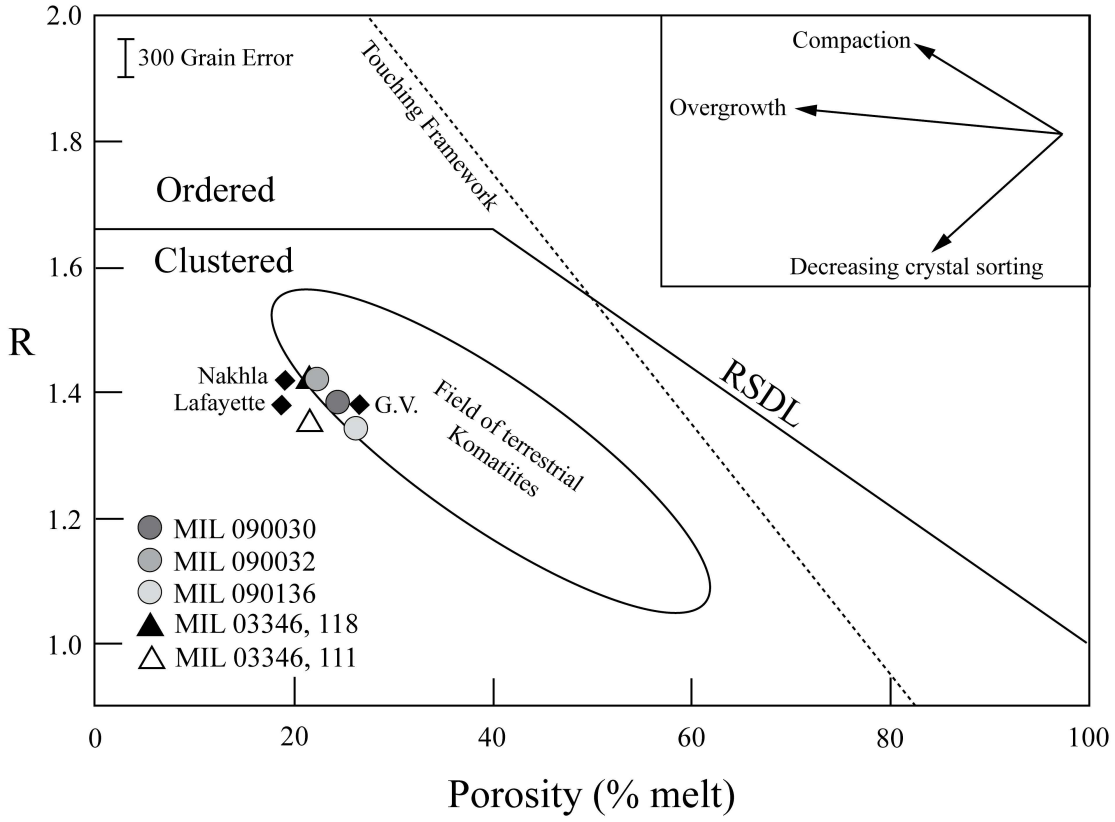

Figure C6. SDP cluster analysis diagram (Jerram et al., 2003) with new data for MIL 090030/32/136 augites, and MIL 03346 (Day et al., 2006), Nakhla, Lafayette and Governador Valadares (G.V; Lentz et al., 1999) data.

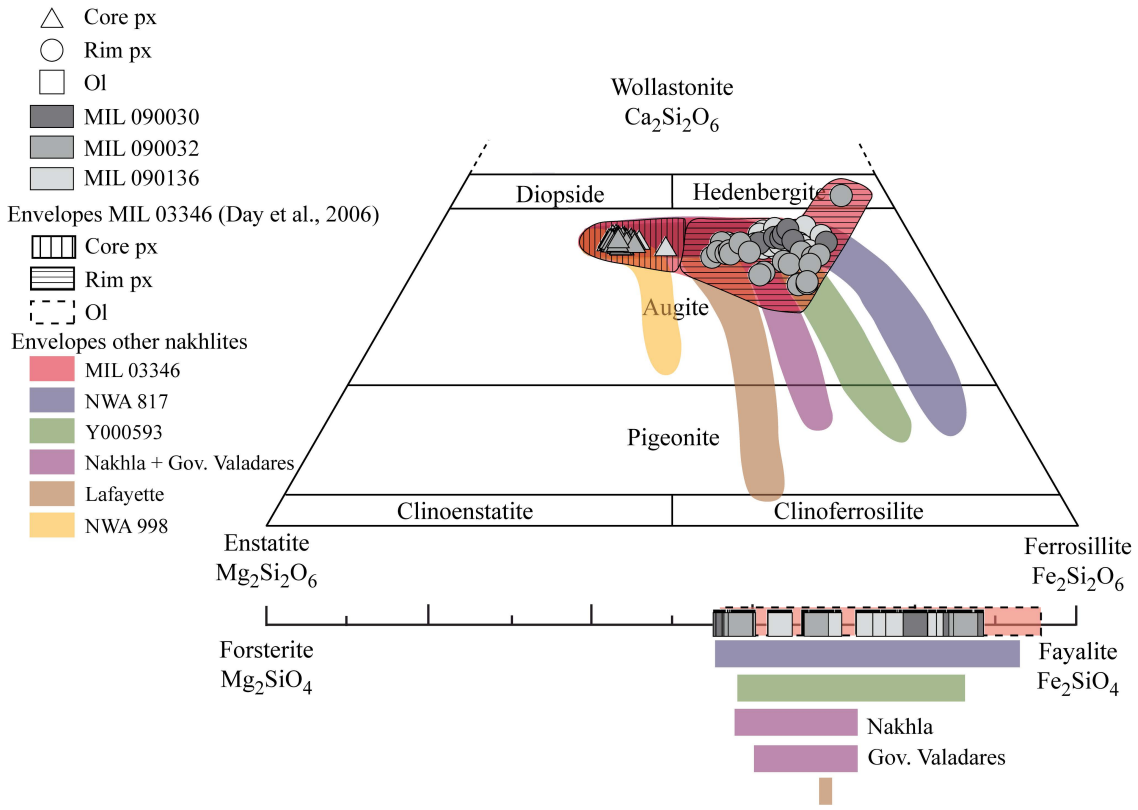

Figure C7. Pyroxene core (triangles) and rim (circles) compositions as well as olivine (squares) compositions in MIL 090030/32/136. All three nakhlites from this study have similar cumulus phase compositions. Envelopes are shown for pyroxenes in MIL 03346 (Day et al., 2006; Imae and Ikeka, 2007; Mikouchi et al., 2003; Treiman and Irving, 2008), NWA 817 (Sauter et al., 2002), Y000593, Nakhla, Governador Valadares, Lafayette and NWA 998 (Treiman and Irving, 2008; Mikouchi et al., 2003). Olivine envelopes from Sautter et al. (2002) and Day et al. (2006) for MIL 03346 and from Mikouchi et al. (2003) for NWA 817, Nakhla, Governador Valadares, and Lafayette. As all the nakhlites have similar pyroxene core compositions, the MIL 03346 pyroxene core envelope corresponds to the other nakhlite pyroxene core composition.

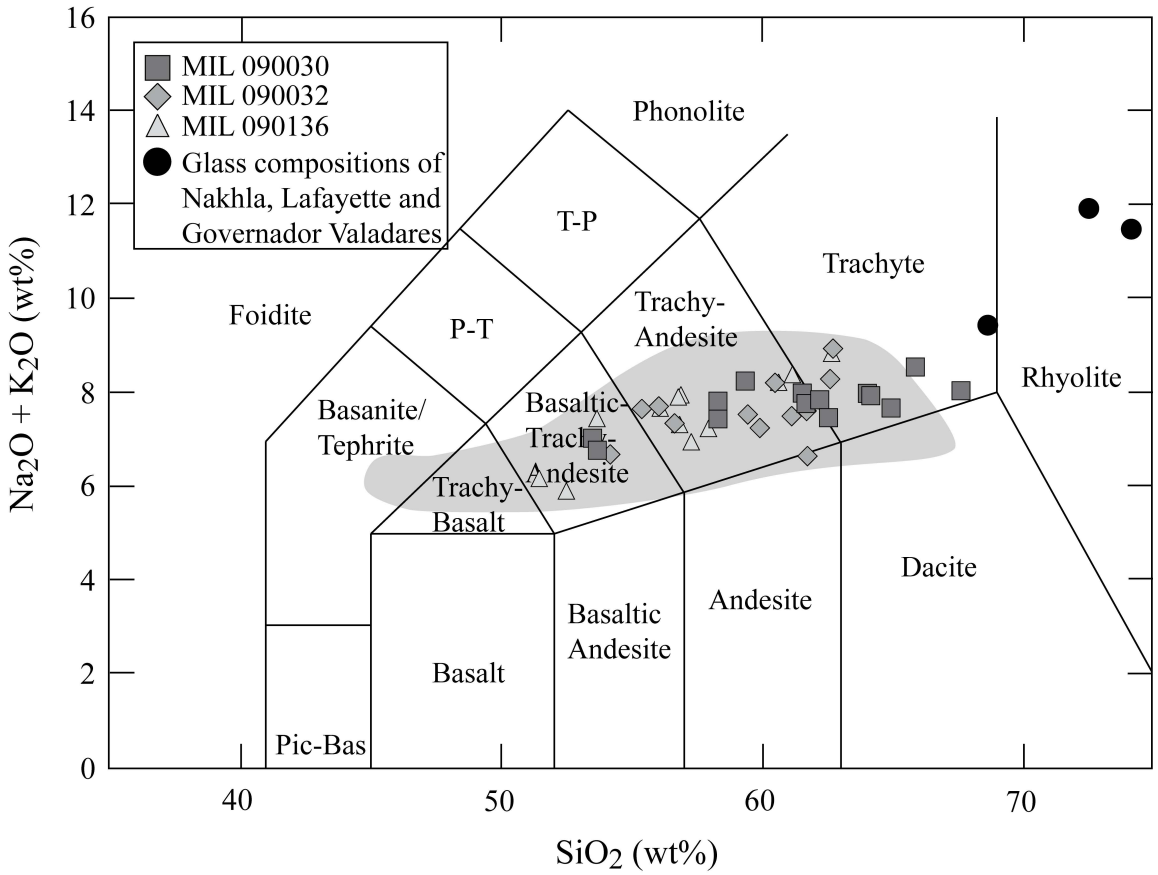

Figure C8. Total alkalis versus silica diagram showing the intercumulus phase compositions in MIL 090030, MIL 090032, and MIL 090136, with an envelope of MIL 03346 intercumulus phase compositions from Day et al. (2006). Black dots represent intercumulus glass compositions of Nakhla + Governador Valadares, Lafayette, (Berkley et al, 1980), and Yamato 000749 (Imae et al., 2005). Most of the glass compositions of MIL 090030/32/136 fall within the MIL 03346 envelope.

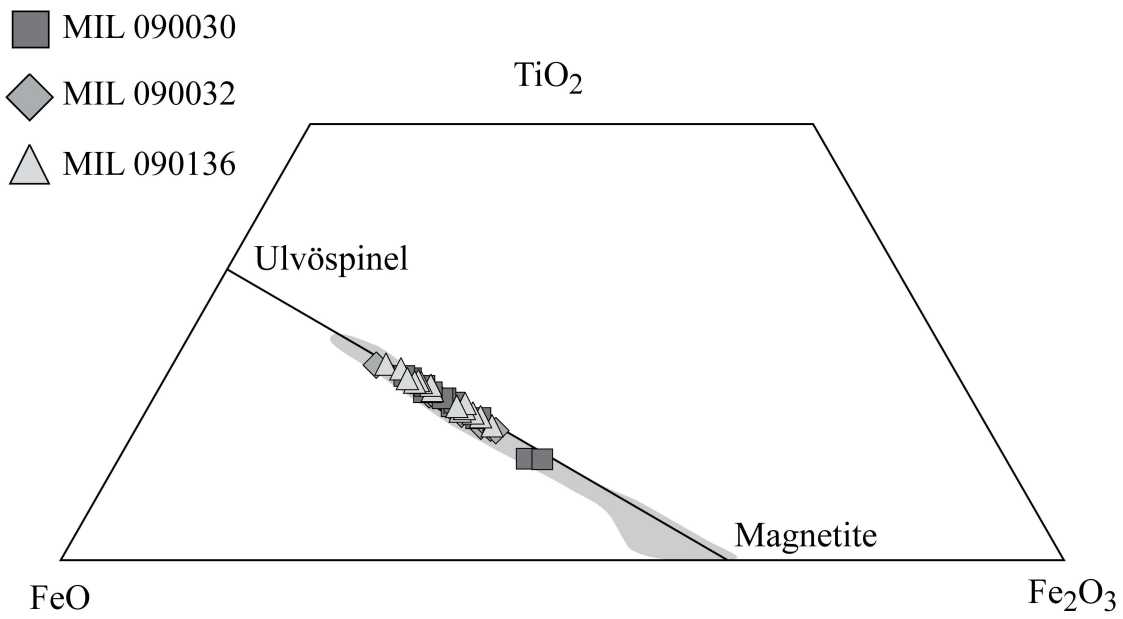

Figure C9. FeO-Fe_2O_3-TiO_2 diagram for MIL 090030/32/136 titanomagnetite, with envelope of MIL 03346 spinels from Day et al. (2006). A cluster of our data compared to the MIL 03346 envelope is observed, probably due to sampling bias.

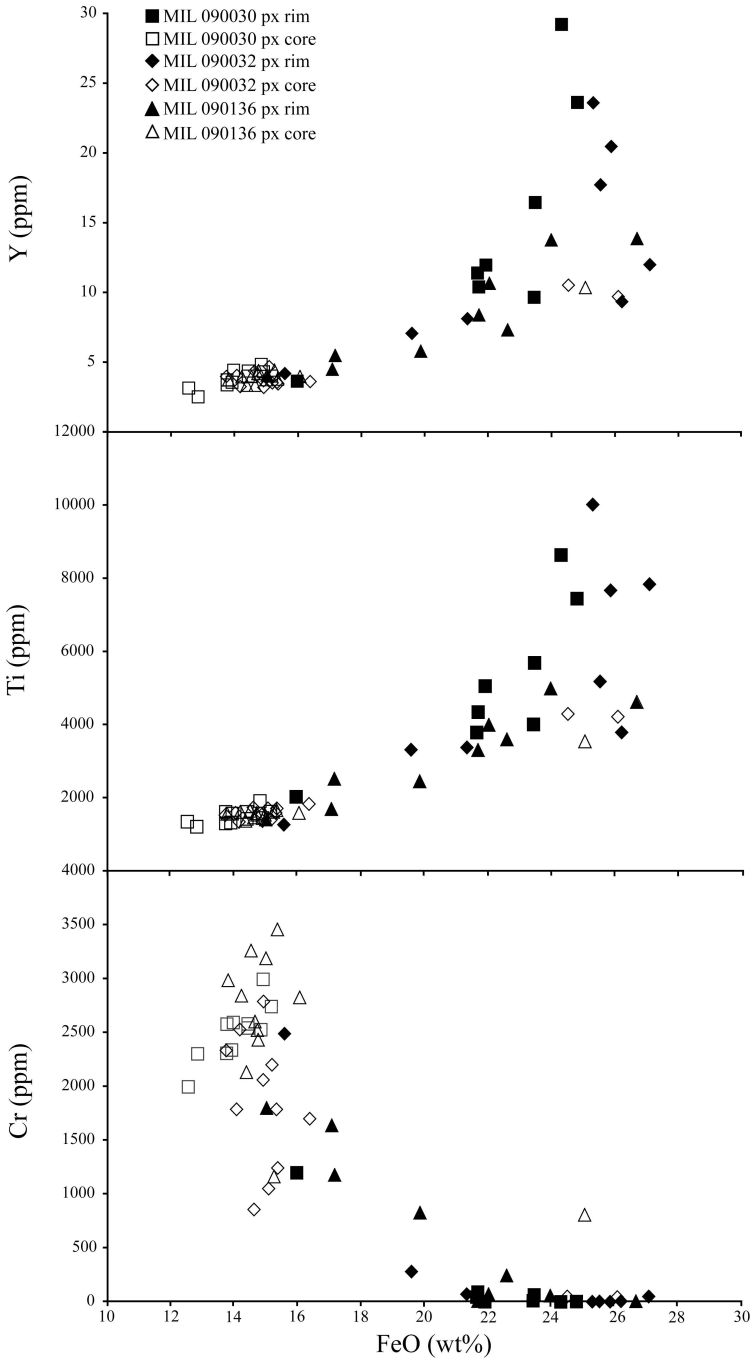

Figure C10. Abundances of Y, Ti and Cr versus Fe in pyroxene cores and rims in MIL 090030/32/136. The rims are enriched in incompatible elements (Y and Ti) and depleted in compatible elements (Cr).

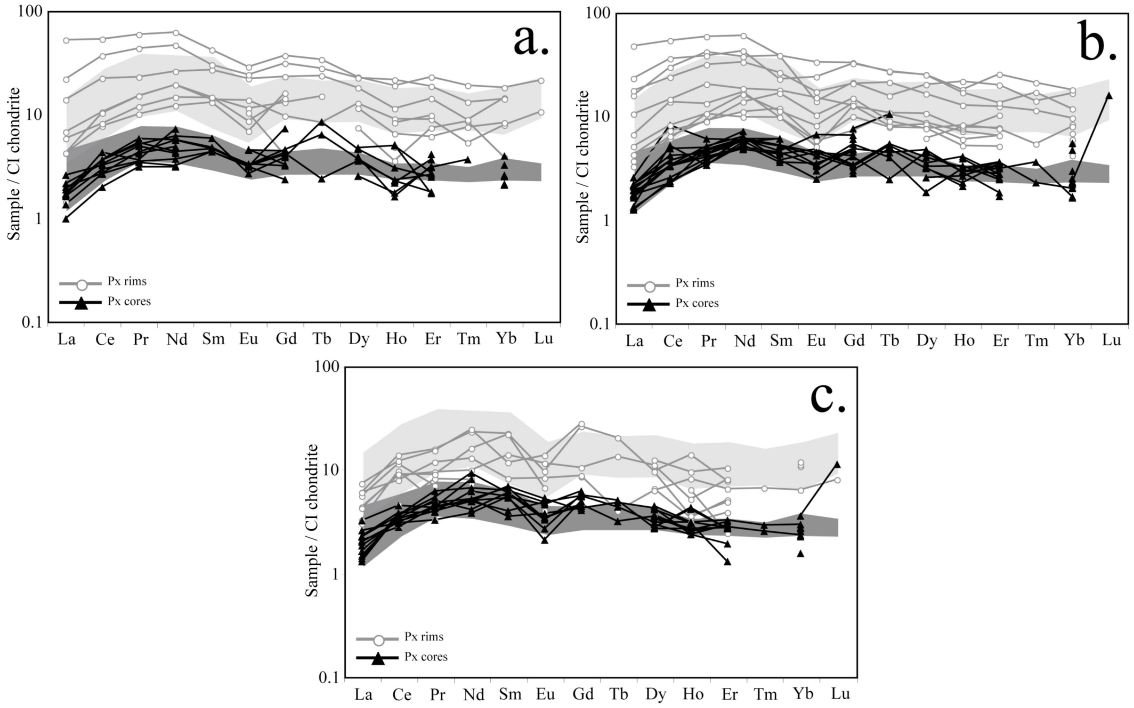

Figure C11. REE concentrations normalized to CI chondrite (Anders and Grevesse, 1989) in pyroxene rims (circles) and cores (triangles) of a) MIL 090030, b) MIL 090032, and c) MIL 090136. Envelopes of REEs in MIL 03346 pyroxene rims (light gray) and cores (dark gray) from Day et al. (2006).

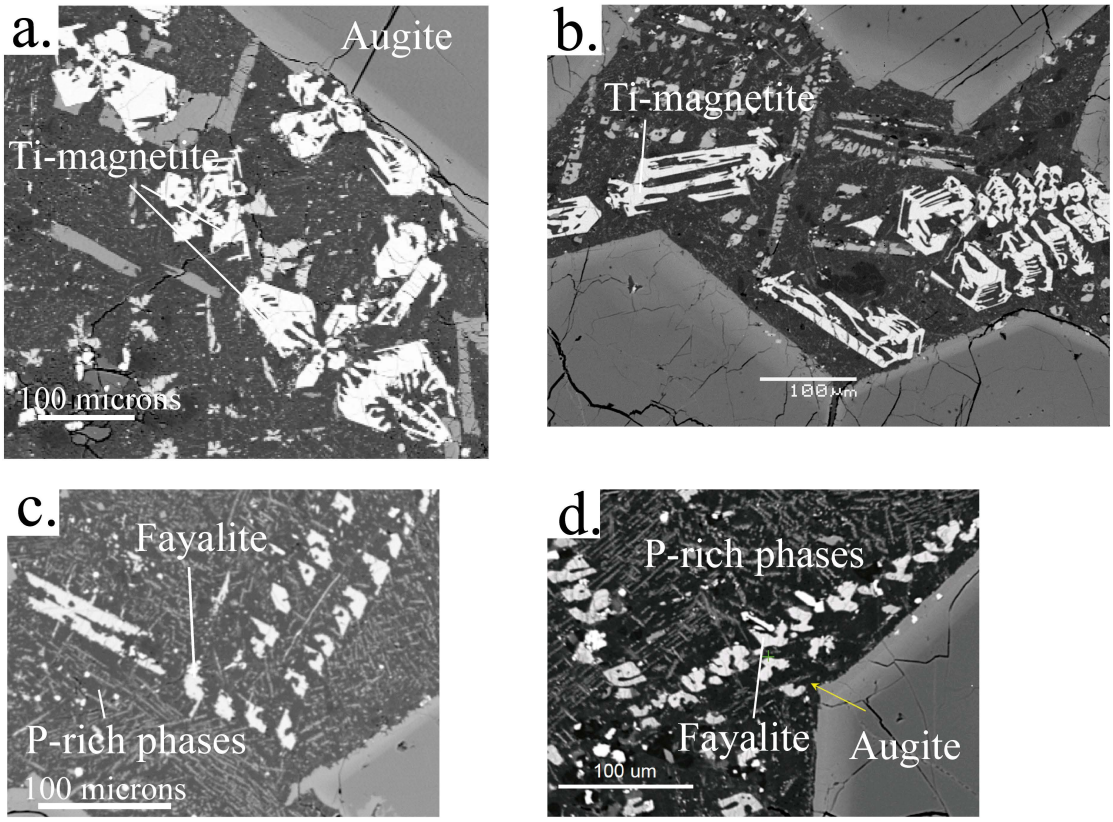

Figure C12. Back-scattered electron images of a) titanomagnetite in MIL 090030 and b) titanomagnetite in MIL 03346 (Righter et al., 2008; reprinted with permission), c) P-rich phases and fayalite in MIL 090136 and d) P-rich phases and fayalite in MIL 03346 (McKay and Schwandt, 2005; reprinted with permission). Images a) and b) and images c) and d) are at the same scales.

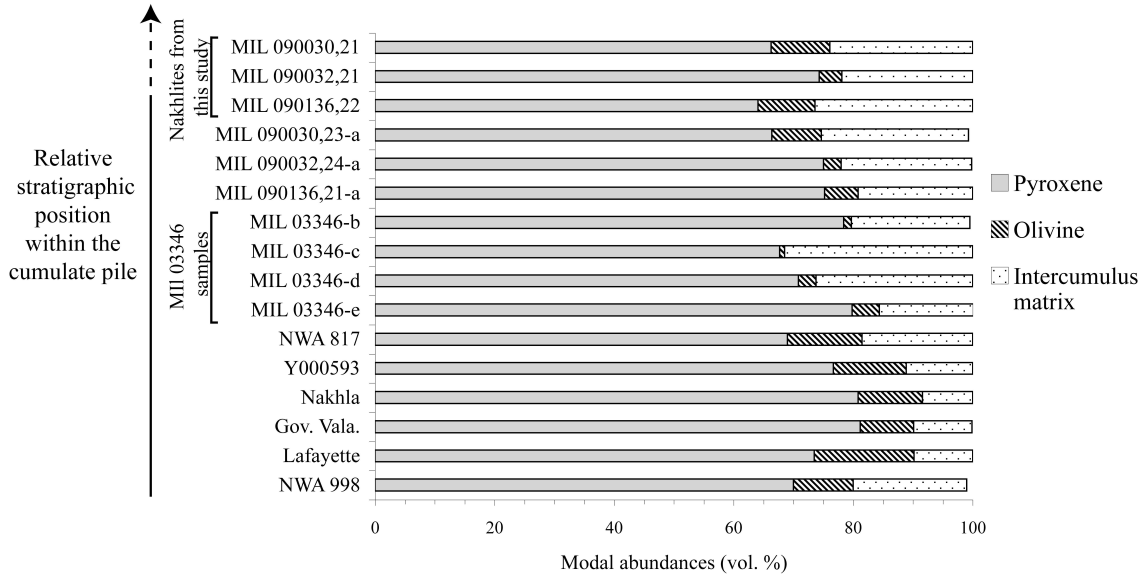

Figure C13. Histograms showing modal abundances of pyroxene, olivine, and intercumulus phase from nakhlites. The sources of data are given in Table 1. The different MIL 03346 samples and MIL 090030/32/136 samples are not presented in any particular order.

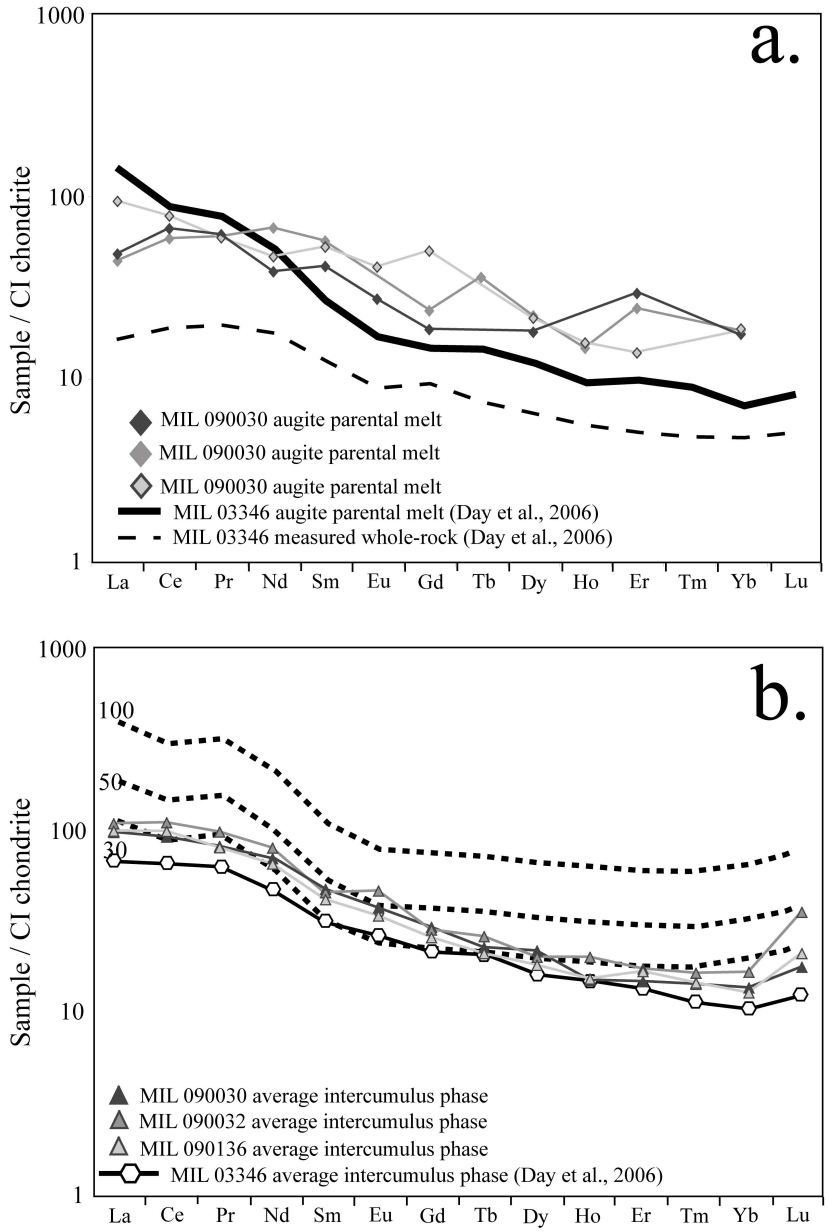

Figure C14. CI chondrite-normalized (Anders and Grevesse, 1989) REE patterns for: a) Calculated pyroxene parental magma of MIL 090030/32/136 and MIL 03346 (Day et al., 2006) and measured whole-rock of MIL 03346 (Day et al., 2006). The parental magma patterns of MIL 090030/32/136 are parallel to the MIL 03346 whole-rock (see text for details). b) Fractional crystallization model calculated by Day et al. (2006) with amount of fractional crystallization and average intercumulus phase REE compositions of MIL 090030/32/136 and MIL 03346 (Day et al., 2006). The average intercumulus phase compositions correspond to 30% fractional crystallization, supporting the Day et al. (2006) model.

CHAPTER IV
PETROGENESIS OF A VITROPHYRE IN THE MARTIAN METEORITE BRECCIA NWA 7034

This chapter is a reformatted version of a paper of the same name that is in review in Geochimica et Cosmochimica Acta. Arya Udry, Nicole Lunning, Harry McSween, and Robert Bodnar are the authors of this paper manuscript. Arya Udry and Nicole Lunning collected all the data analysis.

Abstract

Northwest Africa (NWA) 7034 and its paired meteorites NWA 7533 and NWA 7475 are the first recognized martian polymict breccia samples. An unusual, large, subrounded clast in NWA 7034 shows a vitrophyric texture, consisting of skeletal pyroxene and olivine with mesostasis. This lithology has not been observed in the paired meteorites. It crystallized under disequilibrium conditions as indicated by its olivine and pyroxene $K_D^{Fe/Mg}$, as well as reversed order of crystallization and mineral compositions relative to those predicted by MELTS. We report the highest bulk Ni value (1020 ppm) measured in any known martian meteorite or martian igneous rock, suggesting an impact melt origin for the vitrophyre. Addition of 5.3-7.7% chondritic material would account for the Ni enrichment. The bulk major and trace element abundances of the vitrophyre indicate that the protolith was not the host breccia nor any other martian meteorites. However, the clast is compositionally similar to Humphrey rock in Gusev crater analyzed by the Spirit rover and to a texturally distinct group of clasts in the paired meteorite NWA 7533. Thus, we propose that the target rock was an igneous lithology similar to Gusev basalts, which was subsequently contaminated by a chondritic impactor.

Introduction

The surface of Mars is covered with a pervasive regolith, but until recently all known martian meteorites were igneous rocks. However, the paradigm changed with recovery of the paired meteorites NWA 7034 (Agee et al., 2013), 7475 (Korotev et al., 2013), and 7533 (Hewins et al., 2013a). NWA 7034 was initially described as a monomict volcanic breccia (Agee et al., 2013), but later descriptions of these paired meteorites indicate that they are polymict regolith breccias (Hewins et al., 2013a; 2013b; 2014; Humayun et al., 2013a; 2013b; Santos et al., 2014; Goderis et al., 2014). These breccias potentially provide an opportunity to study clasts of previously unsampled martian rocks. Our investigation focuses on a vitrophyric clast (Fig. D1) in NWA 7034 whose protolith may represent a rock type not represented in meteorite collections.

Evidence that NWA 7034 is from Mars includes the composition of its trapped noble gases (Cartwright et al., 2013), its oxygen isotopic composition, and the Fe/Mn ratios of its pyroxenes (Agee et al., 2013). Its cosmic ray exposure age (^{21}Ne) is 11.4 Ma (Cartwright et al., 2013), coinciding with the Mars ejection ages for nakhlites and chassignites (e.g., McCubbin et al., 2013).

A polymict classification for NWA 7034 and 7533 (and by extension the other paired meteorites) is supported by the occurrence of clasts of multiple igneous lithologies, variously described as microbasalts, norite, monzonite, and mugearite (Hewins et al., 2014), or as basalt, trachyandesite, and basaltic andesite (Santos et al.,

2014), as well as fine-grained clast-laden melt rocks. Zircon U-Pb ages of 4.44, 4.35, and 4.10 Ga (Humayun et al., 2013a; Yin et al., 2014) further demonstrate the polymict nature of these breccias. The polymict nature of these breccias indicates a regolith origin (e.g., Humayun et al., 2013a). These breccias were likely assembled at 1.44 Ga (Yin et al., 2014). They also experienced the addition of exogenic material, as indicated by their high nickel concentrations (corresponding to ~5% CI-chondrite), chondritic platinum-group element (PGE) enrichments, and $^{187}Os/^{188}Os$ ratios in both NWA 7034 and 7533 (Humayun et al., 2013a; Goderis et al., 2014). Additionally, vitrophyric clasts and an accretionary lapillus, likely formed by a water-saturated impact plume, were observed in NWA 7475 (Wittman et al., 2013) but not in the other paired meteorites. Although the breccia textures appear different from the few modern martian soils that have been analyzed (e.g., McGlynn et al., 2011), we have not studied soils of equivalent age and they are likely to vary from place to place.

This study focuses on the formation of the single vitrophyric clast in NWA 7034 (Figs. D1 and D2a-c) initially noted by Agee et al. (2013). Its large size (5 x 4.5 mm) and relatively fine-grained texture suggest that it might be compositionally representative, allowing a more rigorous interpretation of its origin and significance.

Methods

We analyzed a single vitrophyric clast with a surface area of 22 mm^2 in thin section NWA 7034,03 (Fig. D1). We estimated modal abundances by a point counting technique using back-scattered electron (BSE) images and ENVI 4.2 software.

In situ major and minor element compositions were measured using the CAMECA SX-100 electron microprobe (EMP) at the University of Tennessee. Mineral and mesostasis compositions were determined using an accelerating voltage of 15 kV, beam current of 20 nA, counting times of 20 s except for Ca (30 s), Cr (30 s), and Ni (80 s) in olivine, and beam sizes of 1-2 μm (pyroxene and olivine) and 10 μm (mesostasis), using standard PAP corrections. Both natural and synthetic standards were measured. The detection limits were 0.03 wt% for SiO_2, TiO_2, Al_2O_3, MgO, CaO, P_2O_5, Na_2O, NiO, and K_2O and 0.05 wt% for FeO, MnO, and Cr_2O_3 with 1-2% precision of the amount measured for major oxides >10 wt% and increasing to 5% precision for analyses down for major oxides <1 wt%

In situ trace element abundances were measured at Virginia Tech using an Agilent 7500ce inductively coupled plasma mass spectrometer (ICP-MS) combined with an Excimer 193 nm GeoLasPro Laser Ablation (LA) system. Laser spot sizes of 60 μm were used to measure mesostasis. For bulk point (multiple phase) analyses, we used spot sizes between 120 and 160 μm. Reference glass NIST SRM610 was used as the external standard. For each of the analyses, approximately 60 s of background signal was collected before the ablation process was initiated. The NIST standard was measured twice for 60 s every 2 hours to correct for drift. Sample ablation times ranged from 40-60 s using a laser repetition rate of 5 Hz. The samples were ablated in a helium atmosphere. The helium gas carrying the ablated particles was then mixed with the make-up gas (argon) before entering the ICP-MS system. The analytical precision for the LA-ICP-MS

system for the elements analyzed in this study (compared to NIST612) is better than ±5% relative (for V, Co, Cr, Ce, Zn, Ga); between ±5 and 10% (for Ni, Rb, Nb, Cs, Sr, Ba, Pr, Eu, Hf, Pb); between ±10 and 20% (for Y, Zr, La, Nd, Sm, Gd, Dy, Er, Yb, Ta, Lu, Th, Tb, Ho, U), and poorer than ±20% (Sc). Analytical precision was determined previously using the NIST standard 610 as the reference, and then USGS standards BCR-2G, BHVO-2G, BIR-1G, NKT-1G and NIST standards NIST612 and NIST614) were analyzed according to established analytical protocols. USGS standards BCR-2G, BHVO-2G, and BIR-1G are natural basalt glasses, and NKT-1G is a natural nephelinite glass. Details of the analytical results related to these analyses are available at:http://www.geochem.geos.vt.edu/fluids/laicpms/VT_LAICPMS_Accuracy_Precision.pdf.

The LA-ICP-MS detection limits are dependent on several factors, such as element (isotope) being measured, spot size, and duration of the analysis. Therefore, each analysis and element has a slightly different detection limit. For all of the trace elements measured, the detection limits obtained during our calibration runs described above were always less than one ppm. Data reduction was done using the Analysis Management System (AMS) software (Mutchler et al., 2008) enabling time-resolved signal analysis. An advantage of the AMS software is that it provides easy recognition of sample heterogeneities during the ablation process, such as when traversing from one phase into a different phase during ablation, or if a solid inclusion is included in the ablated material. The software allows the user to select the portion of the ablation signal to process in order to eliminate signal from multiple phases in order to obtain the composition of only the phase of interest.

We calculated equilibrium crystallization paths using the AlphaMELTS front end (Smith and Asimov, 2005) of the MELTS algorithm (Ghiorso and Sack, 1995) using the major element bulk composition of the vitrophyre and assuming a pressure of 1 atm with an oxygen buffer at fayalite-magnetite-quartz (FMQ), based on published oxybarometers derived from martian meteorites, and no H_2O.

Petrography and mineral compositions of the vitrophyre

Texture and mode

Although many of the clasts in this breccia are angular, the vitrophyre does not show an angular contact with the host breccia. The complete contact of the clast with the host breccia is not visible, but the observable contact is subrounded and smooth. The vitrophyric texture has not been previously observed in martian meteorites (Figs. D1 and 2a). The clast consists of mesostasis and elongated skeletal crystals of pyroxene and olivine (Fig. D2a), which has not been noted for other clasts in this breccia or its paired meteorites. The pyroxene crystals range from 0.2 to 1.5 mm in length. Olivine grains show a “hopper” morphology (Donaldson, 1976) and range from 0.1 to 1 mm in length. Modal (vol. %) abundances in the clast are 75% mesostasis, 18% pyroxene, 7% olivine, and trace oxides.

Some edges of the clast show a 300-μm wide boundary region that is distinct from the clast interior. This region contains finer-grained acicular pyroxene aligned parallel to

the contact (Fig. D2b), as well as a higher abundance of Fe-oxides and an absence of olivine.

Wavelength dispersive spectra (WDS) elemental maps were used to search for the presence of Fe-oxides, chromite, phosphate, and sulfide. In contrast to the rest of the breccia, the vitrophyre contains substantially lower modal abundances of Fe-oxides (Table D1) and contains no detectable phosphate, chromite, or sulfide.

Major element mineral chemistry

In the interior of the vitrophyre, skeletal pyroxene grains show slight compositional zoning, with an average core composition of $En_{69}Fs_{28}Wo_3$ and average rim composition of $En_{60}Fs_{35}Wo_5$ (Fig. D3: squares; Table D1). The pyroxenes are generally more Fe-rich and Ca-depleted than those in other martian meteorites (Fig. D3). On a plot of Mn versus Fe, commonly used to determine parent body provenance (Papike et al., 1998), the pyroxenes plot on an extension of the terrestrial trend but below the Mars trend, at the edge of the field for pyroxenes in the rest of the breccia (Fig. D4a).

The olivine grains have compositions of $Fo_{55\text{-}63}$ (Fig. D3: triangles; Table D1) and appear to be compositionally zoned. The rims are too small to be analyzed in individual crystals, but the observed compositional range likely represents different zones in slices through the crystals. The olivines are Fe-enriched compared to pyroxenes. The Mn-Fe contents of olivines plot on the Mars trend, but their distribution is scattered around that trend line (Fig. D4b).

The mesostasis has a mostly homogeneous basaltic composition, as shown in a total alkalis versus silica (TAS) classification diagram (mesostasis: Fig. D5a, Table D2). Nonetheless, some local areas deviate in major element composition from the rest of the mesostasis. We recognize 5 different phases: mesostasis and 4 additional compositional variants (Figs. D2c and D5a-c), which comprise 3 endmembers (mesostasis, and variants 2 and 4) and 2 intermediate compositions (variant 1 plots between mesostasis and variant 2, and variant 3 plots between variants 2 and 4). Variant 2 shows enrichment in SiO_2, Al_2O_3, and alkali elements and depletion in FeO_T compared to the mesostasis. Variant 4 is strongly enriched in SiO_2 (plotting in the rhyolite field on the TAS diagram) and depleted in alkalis and FeO_T. These different mesostasis variants presumably represent different portions of the protolith that melted, and the compositionally distinct melts were unable to mix to produce a homogeneous glass before the melt was quenched. Variants 1 to 4 are dark in BSE images (Fig. D2c) and we cannot discern crystallinity in them, but we cannot rule out the presence of microcrystals of alkali feldspar (variant 2) or silica (variant 4). These two compositional endmembers might have been silica-rich and alkali feldspar-rich areas in the protolith, which were not homogenized during melting due to different melt viscosities.

Trace and REE mineral chemistry

Measured rare earth element (REE) abundances for the mesostasis are presented in Table D3. We only analyzed the mesostasis for trace elements and were not able to measure trace elements in pyroxenes and olivines due to their small crystal sizes and hollow skeletal textures. All of the REE trends show a decreasing enrichment from light

REE (LREE) to heavy REE (HREE). Mesostasis REE patterns show negative or nearly flat Eu anomalies, with Eu/Eu* between 0.31-1.07.

Bulk vitrophyre major and trace element chemistry

Figure D6 shows the bulk-vitrophyre major element composition calculated using modal-weighted EMP analyses of pyroxene, olivine, and mesostasis (Table D4). The vitrophyre composition plots below the martian meteorite Fe-Mn line (Fig. D6a), and is similar to basaltic rocks (Adirondack, Humphrey, and Mazatzal) in Gusev crater analyzed by the Spirit rover (McSween et al., 2006; 2008). The FeO content of the vitrophyre (15.5 wt%) is higher than that for the whole-breccia composition (10 wt %; Agee et al., 2013), as well as that of Gusev basalts and most martian meteorites (Fig. D6a). The vitrophyre plots in the basaltic field in the TAS diagram and has an alkali content similar to the Gusev basalts, whereas the bulk-breccia composition shows enrichment in alkalis compared to the vitrophyre and martian meteorites (Fig. D6b). Figures D6c and D6d demonstrate that the Ca/Si, Al/Si, and Mg/Si ratios of the vitrophyre are closer to Gusev basalt compositions than to any known martian meteorites. We also compared the bulk composition of NWA 7034 to the fine-grained clast-laden impact melt rocks (CLIMR) from NWA 7533 (Humayun et al., 2013a). These impact melt rocks show a different texture and mineralogy from the NWA 7034 vitrophyre: plagioclase and subophitic pyroxene are present but olivine and mesostasis do not occur. The major element compositions of clast-laden impact melt rock are more similar to those of the NWA 7034 vitrophyre than they are to compositions of the NWA 7034 host breccia. The bulk composition of the vitrophyre is similar to Gusev soils (McSween et al., 2009) except that the vitrophyre has higher Fe/Si (Fig. D6a). The clast-laden impact melt rocks also fall within the field of Gusev soils but have a slightly higher Mg/Si ratio (Fig. D6c).

We analyzed a number of trace elements and compared their concentrations to available martian data (Table D4). Trace element trends of the bulk vitrophyre, host breccia, and NWA 7533 clast-laden impact melt rocks are similar despite the fact that the host breccia is more enriched in incompatible elements relative to CI-chondrite compared to the NWA 7034 vitrophyre (Fig. D7: on average ~20 ppm/CI-chondrite more than the vitrophyre composition). In contrast, Humphrey is slightly depleted in K and Ti relative to CI-chondrite compared to the vitrophyre (2.4 wt% versus 1.5 wt% and 15.7 wt% versus 7.5 wt%, respectively).

The bulk vitrophyre REE compositions are presented in Figure D8. The REE pattern shows a negative slope toward HREE and a small negative Eu anomaly (Eu/Eu* = 0.78). The vitrophyre pattern is parallel to the NWA 7034 host breccia REE pattern (Agee et al., 2013), but shows lower REE concentrations than the bulk breccia (10-28 x CI-chondrite versus 26-58 x CI-chondrite). The vitrophyre has elevated LREE and higher La/Yb (2.55) compared to the shergottite meteorites (Fig. D8a) and ALH 84001 (Fig. D8b). It is less enriched in LREEs compared to the nakhlites and Chassigny (Fig. D8b). The clast-laden impact melt rocks trend (Humayun et al., 2013a) is parallel to that of the NWA 7034 vitrophyre and host breccia (Agee et al., 2013) but shows values intermediate between these two trends.

Discussion

Vitrophyre cooling rate and disequilibrium

Although the quenched texture in the vitrophyre has not been previously described in martian rocks, similar textures have been observed in some impact melt rocks on Earth (e.g., Rondot, 1971; French et al., 1989), on the Moon (e.g., Papike et al., 1976; 1998; Warner et al., 1978; Symes et al., 1998; Ruzicka et al., 2000; Norman et al., 2006), and in ordinary chondrites (Rubin, 1985; Bogard et al., 1995). The skeletal textures of both olivine and pyroxene indicate a high degree of undercooling. According to crystal growth experiments, these features correspond to very fast cooling rates, on the order of thousands of degrees Celsius per hour (Faure and Schiano, 2005; Faure et al., 2003).

Rapid cooling of the vitrophyre would lead to disequilibrium crystallization of the melt. According to the Fe-Mg partitioning value ($K_D^{Fe/Mg}{}_{ol/bulk} = 0.35$) between olivine and basaltic melt of Filiberto and Dasgupta (2011), the vitrophyre olivines are not in equilibrium with the bulk composition ($K_D^{Fe/Mg}{}_{ol/bulk} = 0.63$). Additionally, the partitioning of Fe/Mg between olivine and pyroxene ($K_D^{Fe/Mg}{}_{ol/px}$) is not consistent with equilibrium. Using our data for compositions of olivine and pyroxene in the vitrophyre, we obtained a $K_D^{Fe/Mg}{}_{ol/px} = 1.6$ for the vitrophyre whereas Longhi and Pan (1989) determined a $K_D^{Fe/Mg}{}_{ol/px}$ of 1.1 for SNC-composition magmas.

Application of the MELTS algorithm to the bulk vitrophyre composition predicts that olivine would crystallize before pyroxene (both pigeonite and augite) under equilibrium conditions. Olivines are predicted to crystallize at 1275 ºC and pyroxene at 1165 ºC. However, in the vitrophyre we interpret pyroxene to have crystallized prior to olivine based on textural evidence: pyroxene is the only phase in the boundary layer and where olivine appears in the interior of the clast, it forms in interstices between pyroxene crystals. The Fe-rich olivine compositions suggest that olivine nucleation might have been suppressed at a fast cooling rate (Donaldson et al., 1975). The greater abundance and earlier crystallization of pyroxene may suggest that the melt was not superheated and preserved relict pyroxene nuclei that seeded crystallization of pyroxene (e.g., experiments of Lofgren and Russell, 1986).

Volcanic or impact melt?

To ascertain whether the NWA 7034 vitrophyre had a volcanic or impact melt origin, we analyzed its bulk Ni content. Nickel is a good indicator of impact contamination, because most impactors (chondrites) are enriched in siderophile elements compared to martian rocks (200 ppm vs 11,000 pm for CI-chondrites: Wasson and Kallemeyn, 1988; Yen et al., 2005). Based on Ni content, Yen et al. (2005) suggested an addition of 1.2% of CI-chondrite in martian soils, similar to the chondritic component in lunar soils (1.9%: Ganapathy et al., 1970). Figure D6e shows that the Ni content in the vitrophyre (1020 ppm) is significantly higher than in other martian rocks, including the NWA 7034 breccia (392 ppm: Agee et al., 2013) and other martian meteorites but is similar to that in Gusev soils. The Ni content of the vitrophyre is higher than in NWA 7533 clast-laden impact melt rocks (589 ppm: Humayun et al., 2013a), which are

unambiguously impact-melt rocks based on their Ir concentrations. Thus, we suggest that the NWA 7034 vitrophyre is also an impact melt contaminated by chondritic material.

We calculated the exogenous Ni content in the vitrophyre assuming that the Mg/Ni ratio in the Gusev basalt Humphrey represents a martian igneous Ni value. If the vitrophyre formed by complete impact melting of the Humphrey (Mg/Ni = 382), the indigenous Ni would be 170 ppm and thus 850 ppm Ni would be from a non-martian source. Nickel has been enriched in martian soils from earlier impacts throughout martian history (e.g., Gellert et al., 2006). Thus, the non-indigenous 850 ppm Ni could have been incorporated into martian soils that subsequently underwent impact melting. Using the Ni contents of L-, H-, and CI-chondrites (Wasson and Kallemeyn, 1988; Anders and Grevesse, 1989), we calculate that the exogenic Ni requires the addition of 7.7 % CI-chondrite as an upper limit. These values are considerably larger than the CI-chondritic component in Gusev soils of 1.2% (Yen et al., 2005), lunar soils of 1.9% (Ganapathy et al., 1970), and the NWA 7533 clast-laden impact melt rocks of 5% (Humayun et al., 2013a) but similar to some lunar crystalline impact melt rocks (Norman et al., 2002). Based on the exogenic Ni content of the vitrophyre and the CI-chondrite Ni/Ir, we estimate that the Ir concentration should be close to 40 ppb, which is similar to the Ir content in clast laden impact melt rocks (33 ppb: Humayun et al., 2013a). Further direct measurements of Ir and other siderophile elements could provide additional evidence to support the chondritic component inferred from Ni concentrations.

Was the precursor material the host breccia or martian soil?

We investigated the compositional and textural features of the vitrophyre to determine if it formed by impact melting of the host breccia. The bulk major and trace element composition of the vitrophyre is different from the NWA 7034 bulk-breccia composition of Agee et al. (2013) (Figs. D6-8). Bischoff and Stöffler (1992) described impact melting of chondrite and achondrite breccias. These melts have the same compositions of the precursor materials except in instances of very small amounts of partial melting. Therefore, the differences in bulk chemistry between the host breccia and the vitrophyre provide evidence that the host breccia was not the target material. Textural evidence also suggests the vitrophyre did not melt *in situ*: the outer boundary of the melt droplet did not co-mingle with the host breccia, nor does the vitrophyre contain unmelted relict material from the breccia. Impact melts that formed *in situ,* such as those described in the Chico chondrite (Bogard et al., 1995), exhibit comingling of melt with unmelted material. Pyroxene grains in the clast boundary region are aligned along the contact, which could suggest that the clast was incorporated into the host breccia as a droplet that was still ductile enough for the pyroxene near the edge to physically conform to the boundary, but was not hot enough to flow into or interact with the surrounding material. Alternatively, this crystal alignment along the boundary could have occurred as the melt droplet traveled through the atmosphere. Some crystal-bearing lunar spherules have crystals aligned along portions of their edges (Symes et al., 1998; Ruzicka et al., 2000). Additionally, the lack of olivine in the boundary region, combined with chemical evidence that pyroxene crystallized before olivine, implies that the boundary region likely solidified before the interior of the clast. Thus, we infer that the vitrophyre is an impact

melt droplet that did not form from the regolith breccia in which it now resides.

Gellert et al. (2006) determined that undisturbed Gusev soils are enriched in Ni, Zn, Cl, S, and P compared to the Gusev rocks. As mentioned above, the vitrophyre Ni content is significantly higher than martian rocks but similar to martian soils. Cl and P were not measured in the vitrophyre. However, Zn and SO_3 are both depleted in the vitrophyre relative to Gusev soils: Zn is 14 ppm versus 320 ppm and SO_3 is 0.2 wt% versus 5.7 wt%, respectively (Yen et al., 2005). This suggests that little or no soil was incorporated into the vitrophyre during impact and that the precursor material for the vitrophyric impact melt was not regolith.

Was the precursor a known martian igneous rock composition?

The compositions of minerals in the vitrophyre are distinct from those in most other martian meteorites. A notable exception is the vitrophyre olivine, which has a similar composition to olivine in olivine-phyric shergottites. Vitrophyre pyroxene is compositionally distinct from pyroxenes in nakhlites or chassignites (Fig. D3). Nakhlites only contain augite, whereas the pyroxene in the vitrophyre is low-Ca pyroxene. Chassignite pyroxenes display low Fe contents compared to other martian meteorites and NWA 7034 (Fig. D3). Although lower in Ca than the pyroxenes in most shergottites, vitrophyre pyroxene exhibits Fe, Mg, and Ca concentrations similar to pyroxene cores in some olivine-phyric shergottites (e.g., Basu Sarbadhikari et al., 2009; Gross et al., 2013). The quenched textures and rapid crystallization could explain the very low Ca-pyroxene and basaltic mesostasis compositions, which are unique compared to those found in other martian meteorites. These quenched minerals did not have the necessary time to evolve and become enriched in elements such as Ca. In addition, vitrophyre pyroxene rims and cores show enrichment in Al and Ti, and depletion in Cr compared to the martian meteorite pyroxenes. The vitrophyre pyroxene falls within the Fe-Mg range of Adirondack basalt pyroxenes, inferred from Mössbauer measurements (Morris et al., 2004). However, they cannot be compared directly because Ca was not measured in Adirondack pyroxene (McSween et al., 2006). The vitrophyre mesostasis and variants were previously compared to shergottite maskelynite and nakhlite intercumulus glass (Fig. D5). The mesostasis is more enriched in MgO and FeO and depleted in SiO_2 compared to glasses described in other martian meteorites (Table D2). The mesostasis and variant compositions in the vitrophyre are also different from the martian glass compositions. Overall, phase compositions in the NWA 7034 vitrophyre are distinct from those found in other martian meteorites.

We compared the bulk composition of the vitrophyre to known martian igneous rock compositions including representative basaltic, olivine-phyric, and lherzolitic shergottites, nakhlites, Chassigny, ALH 84001, Bounce Rock, and Gusev basalts. Figure D6a-d shows that the vitrophyre is depleted in Mn and enriched in alkali elements compared to shergottites, and has Ca/Si, Mg/Si, and Al/Si ratios intermediate between those of basaltic and olivine-phyric shergottites. When compared to all other martian basalts, the vitrophyre composition most closely resembles Gusev basalts for the elements presented in Figure D6a-d.

Similar trends are not observed between the vitrophyre REE pattern and other martian meteorite trends (Fig. D8). The REE trend of the vitrophyre is defined by a La/Yb (bulk rock normalized to CI-chondrite) slope of 2.6, which is different from the La/Yb of other martian meteorites.

In addition to the graphical comparison in Figure D6, we compared the bulk vitrophyre composition to all the martian basalt compositions using best fit (least-squares) methods. We statistically compared the vitrophyre bulk composition to the other martian basalt compositions by calculating their composition differences and identify the minimum sum of squares of the major oxide compositions (Wright and Doherty, 1970). The composition most similar to the vitrophyre is Humphrey. We can refine the composition of the potential target rock by subtracting a chondritic contaminant, which varies between 5.3-7.7% depending on whether it was ordinary or carbonaceous chondrites. Notably, Humphrey is one of the few martian rocks believed to represent a primary martian magma (Monders et al., 2007). Phase equilibrium experiments could verify if the vitrophyre composition is multiply saturated with both olivine and orthopyroxene at high pressure. Further examination of this meteorite might lead to the identification of more impact melted lithologies that sample additional crustal martian rocks.

Summary and conclusions

- The NWA 7034 vitrophyre clast shows a distinctive quenched texture with elongated skeletal pyroxene and "hopper" olivine crystals. Different localized compositions of mesostasis variants likely represent silica and alkali feldspar in the protolith that were not fully homogenized during melting.

- Pyroxene, olivine, and mesostasis show major and trace element compositions that differ from minerals analyzed in other martian meteorites.

- $K_D^{Fe/Mg}{}_{ol/px}$ and $K_D^{Fe/Mg}{}_{ol/melt}$ as well as a different order of crystallization and mineral compositions relative to those calculated using MELTS, indicate disequilibrium, which we attribute to very fast cooling of the melt clast.

- We interpret the vitrophyre to have formed by impact melting, based on its very high Ni content (1020 ppm). We estimate an exogenic Ni component of 850 ppm, equivalent to the addition of 5.3-7.7% chondritic material.

- From the bulk composition and boundary texture of the vitrophyre, we infer that the protolith was not the host breccia.

- Low Zn and S concentrations indicate that the protolith of the vitrophyre did not include martian soil. The absence of a soil component differs from both the host breccia and the observations by Humayun et al. (2013a) of the NWA 7533 clast-laden impact melt rocks.

- The protolith major element composition was almost identical to the Gusev basaltic rock Humphrey. Martian polymict breccias potentially include igneous lithologies, like this vitrophyre, that are not represented as martian meteorites.

References

Agee C. B., Wilson N. V., McCubbin F. M., Ziegler K., Polyak V. J., Sharp Z. D., Asmerom Y., Nunn M. H., Shaheen R., Thiemens M. H., Steele A., Fogel M. L., Bowden R., Glamoclija M., Zhang Z., and Elardo S. M. 2013. Unique meteorite from Early Amazonian Mars: Water-rich basaltic breccia Northwest Africa 7034. *Science* 339:780-785.

Anand M., James S., Greenwood R. C., Johnson D., Franchi I. A., and Grady, M. M. 2008. Mineralogy and geochemistry of shergottite RBT 04262 (abstract #2173) 39th Lunar and Planetary Science Conference. CD-ROM.

Anders E. and Grevesse N. 1989. Abundances of the elements: Meteoritic and solar. *Geochimica et Cosmochimica Acta* 53:197–214.

Barrat J. A., Gillet P. H., Sautter V., Jambon A., Javoy M., Göpel C., LeSourd M., Keller F., and Petit E. 2002.Petrology and chemistry of the basaltic shergottite North West Africa 480. *Meteoritics and Planetary Sciences* 37:487-499.

Basu Sarbadhikari A., Day J. M. D., Liu Y., Rumble III D., and Taylor L. A. 2009. Petrogenesis of olivine-phyric sherottite Larkman Nunatak 06319: Implications for enriched components in martian basalts. *Geochimica et Cosmochimica Acta* 73:2190–2214.

Beck A. and McSween H. Y. 2008. Fe and Mn systematic in olivine-bearing diogenite (abstract #1291) 39th Lunar and Planetary Science Conference. CD-ROM.

Bischoff A. and Stöffler D. 1992. Shock metamorphism as a fundamental process in the evolution of planetary bodies: information form meteorites. *European Journal of Mineralogy* 4:707-755.

Bogard D. D., Garrison D. H., Norman M., Scott E. R. D., and Keil K. 1995. ^{39}Ar-^{40}Ar and petrology of Chico: Large-scale impact melting on the L chondrite parent boy. *Geochimica et Cosmochimica Acta* 59:1383-1399.

Bridges J. C. and Warren P. H. 2006. The SNC meteorites: Basaltic igneous processes on Mars. *Journal of the Geological Society of London* 163:229–251.

Cartwright J. A., Ott U., Hermann S., and Agee C. B. 2013. NWA 7034 contains martian atmospheric noble gases (abstract #2314) 39th Lunar and Planetary Science Conference. CD-ROM.

Day J. M. D., Taylor L. A., Floss C., and McSween H. Y. 2006. Petrology and chemistry of MIL 03346 and its significance in understanding the petrogenesis of nakhlites on Mars. *Meteoritics and Planetary Science* 41:581–606.

Donaldson C. H. 1976. An experimental investigation of the delay in nucleation of olivine in mafic magmas. *Contribution to Mineralogy and Petrology* 69:21-32.

Donaldson C. H., Usselman T. M., Williams R. J., and Lofgren G. E. 1975. Experimental modeling of the cooling history of Apollo 12 olivines basalts. *Proc. Lunar Sci. Conf. 6th* pp. 843-869.

Dreibus G., Spettel B., Haubold R., Jochum K. P., Palme H., Wolf D., and Zipfel J. 2000. Chemistry of a new shergottite: Sayh Al Uhaymir 005. *Meteoritics and Planetary Science* 35, A49.

Faure F. and Schiano P. 2005. Experimental investigation of equilibration

conditions during forsterite growth and melt inclusion formation. *Earth and Planetary Science Letters* 236:882-898.

Faure F., Trolliard G., Nicollet C., and Montel J.-M. 2003. A developmental model of olivine morphology as a function of the cooling rate and the degree of undercooling. *Contribution to Mineralogy and Petrology* 145:251-263.

Faure F., Arndt N., and Libourel G. 2006. Formation of spinifex texture in komatiites: An experimental study. *Journal of Petrology* 47:1591-1610.

Filiberto, J., Treiman A. H., and Le L. 2008. Crystallization experiments on a Gusev Adirondack basalt composition. *Meteoritics and Planetary Science* 43:1137–1146.

Ganapathy R., Keays R. R., Laul J. C., and Anders. 1970. Trace elements in Apollo 11 lunr rocks: Implications for meteorite influx and origin of moon. *Proc. of the Apollo 11 Lunar Sci. Conf.* pp. 1117-1142.

Gellert R., Rider R., Bruckner J., Clark B. C., Dreibus G., Klingelhofer G., Lugmair G., Ming D. W., Wanke H., Yen A., Zipfel K., and Squyres S. W. 2006. Alpha Particle X-Ray Spectrometer (APXS): Results from Gusev crater and calibration report. *Journal of Geophysical Research* 111:E02S05.

Ghiorso M. S. and Sack R. O. 1995. Chemical mass-transfer in magmatic processes IV. A revised and internally consistent thermodynamic model for the interpolation and extrapolation of liquid-solid equilibria in magmatic systems at elevated-temperatures and pressures. *Contribution to Mineralogy and Petrology* 119*:*197-212.

Gillet P., Barrat J. A., Beck P., Marty B., Greenwood R. C., Franchi I. A., Bohn M., and Cotton J. 2005. Petrology, geochemistry, and cosmic-ray exposure age of lherzolitic shergottite Northwest Africa 1950. *Meteoritics and Planetary Science* 40:1175-1184.

Goderis S., Brandon A. D., Mayer B., Humayun M., and Agee C. B. 2014. Tracing impactor signals prevalent in martian regolith breccia Northwest Africa 7034 with Os isotopes and platinum group elements (abstract #2200) 45th Lunar and Planetary Science Conference. CD-ROM.

Gross J., Filiberto J., Herd C. D. K., Melwani M., Schwenzer S. P., and Treiman A. H. 2013. Petrography, mineral chemistry, and crystallization history of olivine-phyric shergottite NWA 6234: A new melt composition. *Meteoritics and Planetary Science* 48:854-871.

Herd C. D. K., Borg L. E., Jones J. H., and Papike J. J. 2002. Oxygen fugacity and geochemical variations in the martian basalts: Implications for martian basalt petrogenesis and the oxidation state of the upper mantle of Mars. *Geochimica et Cosmochimica Acta* 66:2025-2036.

Hewins R. H., Zanda B., Humayun M., Pont S., Fieni C. and Deldicque D. 2013a. Northwest Africa 7533, an impact breccia from Mars (abstract #2385) 45th Lunar and Planetery Science Conference. CD-ROM.

Hewins R. H., Zanda B., Humayun M., Lorand J.-P., Deldicque D., Pont S., Fieni C., Nemchin A., Grange M., Kennedy A., Gopel C., and Lewin E. 2013b. Petrology of NWA 7533: Formation by impact of ancient martian crust (abstract #5252) 76st Meteoritical Society Conference.

Hewins R. H., Zanda B., Humayun M., Lorand J.-P., and Pont S. 2014. Impact

melt rocks and pristine clasts in Northwest Africa 7533 (abstract #1416) 45th Lunar and Planetary Science Conference. CD-ROM.

Humayun M., Nemchin A., Zanda B., Hewins R. H., Grange M., Kennedy A., Lorand J.-P., Gopel C., Fieni C., Pont S., and Deldicque D. 2013a. Origin and age of the earliest martian crust from meteorite NWA 7533. *Nature* 503:513-516.

Humayun M., Zanda B., Hewins R. H., and Göpel C. 2013b. Composition of Northwest Africa 7533: Implications for the origin of martian soils and crust (abstract #1419) 44th Lunar and Planetary Science Conference. CD-ROM.

Ikeda Y., Kimura M., Takeda H., Shimoda G., Kita N. T., Morishita Y., Suzuki A., Jagoutz E., and Dreibus G. 2006. Petrology of a new basaltic shergottite: Dhofar 378. *Antarctica Meteorite Research* 19:20-44.

Jambon A., Barrat J. A., Sautter V., Gillet P. H., Göpel C., Javoy J. L., and LeSourd M. 2002. The basaltic shergottite Northwest Africa 856: Petrology and chemistry. *Meteoritics and Planetary Science* 37:1147-1164.

Jambon A., Barrat, J. A., Bollinger C., Sautter V., Boudouma O., Greenwood R. C., Franchi I., and Badia D. 2010. Northwest Africa 5790. Top sequence of the nakhlite pile (abstract #1696) 41st Lunar and Planetary Science Conference. CD-ROM.

Korotev R. L., Rumble D., and Irving A. J. 2013. Elemental and oxygen isotopic composition of martian mafic regolith breccia NWA 7475 (abstract #5046) 76st Meteoritical Society Conference.

Le Bas M. J., Le Maitre R. W., Streckeisen A., and Zanettin B. 1986. A chemical classification of volcanic rocks based on the total alkali-silica diagram. *Journal of Petrology* 27:745–750.

Lin Y., Qi L., Wang G., and Xu L. 2008. Bulk chemical composition of lherzolitic shergottite Grove Mountains 99027-Constraints on the mantle of Mars. *Meteoritics and Planetary Science* 43:1179–1187.

Lindstrom D. J. 1983. Kinetic effects on trace element partitioning. *Geochimica et Cosmochimica Acta* 47:617-622.

Lodders K. 1998. A survey of shergottite, nakhlite, and Chassigny meteorites whole-rock compositions. *Meteoritics and Planetary Science* 33:183-190.

Lofgren G., and Russell W. J. 1986. Dynamic crystallization of chondrule melts of porphyritic and radial pyroxene composition. *Geochimica et Cosmochimica Acta* 50:1715-1726.

Longhi J. and Pan V. 1989. The parent magma of the SNC meteorites. *Proc. Lunar Planet. Sci. Conf. 19th* pp. 451-464.

McCubbin F. M., Elardo S. M., Shearer C. K., Smirnov A., Hauri E. H., and Draper D. S. 2013. A petrogenetic model for the comagmatic origin of chassignites and nakhlites: interences from chlorine-rich minerals, petrology, and geochemistry. *Meteoritics and Planetary Science* 48:819-853.

McCoy T. J., Wadhwa M., and Keil K. 1999. New lithologies in the Zagami meteorite: Evidence for fractional crystallization of a single magma unit on Mars. *Geochimica et Cosmochimica Acta* 63:1249–1262.

McGlynn I. O., Fedo C. M., and McSween H. Y. 2011. Origin of basaltic soils at Gusev Crater, Mars, by Aeolian modification and impact-generated sediment. *Journal of*

Geophysical Research 116:E00F22.

McSween H. Y., Eisenhour D. D., Taylor L. A., Wadhwa M., and Crozaz G. 1996. QUE 94201 shergottite: Crystallization of a Martian basaltic magma. *Geochimica et Cosmochimica Acta* 60:4563–4569.

McSween H. Y., Wyatt M. B., Gellert R., Bell III J. F., Morris R. V., Herkenhoff K. E., Crumpler L. S., Milam K. A., Stockstill K. R., Tornabene L. L., Arvidson R. E., Bartlett P., Blaney D., Cabrol N. A., Christensen P. R., Clark B. C., Crisp J. A., Des Marais D. J., Economou T., Farmer J. D., Farrand W., Ghosh A., Golombek M. , Gorevan S., Greeley R., Hamilton V. E., Johnson J. R., Joliff B. L., Klingelhöfer G., Knudson A. T., McLennan S., Ming D., Moersch J. E., Rieder R., Ruff S. W., Schröder C., de Souza, Jr., P. A., Squyres S. W., Wänke H., Wang A., Yen A., and Zipfel J. 2006. Characterization and petrologic interpretation of olivine-rich basalts at Gusev Crater, Mars. *Journal of Geophysical Research* 111:E02S10.

McSween H. Y., H. Y.,Ruff S. W., Morris R. V., Gellert R., Klingelhofer G., Christensen P. R., McCoy T. J., Ghosh A., Moersch J. M., Cohen B. A., Rogers A. D., Schroder C., Squyres S. W., Crisp J., and Yen A. 2008. Mineralogy of volcanic rocks in Gusev Crater, Mars: Reconciling Mossbauer, Alpha Particle X-Ray Spectrometer, and Miniature Thermal Emission Spectrometer spectra. *Journal of Geophysical Research* 113:E06S04.

McSween H. Y., Taylor G. J., and Wyatt M. B. 2009. Elemental composition of the martian crust. *Science* 324:736-739.

Mikouchi T., Monkawa A., Koizumi E., Chokai J., and Miyamoto M. 2005. MIL03346 Nakhlite and NWA 2737 ("Diderot") chassignite: Two new martian cumulate rocks from hot and cold deserts (abstract #1944) 36th Lunar and Planetary Science Conference. CD-ROM.

Monders A. G., Médard E., and Grove T. L. 2007. Phase equilibrium investigations of the Adirondack class basalts from the Gusev plains, Gusev Crater, Mars. *Meteoritics and Planetary Science* 42:131-148.

Morris R.V., Klingelhofer G., Bernhardt B., Schroder C., Rodionov D. S., de Souza, Jr., P. A., Yen A., Gellert R., Evlanov E. N., Foh J., Kankeleit E., Gutlich P., Ming D. W., Renz F., Wdowiak T., Squyres S. W., and Arvidson R. E. 2004. Mineralogy at Gusev crater from the Mossbauer spectrometer on the Spirit rover. *Science* 305:833-836.

Mutchler S. R., Fedele L., and Bodnar R. J. 2008. Analysis Management System (AMS) for reduction of laser ablation ICPMS data. In *Laser-Ablation-ICPMS in the Earth Sciences: Current Practices and Outstanding Issues* (ed. P. Sylvester). Mineralogical Association of Canada, Quebec.

Norman M. D., Bennett V. C., and Ryder G. 2002. Targeting the impactors: siderophile element signatures of lunar impact melts from Serenitatis. *Earth and Planetary Science Lett*ers 202:217-228.

Norman M. D., Duncan R. A., and Huard J. J. 2006: Identifying impact events within the lunar cataclysm from ^{40}Ar-^{39}Ar ages and compositions of Apollo 16 impact. *Geochimica et Cosmochimica Acta* 70:6032-6049.

Papike J. J., Hodges F. N., Bence A. E., Cameron M, and Rhodes J. M. 1976. Mare Basalts' crystal chemistry, mineralogy, and petrology. *Reviews of Geophysics and Space Physics* 14:475-540.

Papike J. J., Ryder G., and Shearer C. K. 1998. Lunar samples. In *Planet. Mat. Mineral. Soc. Am. Washington, DC. Rev. Mineral.* (ed. J. J. Papike). Vol 36. pp. 5-1-5-234.

Papike J. J., Karner J. M., Shearer C. K., Burger P. V. 2009. Silicate mineralogy of martian meteorites. *Geochimica et Cosmochimica Acta* 73:7443–7485.

Rondot J. 1971. Impactite of the Charlevoix structure. Quebec, Canada. *J. Geophys. Res.* 76, 5414-4523.

Rubin A. E., Warren P. H., Greenwood J. P., Verish R. S., Leshin L. A., Hervig R. L., Clayton R. N., and Mayeda T. K. 2000. Los Angeles: The most differentiated basaltic martian meteorite. *Geology* 28:1011-1014.

Rubin A. E. 1985. Impact melt products of chondrite material. *Reviews of Geophysics* 23:277-300.

Ruzicka A., Snyder G. A., and Taylor L. A. 2000. Crystal-bearing lunar spherules: Impact melting of the Moon's crust and implications for the origin of meteoritic chondrules. *Meteoritics and Planetary Sciences* 35:173-192.

Santos A. R., Agee C. B., Shearer C. K., Burger P. V., and McCubbin F. M. 2014. A trace element investigation into the petrogenetic relationships of different igneous lithologies within martian meteorite NWA 7034 (abstract #2621) 45th Lunar and Planetary Science Conference. CD-ROM.

Shirai N. and Ebihara M. 2004. Chemical characteristics of a martian meteorite, Yamato 980459. *Antarctica Meteorite Research* 17:55-67.

Smith P. M., and Asimow P. D. 2005. Adiabat_1ph: A new front end to the MELTS, pMELTS, and pHMELTS models. *Geochemistry, Geophysics, and Geosystems* 6:Q02004.

Symes S. J. K., Sears D. W. G., Akridge D. G., Huang S., and Benoit P. H. 1998. The crystalline lunar spherules: Their formation and implications for the origin of meteoritic chondrules. *Meteoritics and Planetary Sciences* 48:13-29.

Udry A., McSween H. Y., Lecumberri-Sanchez P., and Bodnar R. J. 2012. Paired nakhlites MIL 090030, 090032, 090136, and 03346: Insights into the Miller Range parent meteorite. *Meteoritics and Planetary Sciences* 47:1575-1589.

Usui T., McSween H. Y., and Floss C. 2008. Petrogenesis of olivine-phyric shergottite Yamato 980459, revisited. *Geochimica et Cosmochimica Acta* 72:1711–1730.

Treiman A. H. and Irving A. J. 2008. Petrology of Martian meteorite Northwest Africa 998. *Meteoritics and Planetary Sciences* 43:829-854.

Watson E. B. 1996. Surface enrichment and trace-element uptake during crystal growth. *Geochimica et Cosmochimica Acta* 60, 5013-5020.

Warner R. D., Taylor G. J., Jeil K., Planner H. N., Nehru C. E., Ma, and Schmitt R. A. 1979. Green glass vitrophyre 78526: An impact melt of very low-Ti mare basalt composition. *Proc. Lunar Planet. Sci. Conf. 9th*, pp. 547-563.

Wright T. L. and Doherty P. C. 1970. A linear programming and least squares computer method for solving petrologic mixing problems. *Geological Society of America Bulletin* 81:1995-2008.

Yin Q.-Z., McCubbin F. M., Zhou Q., Santos A. R., Tartese R., Li X., Li Q., Liu Y., Tang G., Boyce J. W., Lin Y., Yang W., Zhang J., Hao J., Elardo S. M., Shearer C. K., Rowland D. J., Lerche M., and Agee C. B. 2014. An Earth-like beginning for ancient Mars indicated by alkali-rich volcanism at 4.4 Ga (abstract #1320) 45th Lunar and Planetary Science Conference. CD-ROM.

Zipfel J., Zipfel J., Schroder C., Joliff B. L., Gellert R., Herkenhoff K. E., rieder R., Anderson R., Bell J. F., Bruckner J., Crisp J. A., Christensen P. R., Clark B. C., de Souza Jr. P. A., Dreibus G., d'Uston C., Economou T., Gorevan S. P., Hahn B. C., Klingelhofen G., McCoy T. J., McSween H. Y., Ming D. W., Morris R. V., Rodionov D. S., Squyres S. W., Wanke H., Wright S. P., Wyatt M. B., and Yen A. S. 2011. Bounce Rock-A shergottite-like basalt encountered at Meridiani Planum, Mars. *Meteoritics and Planetary Sciences* 46:1-20.

Appendix D

Table D1. Average major element composition of minerals in the vitrophyre (1σ standard deviation).

wt%	Pyroxene core (n=35)	Pyroxene rim (n=13)		Olivine (n=39)	Fe-oxides (n=5)
SiO_2	51.9 (7)	50.5 (14)		35.7 (5)	0.68 (60)
TiO_2	0.30 (21)	0.38 (15)		0.04 (1)	1.46 (72)
Al_2O_3	2.66 (59)	3.29 (115)		0.07 (4)	0.97 (42)
Cr_2O_3	0.94 (15)	0.46 (27)		0.02 (1)	0.15 (12)
FeOT	17.6 (11)	21.1 (16)		34.1 (24)	87.0 (21)
MnO	0.38 (4)	0.48 (6)		0.78 (10)	0.12 (7)
MgO	24.3 (13)	20.7 (22)		28.9 (20)	0.43 (29)
CaO	1.5 (3)	2.52 (86)		0.11(3)	0.39 (24)
Na_2O	0.04 (6)	0.04 (3)		b.d.	-
K_2O	0.01 (0)	0.01 (0)		b.d.	-
P_2O_5	-	-		0.20 (1)	-
NiO	0.30 (3)	-		0.41 (4)	0.24 (12)
Total	99.6 (3)	99.4 (2)		100.3 (4)	91.5 (11)
En	65	69	Fo	60	
Fs	30	28	Fa	40	
Wo	5	3			

b.d. = below detection

Table D2. Average and representative major element composition of mesostasis and mesostasis variants in the vitrophyre (1σ standard deviation).

wt%	Mesostasis (n=92)	Variant 1 (n=5)	Variant 2 (n=3)	Variant 3 (n=1)	Variant 4 (n=1)
SiO_2	47.6 (20)	63.9 (5)	70.2 (20)	53.6	86.4
TiO_2	1.44 (15)	0.01 (2)	0.04 (1)	0.03	0.04
Al_2O_3	11.9 (14)	21.7 (8)	17.7 (9)	14.7	8.42
Cr_2O_3	0.06 (6)	0.01 (1)	0.01 (1)	0.01	0.03
FeO	19.4 (27)	0.73 (23)	1.22 (34)	10.3	1.07
MnO	0.32 (5)	0.02 (1)	0.02 (1)	0.26	0.02
MgO	5.85 (128)	0.05 (4)	0.15 (20)	6.57	0.03
CaO	9.30 (155)	5.02 (91)	6.96 (58)	9.20	3.38
Na_2O	3.07 (67)	7.21 (70)	3.18 (47)	3.74	1.20
K_2O	0.44 (24)	0.92 (68)	0.30 (5)	0.29	0.37
P_2O_5	0.44 (8)	0.63 (78)	0.10 (10)	0.15	b.d.
NiO	0.06 (3)	0.02 (3)	b.d.	0.09	b.d.
Total	99.9 (5)	99.9 (5)	99.9 (5)	98.9	101.0

b.d. = below detection

Table D3. Average major and trace element composition of mesostasis in the vitrophyre (1σ standard deviation), calculated major element and measured trace element composition of the bulk NWA 7034 vitrophyre.

wt%	Mesostasis (n = 92)	Bulk NWA 7034 melt clast	Humphrey[a, b]
SiO_2	47.6 (20)	47.5	45.9
TiO_2	1.44 (15)	1.14	0.55
Al_2O_3	11.9 (14)	9.40	10.7
Cr_2O_3	0.06 (6)	0.22	0.60
FeO	19.4 (27)	20.1	18.8
MnO	0.32 (5)	0.36	0.41
MgO	5.85 (128)	10.8	10.4
CaO	9.30 (155)	7.25	7.84
Na_2O	3.07 (67)	2.31	2.54
K_2O	0.44 (24)	0.33	0.10
P_2O_5	0.44 (8)	0.34	0.56
Total	99.3 (5)	99.8	98.4
ppm	(n = 29)		
Sc	69.9 (25)	67.3	-
V	43.9 (34)	44.0	-
Co	86.0 (122)	111	-
Ni	496 (93)	1021	164
Zn	16.2 (188)	14.0	112
Ga	5.80 (86)	4.63	-
Rb	48.7 (427)	21.8	-
Sr	65.2 (425)	33.8	-
Y	26.5 (34)	17.1	-
Zr	140 (18)	95.0	-
Nb	14.2 (18)	9.51	-
Cs	8.76 (152)	2.36	-
Ba	71.3 (253)	67.9	-
La	9.93 (124)	6.29	-
Ce	24.4 (27)	17.1	-
Pr	3.40 (42)	2.23	-
Nd	16.3 (21)	10.6	-
Sm	4.51 (59)	2.89	-
Eu	1.27 (23)	0.79	-
Gd	5.02 (69)	3.25	-
Tb	0.79 (11)	0.52	-
Dy	5.0 (65)	3.30	-
Ho	0.99 (130)	0.64	-
Er	2.84 (34)	2.32	-
Tm	0.37 (5)	0.25	-
Yb	2.54 (30)	1.70	-
Lu	0.34 (5)	0.24	-
Hf	3.19 (39)	2.26	-
Th	1.46 (20)	0.97	-

[a] McSween et al. (2008); [b] Gellert et al. (2006)

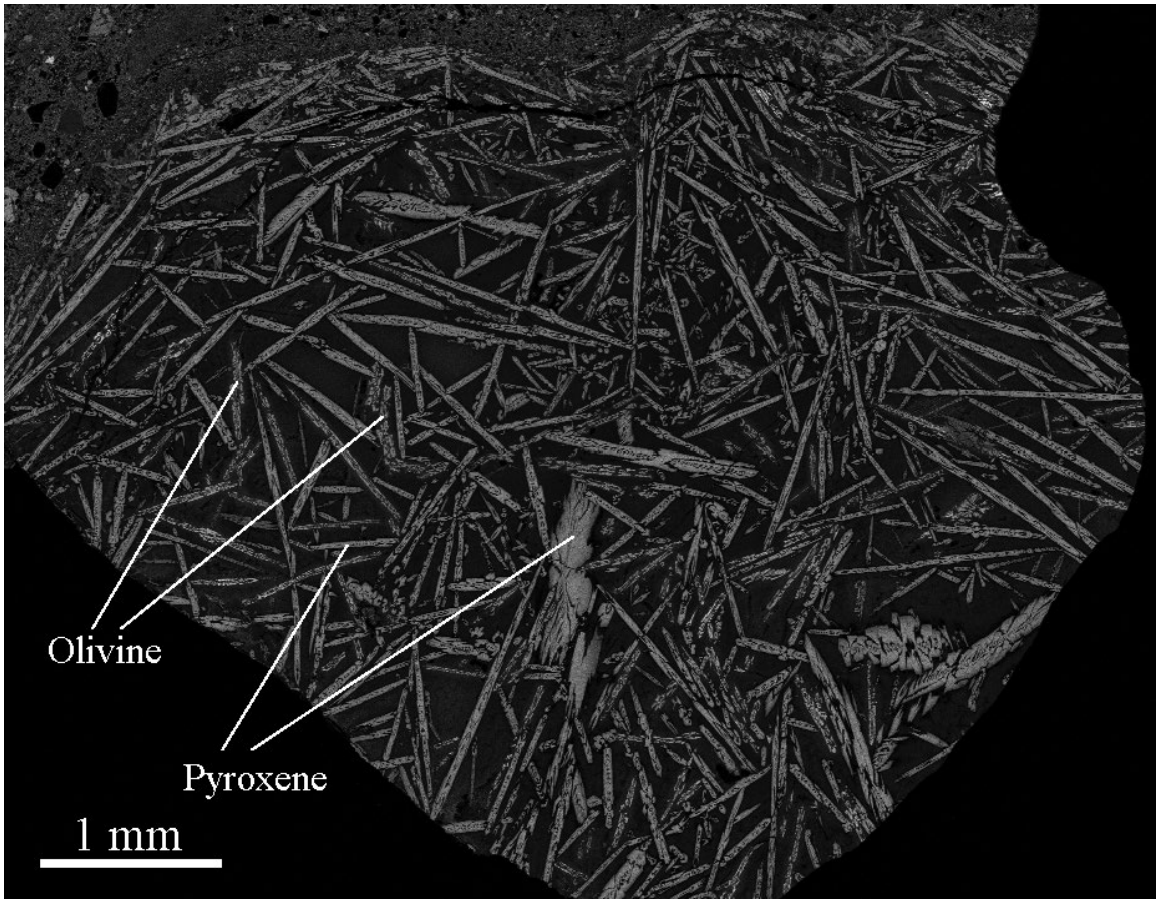

Figure D1. Mg elemental map of the vitrophyre. Olivine and pyroxene are brighter than the mesostasis.

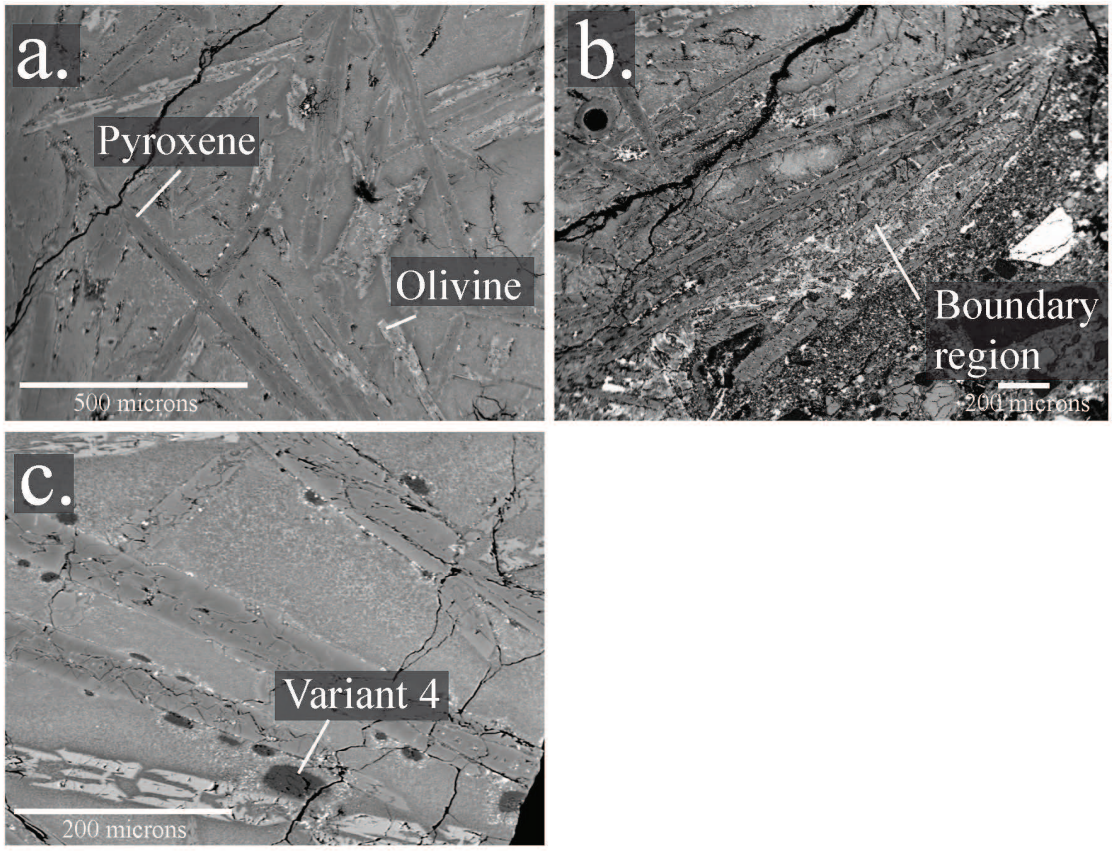

Figure D2. Backscattered electron images of the vitrophyre clast: a) vitrophyric skeletal crystals of pyroxene and olivine, the olivine appears lighter and more skeletal than the pyroxene, b) vitrophyre boundary region with oriented pyroxene grains, and c) mesostasis variant 4.

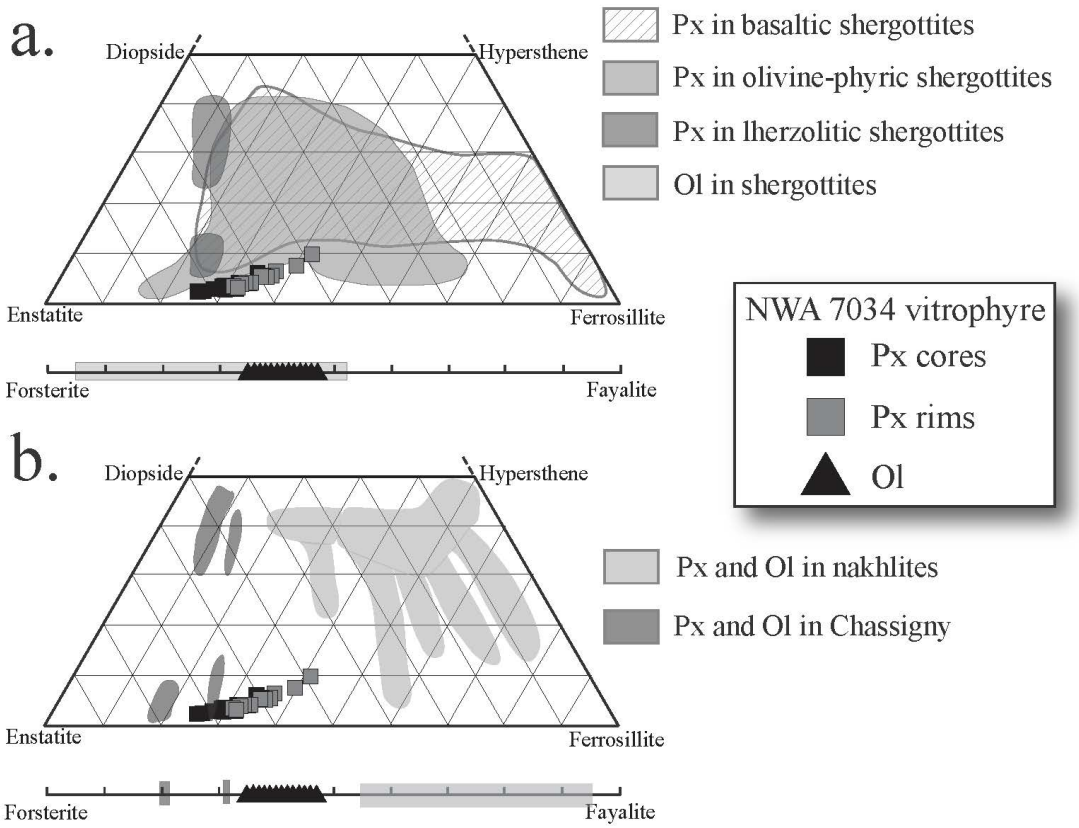

Figure D3. NWA 7034 vitrophyre pyroxene cores (black squares), pyroxene rims (grey squares), and olivine (black triangles) compositions. Envelopes of a) basaltic, olivine-phyric, and lherzolitic shergottites from McSween et al. (1996), McCoy et al. (1999), Taylor et al. (2002), Bridges and Warren (2006), Usui et al. (2008), Basu Sarbadhikari et al. (2009), and Gross et al. (2013), b) nakhlites from Jambon et al. (2010) and Udry et al. (2012) and chassignites from Wadhwa and Crozaz (1995) and Mikouchi et al. (2005).

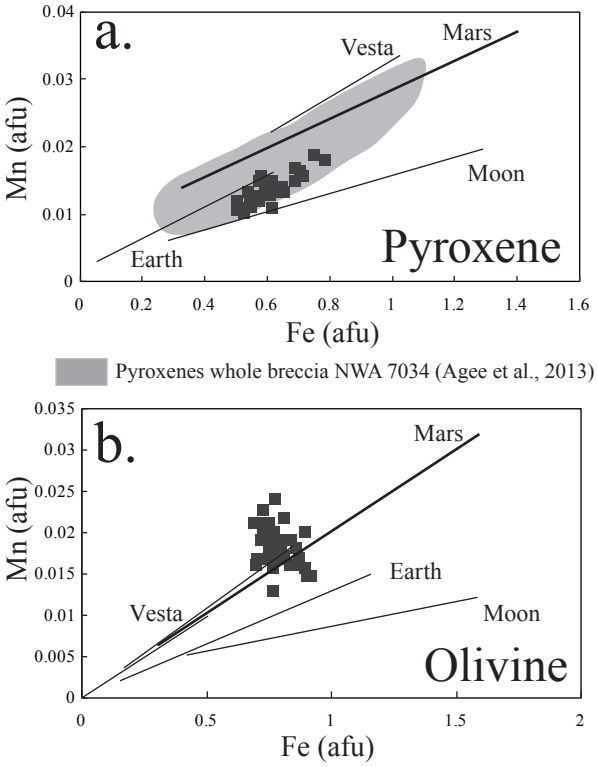

Figure D4. Mn vs. Fe (afu) diagram for a) pyroxene and b) olivine from the vitrophyre NWA 7034 (squares). Mn-Fe lines for different planets from Papike et al. (2009) and Vesta olivine compositions from Beck and McSween (2008). Host breccia pyroxene compositions are from Agee et al. (2013).

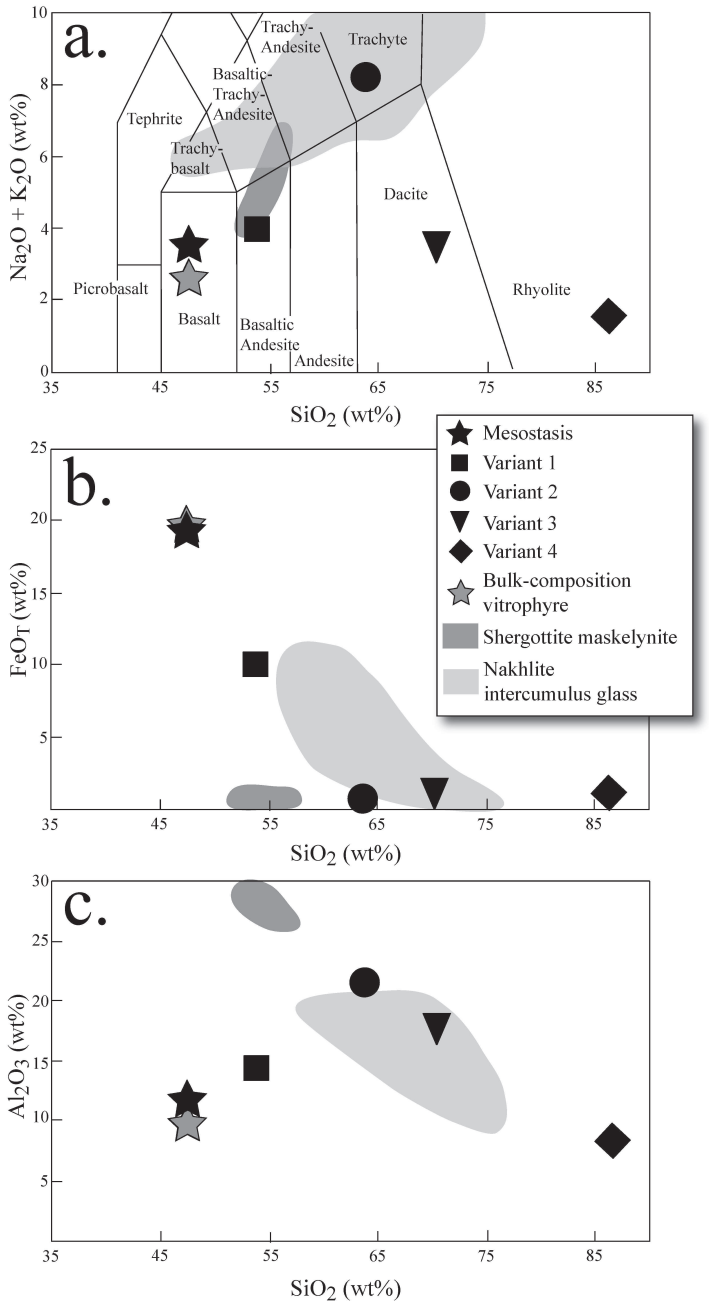

Figure D5. a) Total alkalis versus silica (wt%) diagram for the classification of volcanic rocks (Le Bas et al., 1986) representing the mesostasis and four variant compositions from this study and bulk NWA 7034 breccia from Agee et al. (2013) (i.e., Table 2), b) SiO_2 vs FeO_T (wt%) diagram, and c) SiO_2 vs Al_2O_3 (wt%). Shergottite maskelynite composition is from Papike et al. (2009) and nakhlite intercumulus glass compositions from Day et al. (2006).

Figure D6. Bulk composition diagrams for NWA 7034 bulk vitrophyre, basaltic, olivine-phyric, and lherzolitic shergottites, nakhlites, Chassigny, ALH 84001, Bounce Rock, and Gusev basalts (Adirondack, Humphrey, Mazatzal) and soils from Lodders (1998), Rubin et al. (2000), Dreibus et al. (2000), Barrat et al. (2002), Jambon et al. (2002), Shirai and Ebihara (2004), Gillet et al. (2005), Ikeda et al. (2006), Day et al. (2006), Anand et al. (2008), Treiman and Irving (2008), Lin et al. (2008), McSween et al. (2008), McSween et al. (2009), Basu Sarbadhikari et al. (2009), and Zipfel et al. (2011). These various compositions are plotted on: a) Mn-Fe (wt%) diagram with martian meteorite lines (McSween et al., 2009), b) Total alkalis versus silica (wt%) diagram, c) Ca/Si-Mg/Si (atomic ratio) diagram used for classification of martian meteorites, d) Mg/Si-Al/Si (atomic ratio) diagram, and e) Ni (ppm)-Mg (wt%) diagram with terrestrial and martian fractionation lines (McSween et al., 2009).

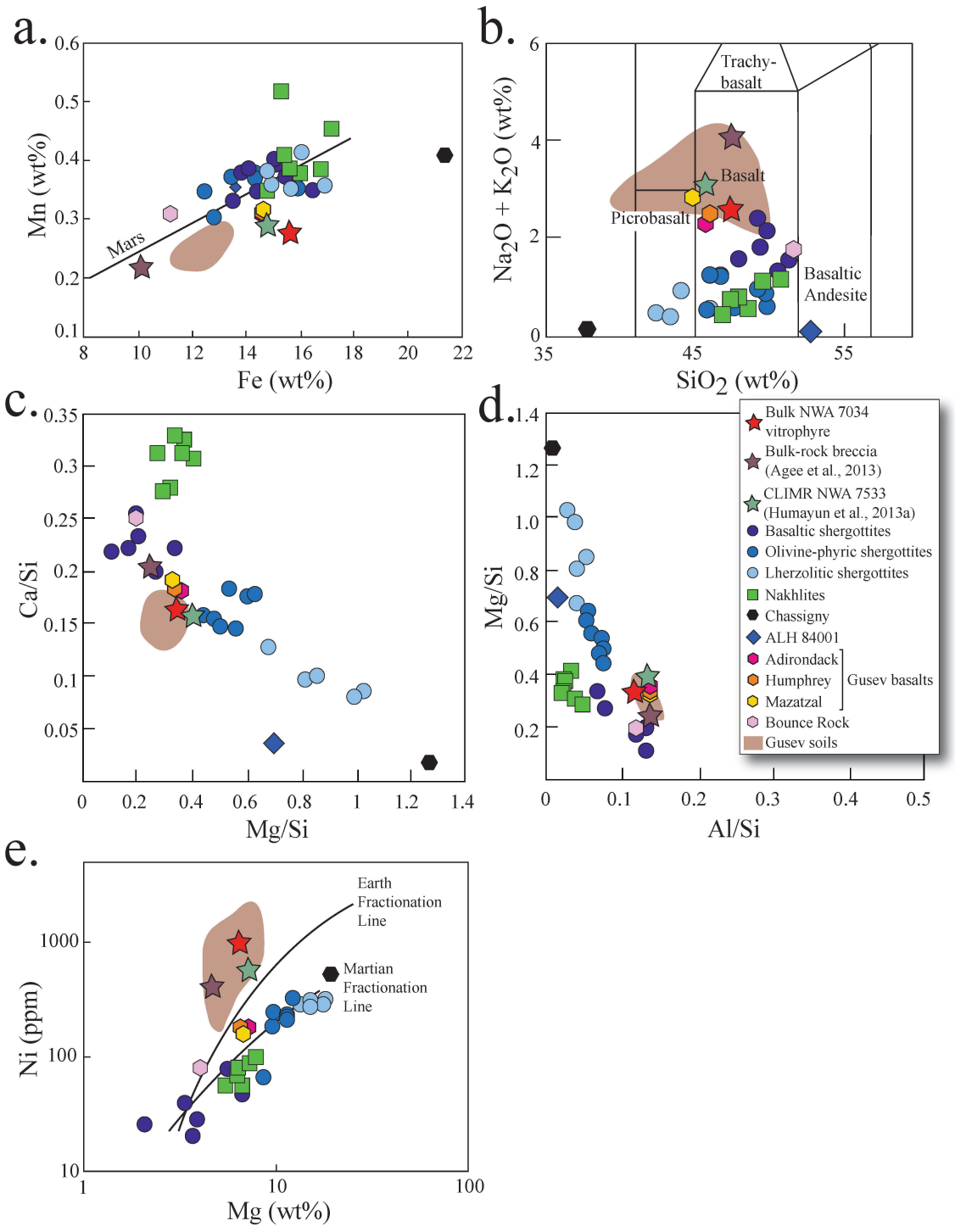
a.
Mn (wt%)
Fe (wt%)
Mars
b.
Na2O + K2O (wt%)
SiO2 (wt%)
Trachy-basalt
Basalt
Picrobasalt
Basaltic Andesite
c.
Ca/Si
Mg/Si
d.
Mg/Si
Al/Si
Bulk NWA 7034 vitrophyre
Bulk-rock breccia (Agee et al., 2013)
CLIMR NWA 7533 (Humayun et al., 2013a)
Basaltic shergottites
Olivine-phyric shergottites
Lherzolitic shergottites
Nakhlites
Chassigny
ALH 84001
Adirondack
Humphrey
Mazatzal
Gusev basalts
Bounce Rock
Gusev soils
e.
Ni (ppm)
Mg (wt%)
Earth Fractionation Line
Martian Fractionation Line

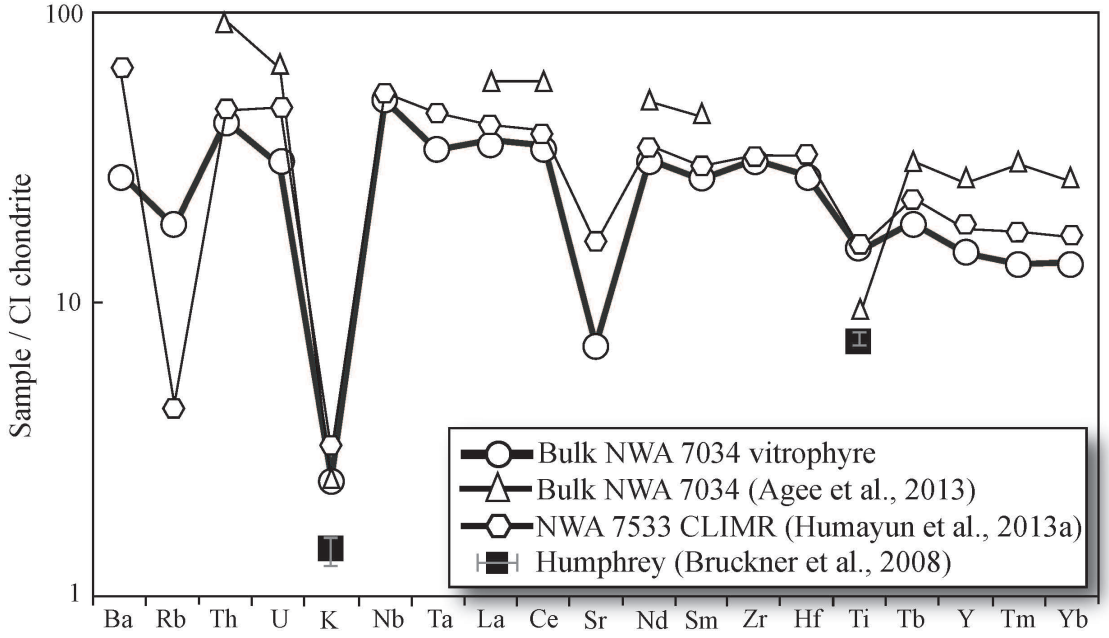

Figure D7. Minor and trace element concentrations normalized to CI-chondrite (Anders and Grevesse, 1989) of NWA 7034 bulk vitrophyre (circles), NWA 7034 bulk host breccia (triangles: Agee et al., 2013), NWA 7533 clast-laden impact melt rocks (hexagons: Humayun et al., 2013b), and Humphrey (squares and errors: Gellert et al., 2006).

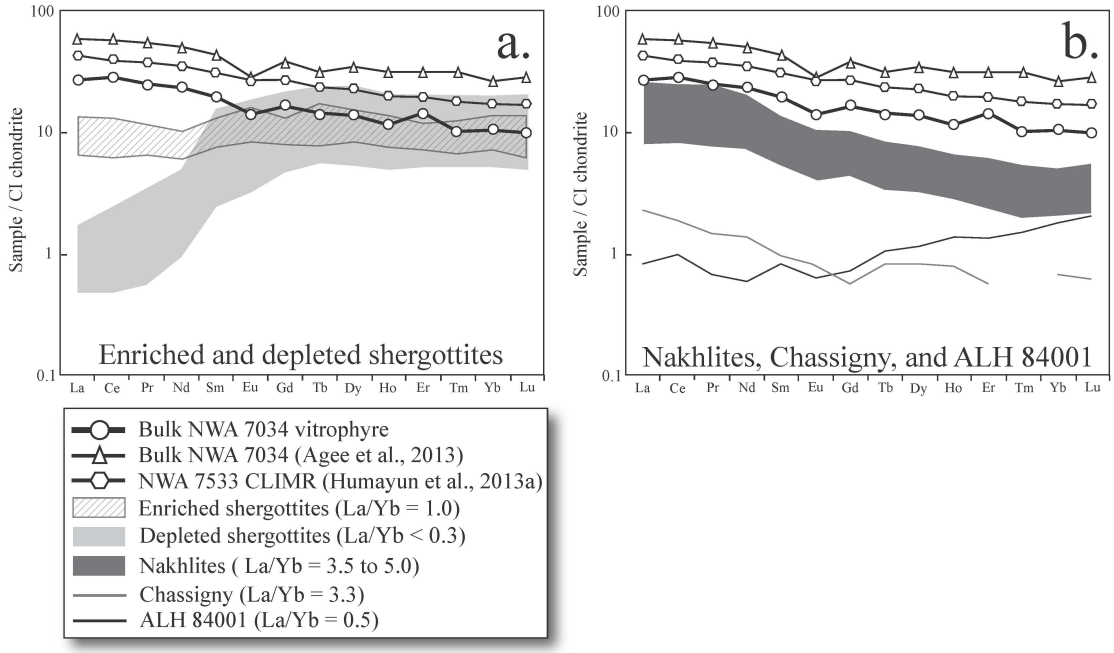

Figure D8. REE concentrations normalized to CI-chondrite (Anders and Grevesse, 1989) of NWA 7034 bulk vitrophyre (circles), NWA 7034 bulk host breccia (triangles: Agee et al. 2013), and NWA 7533 clast-laden impact melt rocks (hexagons: Humayun et al., 2013), with bulk compositions of a) enriched and depleted shergottites and b) nakhlites, Chassigny, and ALH 84001 (see references in Fig. 6 caption). La/Yb are mentioned for each meteorite type indicating their enrichment. Bulk vitrophyre REE composition is different from the NWA 7034 host breccia, NWA 7533 clast-laden impact melt rocks, and other martian meteorite REE compositions.

CONCLUSION

In chapter I of this dissertation, we explore fractional crystallization of various martian primary and parental magmas under different conditions as well as the formation of alkaline rocks on Mars using thermodynamical computer modeling. These calculations show that fractional crystallization of primary magmas on Mars can produce very diverse compositions. This study also illustrates the fact that isobaric and polybaric fractional crystallization produce residual liquids with similar compositions. Consequently, future isobaric experiments at different pressures (polybaric experiments are not feasible) can approximate fractionation under polybaric conditions. In addition, we show that alkaline magmas can be easily formed from known primary martian magmas if fractionation occurs at high pressure. This suggests that alkaline magmas might be widespread on Mars and due to the progressive thickening of the crust, the volume of formed alkaline magmas may have increased with time on Mars. Consequently, martian basalt compositions on Mars might be more diverse than represented by the martian meteorite collection and basalts analyzed by the rovers on the martian surface.

In chapter II, we investigate water degassing in various shergottite parental magmas using analyses of light lithophile elements (LLE: Li, B, and Be) and Li isotopes in pyroxene, olivine, and maskelynite analyzed by SIMS. LLEs and Li isotopes have different solubilities in exsolved aqueous fluids so will be fractionated during degassing. Light lithophile element profiles in pyroxene and olivine in all the studied shergottites indicate water degassing from their parental magmas. Li isotope pyroxene profiles in QUE 94201 and Tissint also suggest water degassing of their parental mantle magmas. These two depleted shergottites represent the youngest and oldest samples from the depleted shergottites showing that the entire depleted shergottite magmatic complex might have undergone water degassing. However, Li isotope pyroxene profiles in Shergotty and LAR 06319 indicate lithium sub-solidus degassing. We conclude that enriched shergottites might have undergone degassing but followed by lithium diffusion, which is a common process in basalts. This study shows that degassed water from shergottite magmas might have been a major source for surficial water during the Amazonian period.

In chapter III, we study the pairing of the Miller Range nakhlites, MIL 090030, 090032, 090136, and 03346. Using mineralogy, texture, crystal size distribution analyses, *in situ* major, minor, and trace element compositions, we showed that the four Miller Range nakhlites are paired. However, they all show different modal abundances indicating that each individual nakhlite sample is not modally representative of its parent meteorite. These results suggest that modal abundances have to be carefully used for placement of nakhlites within the cumulate pile. Discovery of additional nakhlite samples will be critical to better understand the petrology and stratigraphy of the nakhlite cumulate pile and will allow constraining the formation of common martian meteorites.

In chapter IV, we investigate an unusual vitrophyric melt clast in the martian breccia NWA 7034. This vitrophyre displays a texture that was not previously observed in martian meteorites. It was formed from impact melting and crystallized very quickly as indicated by its texture and disequilibrium crystallization compositions. This is shown by

the olivine and pyroxene $K_D^{Fe/Mg}$, as well as a reversed order of crystallization and mineral compositions relative to those predicted by thermodynamical modeling. The parent rock of this vitrophyre had a different composition than martian soils and meteorites, but exhibits an almost identical major element composition as the Humphrey Gusev basalt. This study demonstrates that the further study of the various lithologies of the NWA 7034 breccia and paired samples as well as future breccia samples could potentially reveal new martian compositions never studied before, which would yield essential information about the composition and processes of the martian interior.

This dissertation, which includes petrological studies of a wide variety of martian basalts, shows that these rocks can lead to a better understanding of martian igneous compositions as well as martian mantle and crustal petrological processes. This study demonstrates that there is a tremendous diversity in martian basaltic compositions. Further study of new martian meteorites and surface rocks will be critical to fully constrain petrological martian processes, martian volatile inventory, and the diversity of martian igneous compositions.

VITA

Arya Udry was born February 3rd, 1988 in Geneva, Switzerland. She spent her childhood in Brittany, Western France, and Geneva, where she attended Ferney-Voltaire international middle school and high school. The catalyst for her passion in geology came from studying geology in high school and growing up in the Alps and the Jura.

After graduating from high school, Arya attended the University of Lausanne in Switzerland where she pursued a Bachelor's of Science degree in Geology and Environmental Sciences and a Master's of Science degree specialized in petrology and geochemistry. During her undergraduate studies, she spent nearly nine months in various field camps throughout Europe, which cultivated her love for field-work and petrology. After starting her Master's degree in 2008, focusing on granulitic Archean rocks in NW Scotland, she spent two months in the field and learned about various petrological techniques.

Arya entered the Earth and Planetary Science program at the University of Tennessee, Knoxville, in the fall of 2010 to pursue a childhood dream to work on martian geology. During these four years, she worked under the direction of Professor Hap McSween, and had the opportunity to work on various martian meteorites. She has taught geology, mineralogy, and petrology at various levels from freshmen to graduate students and attended many international planetary and terrestrial meetings. Upon completion of her dissertation defense, Arya will begin a tenure-track petrology position at the University of Nevada, Las Vegas in September 2014.